Title
Density Functional Perturbation Theory and Adaptively Compressed Polarizability Operator

Author
Xu, Ze

Publication Date
2019

Peer reviewed|Thesis/dissertation

Density Functional Perturbation Theory and Adaptively Compressed Polarizability Operator

by

Ze Xu

A dissertation submitted in partial satisfaction of the

requirements for the degree of

Doctor of Philosophy

in

Applied Mathematics

in the

Graduate Division

of the

University of California, Berkeley

Committee in charge:

Associate Professor Lin Lin, Chair
Professor John Strain
Professor Daniel Tataru
Associate Professor Adityanand Guntuboyina

Fall 2019

Density Functional Perturbation Theory and Adaptively Compressed Polarizability Operator

Abstract

Density Functional Perturbation Theory and Adaptively Compressed Polarizability Operator

by

Ze Xu

Doctor of Philosophy in Applied Mathematics

University of California, Berkeley

Associate Professor Lin Lin, Chair

Kohn-Sham density functional theory (KSDFT) is by far the most widely used electronic structure theory in condensed matter systems. Density functional perturbation theory (DFPT) studies the response of a quantum system under small perturbation, where the quantum system is described at the level of first principle electronic structure theories like KSDFT. One important application of DFPT is the calculation of vibration properties such as phonons, which can be further used to calculate many physical properties such as infrared spectroscopy, elastic neutron scattering, specific heat, heat conduction, and electron-phonon interaction related behaviors such as superconductivity . DFPT describes vibration properties through a polarizability operator, which characterizes the linear response of the electron density with respect to the perturbation of the external potential. More specifically, in vibration calculations, the polarizability operator needs to be applied to $d \times N_A \sim \mathcal{O}(N_e)$ perturbation vectors, where d is the spatial dimension (usually $d = 3$), N_A is the number of atoms, and N_e is the number of electrons. In general the complexity for solving KSDFT is $\mathcal{O}(N_e^3)$, while the complexity for solving DFPT is $\mathcal{O}(N_e^4)$. It is possible to reduce the computational complexity of DFPT calculations by "linear scaling methods". Such methods can be successful in reducing the computational cost for systems of large sizes with substantial band gaps, but this can be challenging for medium-sized systems with relatively small band gaps.

In the discussion below, we will slightly abuse the term "phonon calculation" to refer to calculation of vibration properties of condensed matter systems as well as isolated molecules. In order to apply the polarizability operator to $\mathcal{O}(N_e)$ vectors, we need to solve $\mathcal{O}(N_e^2)$ coupled Sternheimer equations. On the other hand, when a constant number of degrees of freedom per electron is used, the size of the Hamiltonian matrix is only $\mathcal{O}(N_e)$. Hence asymptotically there is room to obtain a set of only $\mathcal{O}(N_e)$ "compressed perturbation vectors", which encodes essentially all the information of the $\mathcal{O}(N_e^2)$ Sternheimer equations. In this dissertation, we develop a new method called adaptively compressed polarizability operator (ACP) formulation, which successfully reduces the computational complexity of phonon

calculations to $\mathcal{O}(N_e^3)$ for the first time. The ACP formulation does not rely on exponential decay properties of the density matrix as in linear scaling methods, and its accuracy depends weakly on the size of the band gap. Hence the method can be used for phonon calculations of both insulators and semiconductors with small gaps.

There are three key ingredients of the ACP formulation. 1) The Sternheimer equations are equations for shifted Hamiltonians, where each shift corresponds to an energy level of an occupied band. Hence for a general right hand side vector, there are N_e possible energies (shifts). We use a Chebyshev interpolation procedure to disentangle such energy dependence so that there are only constant number of shifts that is independent of N_e. 2) We disentangle the $\mathcal{O}(N_e^2)$ right hand side vectors using the recently developed interpolative separable density fitting procedure, to compress the right-hand-side vectors. 3) We construct the polarizability by adaptive compression so that the operator remains low rank as well as accurate when applying to a certain set of vectors. This make it possible for fast computation of the matrix inversion using methods like Sherman-Morrison-Woodbury.

In particular, the new method does not employ the "nearsightedness" property of electrons for insulating systems with substantial band gaps as in linear scaling methods. Hence our method can be applied to insulators as well as semiconductors with small band gaps.

This dissertation also extend the method to deal with nonlocal pseudopotentials as well as systems in finite temperature. Combining all these components together, we obtain an accurate, efficient method to compute the vibrational properties for insulating and metallic systems.

To my mom.

Contents

List of Figures

List of Tables

Acknowledgments

I would like to thank my thesis adviser Professor Lin Lin. He have led me to the research topic, taught me the fundamental theories from scratch, inspire me when there is little progress on the research, and also taught me how to ask questions, how to solve problems, and how to think as a computational scientist. He have acted as a teacher as well as a close friend of mine. Without his guidance, inspiration, and encouragement, I cannot imagine how I would overcome the problems and difficulties in my research.

I would like to thank all my colleagues at University of California, Berkeley and Lawrence Berkeley National Laboratory: Wei Hu, Weile Jia, Michael Lindsey, Leonardo Zepeda-Nùñez, Jiefu (Jeff) Zhang, Jeffmin Lin, Yu Tong. Special thanks are given to Dong An for the numerous support and discussion. Without their help, my achievements would not be possible.

I would like to thank the encouragement and support I received from other professors at University of California, Berkeley, especially from Professor Jon Wilkoning, Professor James Sethian and Professor John Strain. I would also like to thank Professor Jianfeng Lu and Professor Lexing Ying for their numerous support and guidance in my research.

Many thanks are given to all my close friends. I enjoyed every single day with every one of you at Berkeley for the past years.

Last but not least, I would thank my girlfriend Wei Wang for her patience and support, and for the love that she gives to me every day in my life. My beloved mom holds all my gratitude for her support and encouragement through my life. This dissertation is dedicated to her.

Chapter 1

Density Functional Perturbation Theory

1.1 Introduction

The theory of lattice vibrations is one of the best established chapters in modern solid-state physics. A wide variety of physical properties of solids depend on their lattice-dynamical behavior. Infrared spectroscopy, elastic neutron scattering, specific heat, heat conduction, and electron-phonon interaction related behaviors such as superconductivity are among the list of them (see [5] for a review). The understanding of phonons is considered to be one of the most convincing pieces of evidence that our current quantum picture of solids is correct.

The early theory of lattice vibrations dates back to the thirties in the twenties century, in which the formulations were mainly concerned with establishing the general properties of the dynamical matrices without even considering their connections with the electronic properties that determine them. It is actually important to exploit the relationship of the electronic and the lattice-dynamical properties of a system as it is only possible then to calculate the lattice-dynamical properties of the system.

Pioneered by Hohenberg and Kohn, first established by Kohn and Sham, the Kohn-Sham density functional theory is by far the most widely used electronic structure theory and made it possible for calculating specific properties of specific (simple) materials using *ab initio* quantum-mechanical techniques whose only input information is the chemical composition of the materials. In the specific case of lattice-dynamical properties, a large number of *ab initio* calculations based on the linear response theory of lattice vibrations have been made possible by the development of density functional perturbation theory based on Kohn-Sham Density functional theory.

Density functional perturbation theory (DFPT) [3, 21, 5, 11] studies the response of a quantum system under small perturbation, where the quantum system is described at the level of first principle electronic structure theories such as Kohn-Sham density functional theory (KSDFT) [26, 31]. One important application of DFPT is the calculation of vibration

properties such as phonons, which can be further used to calculate many physical properties . DFPT describes vibration properties through a polarizability operator, which characterizes the linear response of the electron density with respect to the perturbation of the external potential. More specifically, in vibration calculations, the polarizability operator needs to be applied to $d \times N_A \sim \mathcal{O}(N_e)$ perturbation vectors, where d is the spatial dimension (usually $d = 3$), N_A is the number of atoms, and N_e is the number of electrons. In general the complexity for solving KSDFT is $\mathcal{O}(N_e^3)$, while the complexity for solving DFPT is $\mathcal{O}(N_e^4)$. It is possible to reduce the computational complexity of DFPT calculations by "linear scaling methods" [19, 45, 8]. Such methods can be successful in reducing the computational cost for systems of large sizes with substantial band gaps, but this can be challenging for medium-sized systems with relatively small band gaps.

In the discussion below, we will slightly abuse the term "phonon calculation" to refer to calculation of vibration properties of condensed matter systems as well as isolated molecules. In order to apply the polarizability operator to $\mathcal{O}(N_e)$ vectors, we need to solve $\mathcal{O}(N_e^2)$ coupled Sternheimer equations. On the other hand, when a constant number of degrees of freedom per electron is used, the size of the Hamiltonian matrix is only $\mathcal{O}(N_e)$. Hence asymptotically there is room to obtain a set of only $\mathcal{O}(N_e)$ "compressed perturbation vectors", which encodes essentially all the information of the $\mathcal{O}(N_e^2)$ Sternheimer equations.

In the first chapter, we include the minimum details of Kohn-Sham density functional theory, density functional perturbation theory, for the purpose of phonon calculation. The rest of the chapter is organised as follows. Section 1.2 briefly introduces the basic components of the Kohn-Sham density functional theory, followed by section 1.3 for the self-consistent field iteration and section 1.4 for more details of density matrix. Section 1.5 briefly introduces the basics of linear response theory, which is applied to Kohn-Sham density functional theory and hence lead to the discussion of density functional perturbation theory in section 1.6. Section 1.7 introduces the calculation of phonon frequency as an important application of DFPT, which will be discussed in detail through this dissertation.

1.2 Kohn-Sham Density Functional Theory

In this section, we briefly review the formulation of Kohn-Sham Density Functional Theory. It is by far the most widely used electronic structure theory, which achieves the best compromise between accuracy and efficiency. Having full knowledge of the arrangement of the electrons is the foundation and the first step for the calculation of phonon and other properties.

1.2.1 Quantum many body problem and Born-Oppenheimer approximation

The microscopic properties of electrons in chemistry, biology and material science are described by the many body Hamiltonian of the Schödinger equation. The many body Hamil-

tonian with N_A nuclei and N_e electrons is

$$\begin{aligned} H &= \sum_{i=1}^{N_e} -\frac{1}{2}\Delta_{\mathbf{r}_i} + \sum_{i=1}^{N_e} V_{\text{ext}}(\mathbf{r}_i; \{\mathbf{R}_I\}) + \sum_{i<j}^{N_e} \frac{1}{|\mathbf{r}_i - \mathbf{r}_j|} + \sum_{I<J}^{N_A} \frac{Z_I Z_J}{|\mathbf{R}_I - \mathbf{R}_J|} \\ &\equiv T + V_{\text{en}} + V_{\text{ee}} + E_{\text{II}}, \end{aligned} \tag{1.1}$$

where the Hamiltonian is partitioned into kinetic, electron-ion interaction, electron-electron interaction, and ion-ion interaction respectively:

$$\begin{aligned} T &= \sum_{i=1}^{N_e} -\frac{1}{2}\Delta_{\mathbf{r}_i}, \quad V_{\text{en}} = \sum_{i=1}^{N_e} V_{\text{ext}}(\mathbf{r}_i; \{\mathbf{R}_I\}) \\ V_{\text{ee}} &= \sum_{i<j}^{N_e} \frac{1}{|\mathbf{r}_i - \mathbf{r}_j|}, \quad E_{\text{II}} = \sum_{I<J}^{N_A} \frac{Z_I Z_J}{|\mathbf{R}_I - \mathbf{R}_J|}. \end{aligned} \tag{1.2}$$

Here $\{\mathbf{R}_I\}$ are the positions of the nuclei, $\{\mathbf{r}_i\}$ are the spatial coordinates of the electrons. $\{Z_I\}$ are the charge of the nuclei. This is a convention we follow throughout this dissertation unless otherwise stated, that $\mathbf{R}$ is for position of a nucleus, whereas $\mathbf{r}$ stands for coordinates of the electron.

In principle, the many body Hamiltonian 1.1 contains all the information of the system. But in most cases, for a quantum many body system, the ground state is often the most important state. It is characterized by the smallest eigenvalue and eigenvector of the many body Hamiltonian:

$$H\Psi = E\Psi. \tag{1.3}$$

(1.3) is referred to as the quantum many body problem. E is called the ground state energy of the many body system, and Ψ is called the ground state wavefunction. According to the Pauli's exclusion principle for the identical electrons, Ψ changes sign if any pair of coordinates $\mathbf{r}_i$

For a system containing both nuclei and electrons, all particles are quantum particles and should be characterized by quantum mechanics. Using the fact that the mass of the electron is much smaller compared to a nuclei of any element in the periodic table(around 0.0005 of hydrogen), Born and Oppenheimer proposed the adiabatic approximation that the nuclei can be described by classical mechanics. The Born-Oppenheimer (BO) approximation [7] separates the complexity due to the electrons and that due to the nuclei.

Under the BO approximation, the nuclei have a set of fixed positions $\{\mathbf{R}_I\}_{I=1}^{N_A}$, which is called the atomic configuration. Note that under this assumption, the ion-ion interaction then become a constant shift to the Hamiltonian.

Before we move on to the Kohn-Sham density functional theory, we introduce another point of view of the quantum many body problem (1.3) from the minimization point of view. The Courant-Fisher minimax theorem states that eigenvalue problem (1.3) is equivalent to the following optimization problem

$$E = \inf_{|\Psi\rangle \in \mathcal{A}_N, \langle\Psi|\Psi\rangle = 1} \langle \Psi | H | \Psi \rangle \,, \tag{1.4}$$

where $\mathcal{A}_N$ denotes the set of anti-symmetric functions. Eq. (1.4) is the variational principle for ground state in quantum mechanics.

1.2.2 Kohn-Sham Density functional theory (KSDFT)

Born-Oppenheimer approximation reduces the quantum many body problem (1.3) to the electronic structure problem. Still, it appears that one has to know the many body wavefunction Ψ in order to solve the quantum many body problem exactly. However, the fact is that electron density ρ is all one needs to determine the quantum many body ground state, thanks to Hohenberg and Kohn. According to Hohenberg and Kohn[26], no two different potentials acting on the electrons of a given system can give rise to a same ground-state electronic charge density. This theorem provides the foundation of density functional theory (DFT). It provides a huge simplification of the quantum mechanical problem of a system of interacting electrons. It replaces the traditional description based on wavefunctions, which depend on $3N_e$ independent variables, with a much more tractable one in terms of the charge density ρ.

The most widely used form of the density functional theory is called the Kohn-Sham density functional theory (KSDFT)[31]. In the following discussion, we briefly introduce the setup of KSDFT, including Kohn-Sham energy functional, Kohn-Sham equations, pseudopotential setup, and other related concepts. In section 1.2.2.1, the setup in zero temperature is first visited. Meanwhile in section 1.2.2.2, the generalization of KSDFT for system in finite temperature is introduced.

1.2.2.1 Zero Temperature

Consider a system consisting of N_A nuclei and N_e electrons. In the Born-Oppenheimer approximation, for each set of nuclear positions $\{\mathbf{R}_I\}_{I=1}^{N_A}$, the electrons are relaxed to their ground state. The ground state total energy is denoted by $E_{\text{tot}}(\{\mathbf{R}_I\}_{I=1}^{N_A})$, and can be computed in Kohn-Sham density functional theory [26, 31] according to the minimization of the following Kohn-Sham energy functional

$$\begin{aligned} E_{\mathrm{KS}}(\{\psi_i\};\{\mathbf{R}_I\}) =& \frac{1}{2}\sum_{i=1}^{N_e}\int |\nabla\psi_i(\mathbf{r})|^2\,\mathrm{d}\mathbf{r} + \int V_{\mathrm{ion}}(\mathbf{r};\{\mathbf{R}_I\})\rho(\mathbf{r})\,\mathrm{d}\mathbf{r} \\ &+ \frac{1}{2}\iint v_c(\mathbf{r},\mathbf{r}')\rho(\mathbf{r})\rho(\mathbf{r}')\,\mathrm{d}\mathbf{r}\,\mathrm{d}\mathbf{r}' + E_{\mathrm{xc}}[\rho] + E_{\mathrm{II}}(\{\mathbf{R}_I\}). \end{aligned} \tag{1.5}$$

Here the minimization is with respect to the Kohn-Sham orbitals $\{\psi_i\}_{i=1}^{N_e}$ satisfying the orthonormality condition

$$\int \psi_i^*(\mathbf{r})\psi_j(\mathbf{r})\,\mathrm{d}\mathbf{r} = \delta_{ij}, \quad i,j = 1,\ldots,N_e.$$

In Eq. (1.5), $\rho(\mathbf{r}) = \sum_{i=1}^{N_e}|\psi_i(\mathbf{r})|^2$ defines the electron density. In the discussion below we will omit the range of indices I, i unless otherwise specified. In Eq. (1.5),

$$v_c(\mathbf{r},\mathbf{r}') = \frac{1}{|\mathbf{r}-\mathbf{r}'|} \tag{1.6}$$

defines the kernel for Coulomb interaction in $\mathbb{R}^3$. V_{ion} is a local potential characterizing the electron-ion interaction in all-electron calculations, and is independent of the electronic states $\{\psi_i\}$. More specifically, V_{ion} is the summation of local potentials from each atom I

$$V_{\mathrm{ion}}(\mathbf{r};\{\mathbf{R}_I\}) = \sum_I V_{\mathrm{loc},I}(\mathbf{r}-\mathbf{R}_I). \tag{1.7}$$

In a pseudopotential approximation, $V_{\mathrm{loc},I}(\mathbf{r}-\mathbf{R}_I)$ is defined as

$$V_{\mathrm{loc},I}(\mathbf{r}-\mathbf{R}_I) := \int v_c(\mathbf{r},\mathbf{r}')m_I(\mathbf{r}'-\mathbf{R}_I)\,\mathrm{d}\mathbf{r}', \tag{1.8}$$

where m_I is a localized function in the real space and is called a pseudocharge [40, 48]. The normalization condition for each pseudocharge is $\int m_I(\mathbf{r})\,\mathrm{d}\mathbf{r} = -Z_I$, and Z_I is the atomic charge for the I-th atom. The total pseudocharge is defined as $m(\mathbf{r}) = \sum_I m_I(\mathbf{r}-\mathbf{R}_I)$. We assume the system is charge neutral, i.e.

$$\int m(\mathbf{r})\,\mathrm{d}\mathbf{r} = -\sum_I Z_I = -N_e.$$

E_{xc} is the exchange-correlation energy, and here we assume semi-local functionals such as local density approximation (LDA) [12, 50] and generalized gradient approximation (GGA) functionals [6, 32, 49] are used. The last term in Eq. (1.5) is the ion-ion Coulomb interaction energy. For isolated clusters in 3D,

$$E_{\mathrm{II}}(\{\mathbf{R}_I\}) = \frac{1}{2}\sum_{I\neq J}\frac{Z_I Z_J}{|\mathbf{R}_I - \mathbf{R}_J|}. \tag{1.9}$$

We also note that for extended systems, modeled as infinite periodic structures, all the terms with Coulomb kernel require special treatment in order to avoid divergence due to the long-range $1/r$ nature of the Coulomb interaction [40].

The Euler-Lagrange equation associated with the Kohn-Sham energy functional gives rise to the Kohn-Sham equations as

$$\begin{aligned} H[\rho]\psi_i &= \left(-\frac{1}{2}\Delta + \mathcal{V}[\rho]\right)\psi_i = \varepsilon_i\psi_i \\ &\int \psi_i^*(\mathbf{r})\psi_j(\mathbf{r})\,\mathrm{d}\mathbf{r} = \delta_{ij}, \\ \rho(\mathbf{r}) &= \sum_{i=1}^{N_e}|\psi_i(\mathbf{r})|^2. \end{aligned} \tag{1.10}$$

Here the eigenvalues $\{\varepsilon_i\}$ are ordered non-decreasingly. $\psi_1, \ldots, \psi_{N_e}$ are called the occupied orbitals, while $\psi_{N_e+1}, \ldots$ are called the unoccupied orbitals. ψ_{N_e} is often referred to as the highest occupied molecular orbital (HOMO), and ψ_{N_e+1} the lowest unoccupied molecular orbital (LUMO). The difference of the corresponding eigenvalues $\varepsilon_g = \varepsilon_{N_e+1} - \varepsilon_{N_e}$ defines the HOMO-LUMO gap. A system with finite gap is called an insulating system or an insulator, whereas a system with no gap $\varepsilon_g = 0$ is called a metallic system, or a metal. The intermediate state where the gap is not zero but considerably small, the system is referred to as the semiconducting system, or a semiconductor.

For a given electron density ρ, the effective potential $\mathcal{V}[\rho]$ is

$$\begin{aligned} \mathcal{V}[\rho](\mathbf{r}) &= V_{\mathrm{ion}}(\mathbf{r};\{\mathbf{R}_I\}) + \int v_c(\mathbf{r},\mathbf{r}')\rho(\mathbf{r}')\,\mathrm{d}\mathbf{r}' + V_{\mathrm{xc}}[\rho](\mathbf{r}) \\ &= \int v_c(\mathbf{r},\mathbf{r}')(\rho(\mathbf{r}') + m(\mathbf{r}'))\,\mathrm{d}\mathbf{r}' + V_{\mathrm{xc}}[\rho](\mathbf{r}). \end{aligned} \tag{1.11}$$

Here

$$V_{\mathrm{xc}}[\rho](\mathbf{r}) = \frac{\delta E_{\mathrm{xc}}}{\delta\rho(\mathbf{r})} \tag{1.12}$$

is the exchange-correlation potential, which is the functional derivative of the exchange-correlation energy with respect to the electron density. The Kohn-Sham Hamiltonian depends nonlinearly on the electron density ρ, and the electron density should be solved self-

consistently. When the Kohn-Sham energy functional E_{KS} achieves its minimum, the self-consistency of the electron density is simultaneously achieved. Then the total energy can be equivalently computed as [40]

$$\begin{aligned} E_{\mathrm{tot}} =& \sum_{i=1}^{N_e} \varepsilon_i - \frac{1}{2} \iint v_c(\mathbf{r}, \mathbf{r}') \rho(\mathbf{r}) \rho(\mathbf{r}') \, \mathrm{d}\mathbf{r} \, \mathrm{d}\mathbf{r}' \\ & - \int V_{\mathrm{xc}}[\rho](\mathbf{r}) \rho(\mathbf{r}) \, \mathrm{d}\mathbf{r} + E_{\mathrm{xc}}[\rho] + E_{\mathrm{II}}(\{\mathbf{R}_I\}). \end{aligned} \tag{1.13}$$

Here $E_{\mathrm{band}} = \sum_{i=1}^{N_e} \varepsilon_i$ is referred to as the band energy.

1.2.2.2 Finite temperature

In this section, we introduce the extension of density functional theory formulation to the finite temperature setup to include thermal effects. This is formulated first by Mermin [41]. In this setup, we consider a system of finite size with periodic boundary conditions. This can be used to model isolated molecular systems as well as solid state systems with the Gamma point sampling strategy of the Brillouin zone [40]. However, we do not explicitly take advantage that $\{\psi_i(\mathbf{r})\}$ are real, so that the formulation is applicable to real space and Fourier space implementation, as commonly done in electronic structure software packages. The spatial dimension $d = 3$ is assumed in the treatment of e.g. Coulomb interaction unless otherwise specified. Since our numerical results involve real materials and systems of both insulating and metallic characters, we include relevant technical details such as nonlocal pseudopotential and temperature dependence in the discussion. Note that the discussion overlap with section 1.2.2.1 by a lot. For the completion of the discussion for the setup of KSDFT, the overlapping details are also mentioned in place.

Consider a system consisting of N_A nuclei and N_e electrons at temperature $T = 1/(k_B\beta)$, where k_B is the Boltzmann constant and β is the inverse temperature. In the Born-Oppenheimer approximation, for each set of nuclear positions $\{\mathbf{R}_I\}_{I=1}^{N_A}$, the electrons are relaxed to their ground state. The ground state total energy is denoted by $E_{\mathrm{tot}}(\{\mathbf{R}_I\}_{I=1}^{N_A})$, and can be computed in Kohn-Sham density functional theory [26, 31, 41] according to the minimization of the following Kohn-Sham-Mermin energy functional

$$\begin{aligned} & E_{\mathrm{KS}}(\{\psi_i\}; \{\mathbf{R}_I\}) \\ =& \frac{1}{2} \sum_{i=1}^{\infty} f_i \int |\nabla \psi_i(\mathbf{r})|^2 \, \mathrm{d}\mathbf{r} + \sum_{i=1}^{\infty} f_i \int \psi_i^*(\mathbf{r}) V_{\mathrm{ion}}(\mathbf{r}, \mathbf{r}'; \{\mathbf{R}_I\}) \psi_i(\mathbf{r}') \, \mathrm{d}\mathbf{r} \, \mathrm{d}\mathbf{r}' \\ & + \frac{1}{2} \iint v_c(\mathbf{r}, \mathbf{r}') \rho(\mathbf{r}) \rho(\mathbf{r}') \, \mathrm{d}\mathbf{r} \, \mathrm{d}\mathbf{r}' + E_{\mathrm{xc}}[\rho] + E_{\mathrm{II}}(\{\mathbf{R}_I\}) \\ & + \frac{1}{\beta} \sum_{i=1}^{\infty} \left[f_i \log f_i + (1 - f_i) \log(1 - f_i) \right]. \end{aligned} \tag{1.14}$$

Here the minimization is with respect to the Kohn-Sham orbitals $\{\psi_i\}_{i=1}^{\infty}$ satisfying the orthonormality condition

$$\int \psi_i^*(\mathbf{r})\psi_j(\mathbf{r})\,\mathrm{d}\mathbf{r} = \delta_{ij}, \tag{1.15}$$

as well as the occupation numbers $\{f_i\}_{i=1}^{\infty}$ satisfying $0 \le f_i \le 1$. In Eq. (1.14),

$$\rho(\mathbf{r}) = \sum_{i=1}^{\infty} f_i \left|\psi_i(\mathbf{r})\right|^2 \tag{1.16}$$

defines the electron density with normalization condition

$$\int \rho(\mathbf{r})\,\mathrm{d}\mathbf{r} = N_e. \tag{1.17}$$

In the discussion below we will omit the range of indices I, i unless otherwise specified. In Eq. (1.14), $v_c(\mathbf{r},\mathbf{r}') = \frac{1}{|\mathbf{r}-\mathbf{r}'|}$ is the kernel for Coulomb interaction in $\mathbb{R}^3$ and the corresponding term is called the Hartree energy. V_{ion} is a collection of local and nonlocal potential characterizing the electron-ion interaction, and is independent of the electronic states $\{\psi_i\}$. More specifically, in a pseudopotential approximation [40], if we view V_{ion} as an integral operator, then the kernel of V_{ion} can be expressed as the summation of contribution from each atom I

$$\begin{aligned} V_{\text{ion}}(\mathbf{r},\mathbf{r}';\{\mathbf{R}_I\}) &= \sum_I V_{\text{loc},I}(\mathbf{r}-\mathbf{R}_I)\delta(\mathbf{r}-\mathbf{r}') + \sum_I V_{\text{nl},I}(\mathbf{r}-\mathbf{R}_I,\mathbf{r}'-\mathbf{R}_I) \\ &\equiv V_{\text{loc}} + V_{\text{nl}}. \end{aligned} \tag{1.18}$$

Here $V_{\text{loc},I}$ is the local pseudopotential as introduced in (1.8), and $V_{\text{nl},I}$ the nonlocal pseudopotential. In the Kleinman-Bylander form [28], each nonlocal pseudopotential is a low rank and symmetric operator with kernel

$$V_{\text{nl},I}(\mathbf{r}-\mathbf{R}_I,\mathbf{r}'-\mathbf{R}_I) = \sum_{l=1}^{L_I} \gamma_{I,l} b_{I,l}(\mathbf{r}-\mathbf{R}_I) b_{I,l}^*(\mathbf{r}'-\mathbf{R}_I). \tag{1.19}$$

Here $\gamma_{I,l}$ is a weight factor, and each $b_{I,l}(\mathbf{r})$ is a real valued function compactly supported around $\mathbf{r} = 0$. E_{xc} is the exchange-correlation energy, and here we assume semi-local functionals such as local density approximation (LDA) [12, 50] and generalized gradient approximation (GGA) functionals [6, 32, 49] are used. E_{II} is the ion-ion Coulomb interaction energy as introduced in (1.9)

$$E_{\mathrm{II}}(\{\mathbf{R}_I\}) = \frac{1}{2}\sum_{I\neq J}\frac{Z_I Z_J}{|\mathbf{R}_I - \mathbf{R}_J|}, \tag{1.20}$$

while for periodic systems the contribution from all the image charges should be properly taken into account via e.g. the Ewald summation technique [54]. The last term of Eq. (1.14) is the entropy term related to the temperature. Again, spin degeneracy is neglected for simplicity of the notation.

The Euler-Lagrange equation associated with the Kohn-Sham energy functional gives rise to the Kohn-Sham equations as

$$\begin{aligned}
&H[\rho]\psi_i = \left(-\frac{1}{2}\Delta + \mathcal{V}[\rho]\right)\psi_i = \varepsilon_i\psi_i,\\
&\int \psi_i^*(\mathbf{r})\psi_j(\mathbf{r})\,\mathrm{d}\mathbf{r} = \delta_{ij},\\
&\rho(\mathbf{r}) = \sum_{i=1}^{\infty} f_i\left|\psi_i(\mathbf{r})\right|^2,\\
&f_i = \frac{1}{1+e^{\beta(\varepsilon_i-\mu)}}.
\end{aligned} \tag{1.21}$$

Here the eigenvalues $\{\varepsilon_i\}$ are ordered non-decreasingly. Note that the occupation number f_i is given analytically by the Fermi-Dirac distribution with respect to the eigenvalue ε_i, and μ is a Lagrange multiplier enforcing the normalization condition of the electron density. The difference of the eigenvalues $\varepsilon_g = \varepsilon_{N_e+1} - \varepsilon_{N_e}$ defines the energy gap. If ε_g is positive then the system is called an insulating system, and otherwise a metallic system. For insulating systems, $\psi_1, \ldots, \psi_{N_e}$ are called the occupied orbitals, while $\psi_{N_e+1}, \ldots$ are called the unoccupied orbitals. ψ_{N_e} is often referred to as the highest occupied molecular orbital (HOMO), and ψ_{N_e+1} the lowest unoccupied molecular orbital (LUMO).

The effective potential $\mathcal{V}[\rho]$ depends on the electron density ρ as

$$\mathcal{V}[\rho](\mathbf{r},\mathbf{r}') = V_{\mathrm{ion}}(\mathbf{r},\mathbf{r}') + \left[\int v_c(\mathbf{r},\mathbf{r}')\rho(\mathbf{r}')\,\mathrm{d}\mathbf{r}' + V_{\mathrm{xc}}[\rho](\mathbf{r})\right]\delta(\mathbf{r}-\mathbf{r}'); \tag{1.22}$$

$$V_{\mathrm{xc}}[\rho](\mathbf{r}) = \frac{\delta E_{\mathrm{xc}}}{\delta\rho(\mathbf{r})}. \tag{1.23}$$

Here $V_{\mathrm{xc}}[\rho](\mathbf{r})$ is the exchange-correlation potential, which is the functional derivative of the exchange-correlation energy with respect to the electron density. The Kohn-Sham Hamiltonian depends nonlinearly on the electron density ρ, and the electron density should be solved self-consistently. When the Kohn-Sham energy functional E_{KS} achieves its minimum, the self-consistency of the electron density is simultaneously achieved. Note that both the

Hartree potential and the exchange-correlation potential are local potentials. This plays an important role in simplifying the density functional perturbation theory.

When the Kohn-Sham energy functional E_{KS} achieves its minimum, the self-consistency of the electron density is simultaneously achieved. Then the total energy can be equivalently computed as [40]

$$\begin{aligned} E_{\mathrm{tot}} = & \sum_{i=1}^{N_e} \varepsilon_i - \frac{1}{2} \iint v_c(\mathbf{r}, \mathbf{r}') \rho(\mathbf{r}) \rho(\mathbf{r}') \, \mathrm{d}\mathbf{r} \, \mathrm{d}\mathbf{r}' \\ & - \int V_{\mathrm{xc}}[\rho](\mathbf{r}) \rho(\mathbf{r}) \, \mathrm{d}\mathbf{r} + E_{\mathrm{xc}}[\rho] + E_{\mathrm{II}}(\{\mathbf{R}_I\}). \end{aligned} \tag{1.24}$$

Here $E_{\mathrm{band}} = \sum_{i=1}^{N_e} \varepsilon_i$ is referred to as the band energy.

At this point, it is worth noted that the Kohn-Sham Hamiltonian depends nonlinearly on the electron density, and the electron density should be solved self-consistently, where the details are discussed in section 1.3.

Before we finish the discussion of KSDFT, note that this energy functional (1.14) is indeed a generalization of the zero temperature case as in (1.5): when $T \to 0$, $\beta \to \infty$, meanwhile the occupation numbers f_i are either 1 for occupied states or 0 for the unoccupied states. Hence the entropy term is just 0. On the other hand, V_{ion} defined in Eq. (1.18) is taking the nonlocal pseudopotential into account, which is an extension of Eq. (1.7) where the nonlocal pseodopotential is not considered. In the rest of the this dissertation, we will follow the setup in this section and show the results in finite temperature if not otherwise stated.

1.3 Self-consistent field iteration

In section 1.2, KSDFT is introduced with exchange-correlation given as pure density functionals. The Kohn-Sham Hamiltonian depends nonlinealy on the electron density ρ, and the electron density should be solved self-consistently. In this section, we show the details of solving the Kohn-Sham equatinos.

The map from the effective potential $\mathcal{V}$ to the electron density ρ is called the Kohn-Sham map, denoted by

$$\rho = \mathcal{F}_{\mathrm{KS}}[V]. \tag{1.25}$$

By solving a linear eigenvalue problem, the electron density can be evaluated. So ρ and $\mathcal{V}$ should be iteratively determined by each other till convergence. This is called the self-consistent field (SCF) iteration.

Starting from certain initial electron density denoted by ρ_0, with $\rho_k, \mathcal{V}_k$ denoting the electron density and the effective potential at the k-th SCF iteration, respectively, the SCF iteration becomes

$$\cdots \to \rho_k \to V_k = \mathcal{V}[\rho_k] \to \rho_{k+1} \to V_{k+1} = \mathcal{V}[\rho_{k+1}] \to \cdots \tag{1.26}$$

The relation (1.26) can be viewed as a mapping either from ρ_k to ρ_{k+1}, or from V_k to V_{k+1}. These two viewpoints are called density mixing and potential mixing, respectively. There is no qualitative difference between these two types of mixing schemes. In the sections 2.4 and 3.4 where numerical examples are discussed, potential mixing is used in the calculations. We remark that both mixing schemes are widely used in electronic structure software packages, and the Anderson's method to be discussed below can be used for density mixing as well.

When self-consistency is reached, the converged effective potential is denoted by V^* and satisfies the nonlinear equation

$$V^* = \mathcal{V}[\rho] = \mathcal{V}[\mathcal{F}_{\mathrm{KS}}[V^*]]. \tag{1.27}$$

The simplest version of the SCF iteration is the fixed point iteration, where the potential at the $(k+1)$-th step is directly given by the output potential at the k-th step

$$V_{k+1} = \mathcal{V}[\mathcal{F}_{\mathrm{KS}}[V_k]]. \tag{1.28}$$

However, the simple fixed point iteration generally cannot be expected to converge, as the map $V_k \mapsto V_{k+1}$ in Eq. (1.28) is generally not a contraction map. A slight modification of the fixed point iteration is more practically feasible, which is written as

$$V_{k+1} = \alpha \mathcal{V}[\mathcal{F}_{\mathrm{KS}}[V_k]] + (1-\alpha)V_k. \tag{1.29}$$

If we denote the residual error of the potential as

$$r_k = V_k - \mathcal{V}[\mathcal{F}_{\mathrm{KS}}[V_k]], \tag{1.30}$$

then the simple mixing scheme is written as

$$V_{k+1} = V_k - \alpha r_k. \tag{1.31}$$

Following this setup, a more widely used quasi-Newton type of method is called Broyden's method, which replaces α in Eq. 1.31 by C_k. The scheme reads

$$V_{k+1} = V_k - C_k r_k. \tag{1.32}$$

Note that here C_k is an approximate matrix that should be easy to compute and to apply. Specifically, Andersons method [2], as a variant of Broyden's method, is widely used in electronic structure software packages. Using Broyden's technique [27], C_k is obtained by

a sequence of low-rank updates to a certain approximation C_0 of the Jacobian inverse J_k^{-1} using a recursive formula [16, 39] derived from the constrained optimization problem

$$\min_{C} \quad \frac{1}{2}\|C - C_{k-1}\|_F^2 \tag{1.33}$$

$$\text{s.t.} \quad S_k = CY_k, \tag{1.34}$$

where C_{k-1} is the approximation to the Jacobian in the $(k-1)$-th iteration. Here the Jacobian matrix J_k is with respect to the residual map

$$\delta V \mapsto \delta V - \mathcal{V}[\mathcal{F}_{\text{KS}}[V_k + \delta V]]. \tag{1.35}$$

Matrices S_k and Y_k in Eq. (1.34) are defined as

$$S_k = (s_k, s_{k-1}, \ldots, s_{k-l}), \quad Y_k = (y_k, y_{k-1}, \ldots, y_{k-l}), \tag{1.36}$$

where s_j and y_j are defined by $s_j = V_j - V_{j-1}$ and $y_j = r_j - r_{j-1}$, respectively. Here the number l is the length of history used in Broyden's method.

Note that the difference of Anderson's method to Broyden's method is that it is replacing C_{k-1} by a fixed C_0 in Eq. (1.33). Solving the constrained minimization problem in Eq. (1.33) using the method of Lagrange multipliers, one get the solution

$$C_k = C_{k-1} + (S_k - C_{k-1}Y_k)Y_k^\dagger, \tag{1.37}$$

which is the update scheme used in Broyden's method. Here $Y_k^\dagger$ denotes the Moore-Penrose pseudoinverse of Y_k, i.e. $Y_k^\dagger = (Y_k^T Y_k)^{-1} Y_k^T$. Replacing C_{k-1} by C_0 in Eq. (1.37) and plug into Eq. (1.32), we arrive at the update scheme of Anderson's method

$$V_k = V_{k-1} - C_0(I - Y_k Y_k^\dagger)r_k - S_k Y_k^\dagger r_k. \tag{1.38}$$

Particularly, C_0 is chosen to be αI, we obtain Anderson's method

$$V_k = V_{k-1} - \alpha(I - Y_k Y_k^\dagger)r_k - S_k Y_k^\dagger r_k. \tag{1.39}$$

This is the method that is commonly used in KSDFT solvers, and is used in the numerical examples tested in this dissertation.

1.4 Density matrix formulation

Density matrix is a central object in electronic structure theory. More specifically, density matrix formulation is a more intrinsic way of constructing the Kohn-Sham equations. In terms of numerical algorithms, the usage of density matrix is also preferable, especially for large scale problems. In this section, we visit the density matrix formulation for both the zero temperature case and the finite temperature case.

In the Kohn-Sham equations (1.10), orbitals $\{\psi_i\}$ are defined. At the same time, density matrix can be defined mathematically as

$$P(\mathbf{r}', \mathbf{r}) = \sum_{i=1}^{N_e} \psi_i^*(\mathbf{r}')\psi_i(\mathbf{r}). \tag{1.40}$$

Note that the electron density takes the diagonal elements of the density matrix

$$\rho(\mathbf{r}) = P(\mathbf{r}, \mathbf{r}) = \sum_{i=1}^{N_e} \psi_i^*(\mathbf{r})\psi_i(\mathbf{r}). \tag{1.41}$$

One important point is that the density matrix can also be equivalently defined using contour integrals from complex analysis using Cauchy integral formula

$$P = \frac{1}{2\pi\iota} \oint_{\mathcal{C}} (\lambda - H)^{-1} \, \mathrm{d}\lambda, \tag{1.42}$$

where H is the Hamiltonian defined in Eq. (1.10); C is a contour which encloses all occupied states $\varepsilon_{i\,i=1}^{N_e}$ only. Such contour always exists whenever a gap is present. This means that this contour integral formulation (1.42) is only valid for insulator and semiconductor.

On the other hand, when the finite temperature is considered, using the Kohn-Sham equations (1.21) in which the orbitals are defined, density matrix can be defined mathematically as

$$P(\mathbf{r}', \mathbf{r}) = \sum_{i=1}^{\infty} f_i \psi_i^*(\mathbf{r}')\psi_i(\mathbf{r}). \tag{1.43}$$

Note that the corresponding electron density still takes the diagonal elements of the density matrix

$$\rho(\mathbf{r}) = P(\mathbf{r}, \mathbf{r}) = \sum_{i=1}^{\infty} f_i \psi_i^*(\mathbf{r})\psi_i(\mathbf{r}). \tag{1.44}$$

Also note that in Eq. (1.43), the summation involve only finite number of terms, as the occupation number f_i goes to zero.

The density matrix can also be equivalently defined using contour integrals from complex analysis using Cauchy integral formula

$$P = \frac{1}{2\pi\iota} \oint_{\mathcal{C}} f_\beta(\lambda - \mu)(\lambda - H)^{-1} \, \mathrm{d}\lambda, \tag{1.45}$$

where H is the Hamiltonian defined in Eq. (1.21); f_β is the Fermi-Dirac function

$$f_\beta(z) = \frac{1}{1 + \exp(\beta z)}; \tag{1.46}$$

C is a contour which encloses the entire spectrum of H as well as close to the real axis so that it is away from the singular points of the Fermi-Dirac function.

The contour integral formalism provides a way for numerical approximation of the density matrix. The discretized contour integral with proper choice of quadrature nodes and weights would give an approximation of the density matrix with fair precision. [ZX:Figure as the contour.].

1.5 Linear response theory

Many properties of chemical or material systems are characterized by how they respond to external perturbations. Mathematically, when the external perturbation is small, only the leading order perturbation is important. This is known as the linear response regime. In this section, we discuss the basics of the linear response theory, for preparation of introducing density functional perturbation theory in Section 1.6.

1.5.1 Perturbation of the density matrix

For a fixed Hamiltonian H, consider the perturbation of the density matrix. The contour integral representation of the density matrix with finite temperature reads

$$P_0 = \frac{1}{2\pi i} \oint_{\mathcal{C}} f(z)(z - H)^{-1} \, \mathrm{d}z. \tag{1.47}$$

Consider that the Hamiltonian is perturbed to $H_\varepsilon = H_0 + \varepsilon\mathfrak{g}$, in which the operator norm of $\mathfrak{g}$ is bounded. As $\mathcal{C}$ lies in the resolvent set of H_0, we assume that when ε is small and so is the perturbation, the perturbed density matrix P_ε can be still computed using the same contour as

$$P_\varepsilon = \frac{1}{2\pi i} \oint_{\mathcal{C}} f(z)(z - H_\varepsilon)^{-1} \, \mathrm{d}z. \tag{1.48}$$

Then we have

$$\begin{aligned} P_\varepsilon - P_0 &= \frac{1}{2\pi i} \oint_{\mathcal{C}} f(z) \left[(z - H_\varepsilon)^{-1} - (z - H)^{-1} \right] \mathrm{d}z \\ &= \frac{1}{2\pi i} \oint_{\mathcal{C}} f(z) \left[(z - H_\varepsilon)^{-1} \varepsilon \mathfrak{g} (z - H)^{-1} \right] \mathrm{d}z \\ &= \frac{1}{2\pi i} \oint_{\mathcal{C}} f(z) \left[(z - H)^{-1} \varepsilon \mathfrak{g} (z - H)^{-1} \right] \mathrm{d}z + \mathcal{O}(\varepsilon^2). \end{aligned} \tag{1.49}$$

The last line comes from the Neumann expansion of $(z - H_\varepsilon)^{-1}$,

$$(z - H_\varepsilon)^{-1} = (z - H)^{-1} \sum_{n=0}^{\infty} \left(\varepsilon \mathfrak{g} (z - H)^{-1} \right)^n. \tag{1.50}$$

Define an operator $\mathfrak{X}_0$ as

$$\mathfrak{X}_0 \mathfrak{g} = \frac{1}{2\pi i} \oint_{\mathcal{C}} f(z) \left[(z - H)^{-1} \mathfrak{g} (z - H)^{-1} \right] \mathrm{d}z, \tag{1.51}$$

we arrive at

$$P_\varepsilon - P_0 = \varepsilon \mathfrak{X}_0 \mathfrak{g} + \mathcal{O}(\varepsilon^2). \tag{1.52}$$

If we further note $P(H)$ as the density matrix corresponds to H, we have

$$\left. \frac{\partial P(H + \varepsilon \mathfrak{g})}{\partial \varepsilon} \right|_{\varepsilon = 0} = \mathfrak{X}_0 \mathfrak{g}. \tag{1.53}$$

Mathematically, this means that the Gâteaux derivative of P in the $\mathfrak{g}$ direction is given by the operator $\mathfrak{X}_0 \mathfrak{g}$. In physical terms, the linear response of the density matrix when the potential changes is given by the operator $\mathfrak{X}_0$.

$$\frac{\partial P}{\partial V}(\mathfrak{g}) = \mathfrak{X}_0 \mathfrak{g}. \tag{1.54}$$

Using the spectral decomposition, we have

$$\begin{aligned}
\mathfrak{X}_0\mathfrak{g} &= \frac{1}{2\pi i}\oint_{\mathcal{C}} \sum_{j,k=1}^{\infty} f(z)\left[\frac{\psi_j\psi_j^*\mathfrak{g}\psi_k\psi_k^*}{(z-\varepsilon_j)(z-\varepsilon_k)}\right] \mathrm{d}z \\
&= \frac{1}{2\pi i}\sum_{j,k=1}^{\infty}\oint_{\mathcal{C}} \mathrm{d}z \frac{f(z)}{(z-\varepsilon_j)(z-\varepsilon_k)}\left[\psi_j\psi_j^*\mathfrak{g}\psi_k\psi_k^*\right] \\
&= \sum_{j\neq k}^{\infty}\frac{f_j-f_k}{\varepsilon_j-\varepsilon_k}\left[\psi_j\psi_j^*\mathfrak{g}\psi_k\psi_k^*\right] + \sum_{j}^{\infty} f_j'\left[\psi_j\psi_j^*\mathfrak{g}\psi_j\psi_j^*\right] \\
&= \sum_{j,k}^{\infty}\frac{f_j-f_k}{\varepsilon_j-\varepsilon_k}\left[\psi_j\psi_j^*\mathfrak{g}\psi_k\psi_k^*\right],
\end{aligned} \tag{1.55}$$

where the $\frac{f_j-f_k}{\varepsilon_j-\varepsilon_k}$ is interpreted as the derivative when $j=k$. Eq. (1.55) is called the Adler-Wiser formula [1, 60].

1.5.2 Perturbation of the electron density

In Section 1.5.1, we show the perturbation of the density matrix. The perturbation of electron density, which is of particular interest, follows directly from the definition. As $\rho(\mathbf{r}) = P(\mathbf{r},\mathbf{r})$ is the diagonal of the density matrix, we have

$$\frac{\partial\rho}{\partial V}(\mathfrak{g}) = \mathrm{diag}\left(\mathfrak{X}_0\mathfrak{g}\right) =: \chi_0\mathfrak{g}, \tag{1.56}$$

where χ_0 is defined as

$$\begin{aligned}
\left(\chi_0\mathfrak{g}\right)(\mathbf{r}) =& (\mathfrak{X}_0\mathfrak{g})(\mathbf{r},\mathbf{r}) \\
=& \sum_{j,k}^{\infty}\frac{f_j-f_k}{\varepsilon_j-\varepsilon_k}\left[\psi_j(\mathbf{r})\left(\psi_j^*\mathfrak{g}\psi_k\right)\psi_k^*(\mathbf{r})\right].
\end{aligned} \tag{1.57}$$

Eq. (1.55) is the Adler-Wiser formula for the electron density. The operator χ_0 gives the linear response of the density with respect to the change of the potential.

Before we go into the details, we make remarks on the notation throughout the discussion in this dissertation, as the discussion using the notation $\mathbf{r}, \mathbf{r}', \mathbf{r}''$ etc will quickly become complicated. For simplicity in the discussion below, we will not distinguish the continuous and discretized representations of various quantities. In the case when a discretized representation is needed, we assume that the computational domain is uniformly discretized into a number of grid points $\{\mathbf{r}_\alpha\}_{\alpha=1}^{N_g}$. After discretization all quantities can be called tensors. For example, we will call $u(\mathbf{r})$ an order 1 tensor (or a vector), $A(\mathbf{r},\mathbf{r}')$ an order 2 tensor (or a

matrix), and $\mathfrak{X}(\mathbf{r}, \mathbf{r}'; \mathbf{r}'', \mathbf{r}''')$ an order 4 tensor. The tensor contraction can be denoted using either the continuous or the discrete notation. For example, $\mathfrak{X}(\mathbf{r}, \mathbf{r}; \mathbf{r}'', \mathbf{r}''')$ denotes an order 3 tensor. The tensor contraction between two order 1 tensors u and v should be interpreted as $u^* v = \int u^*(\mathbf{r}) v(\mathbf{r}) \, \mathrm{d}\mathbf{r}$. The tensor contraction between an order 2 tensor A and an order 1 tensor v (i.e. a matrix-vector product) should be interpreted as $(Av)(\mathbf{r}) = \int A(\mathbf{r}, \mathbf{r}') v(\mathbf{r}') \, \mathrm{d}\mathbf{r}'$. Similarly the contraction between an order 2 tensor A and an order 2 tensor $\mathfrak{g}$ (i.e. matrix-matrix product) should be interpreted as $(A\mathfrak{g})(\mathbf{r}, \mathbf{r}') = \int A(\mathbf{r}, \mathbf{r}'') \mathfrak{g}(\mathbf{r}'', \mathbf{r}') \, \mathrm{d}\mathbf{r}''$, and the contraction between an order 4 tensor $\mathfrak{X}$ and an order 2 tensor $\mathfrak{g}$ should be interpreted as

$$(\mathfrak{X}\mathfrak{g})(\mathbf{r}, \mathbf{r}') = \int \mathfrak{X}(\mathbf{r}, \mathbf{r}'; \mathbf{r}'', \mathbf{r}''') \mathfrak{g}(\mathbf{r}'', \mathbf{r}''') \, \mathrm{d}\mathbf{r}'' \, \mathrm{d}\mathbf{r}'''.$$

We also define two operations for order 1 tensors. The Hadamard product of two order 1 tensors $u \odot v$ should be interpreted as $(u \odot v)(\mathbf{r}) = u(\mathbf{r}) v(\mathbf{r})$. For an order 1 tensor $v(\mathbf{r})$, we define an associated order 2 tensor as $(\mathrm{diag}[v])(\mathbf{r}, \mathbf{r}') = v(\mathbf{r}) \delta(\mathbf{r} - \mathbf{r}')$. It is easy to verify the Hadamard product $u \odot v = \mathrm{diag}[u] v$.

1.6 Density functional perturbation theory

In this section, we will apply the result of linear response theory in Section 1.5 to case of Kohn-Sham density functional theory. Note that the effective Hamiltonian depends self-consistently on the electron density. Therefore when we consider the perturbation of the electron density or more generally the perturbation of the density matrix, we also need to take into account the change of the effective potential which is induced by the density perturbation.

Recall that the effective Hamiltonian is defined as $H[\rho] = -\frac{1}{2} + \mathcal{V}[\rho]$, where $\mathcal{V}[\rho]$ is the effective potential defined in Eq. (1.22). Consider a small perturbation to the external potential $V_{\mathrm{ion}}(\mathbf{r}, \mathbf{r}')$, defined as $\mathfrak{g}$. This would induce a change in the electron density and hence the effective potential $\mathcal{V}$ and the effective Hamiltonian H. Mathematically, we apply the chain rule from Eq. (1.22) and then we have

$$\mathfrak{u} := \mathfrak{X}\mathfrak{g} = \frac{\delta P}{\delta \mathcal{V}} \frac{\delta \mathcal{V}}{\delta V_{\mathrm{ion}}} \mathfrak{g} = \mathfrak{X}_0 \mathfrak{g} + \mathfrak{X}_0 \mathfrak{f}_{\mathrm{hxc}} \mathfrak{X} \mathfrak{g} = \mathfrak{X}_0 \mathfrak{g} + \mathfrak{X}_0 \mathfrak{f}_{\mathrm{hxc}} \mathfrak{u}. \tag{1.58}$$

In Eq. (1.58),

$$\begin{aligned} \mathfrak{f}_{\mathrm{hxc}}(\mathbf{r}, \mathbf{r}'; \mathbf{r}'', \mathbf{r}''') =& \left(v_c(\mathbf{r}, \mathbf{r}'') + \frac{\delta V_{\mathrm{xc}}[\rho^*](\mathbf{r})}{\delta \rho(\mathbf{r}')} \right) \delta(\mathbf{r} - \mathbf{r}'') \delta(\mathbf{r}' - \mathbf{r}''') \\ :=& f_{\mathrm{hxc}}(\mathbf{r}, \mathbf{r}') \delta(\mathbf{r} - \mathbf{r}'') \delta(\mathbf{r}' - \mathbf{r}''') \end{aligned} \tag{1.59}$$

is the kernel characterizing the dependence of the $\mathcal{V}$ with respect to the density matrix P

in the linear regime. Here $\frac{\delta V_{\rm xc}[\rho^*](\mathbf{r})}{\delta\rho(\mathbf{r}')}$ is called the exchange-correlation kernel, which is a local operator in the LDA and GGA formulations of the exchange-correlation functionals. $\mathfrak{X}$ is called the reducible polarizability operator, which characterizes the *self-consistent* linear response of the density matrix at $(\mathbf{r},\mathbf{r}')$ with respect to an external nonlocal perturbation of $V_{\rm ion}$ at $(\mathbf{r}',\mathbf{r}''')$. $\mathfrak{X}_0$ is the irreducible polarizability operator. Eq. (1.58) is called the *Dyson equation*, and the solution $\mathfrak{u}$ should be solved self-consistently.

The Dyson equation shows that how the computation of $\mathfrak{X}$ should be obtained through the quantity $\mathfrak{X}_0$. It characterizes the self-consistent linear response of the density matrix with respect to an external nonlocal perturbation of $V_{\rm ion}$. Mathematically, one could solve $\mathfrak{u}$ from Eq.(1.59) as

$$\mathfrak{u} = (\mathfrak{I} - \mathfrak{X}_0\mathfrak{f}_{\rm hxc})^{-1}\,\mathfrak{X}_0\mathfrak{g}. \tag{1.60}$$

This requires that $\mathfrak{I}-\mathfrak{X}_0\mathfrak{f}_{\rm hxc}$ is invertible. If operator $\mathfrak{I}-\mathfrak{X}_0\mathfrak{f}_{\rm hxc}$ is not invertible, it means that it is possible that a small perturbation of the potential generates a unbounded perturbation to the density matrix and more specifically to the density. From a physical point of view, This means that the electronic structure of the system is not stable with respect to external perturbations. Therefore the invertibility of the operator $\mathfrak{I}-\mathfrak{X}_0\mathfrak{f}_{\rm hxc}$ is known as the stability condition of electronic structure in Kohn-Sham density functional theory. [59]

In practice, Eq. (1.59) can be solved iteratively as a fixed point problem. A simplest iteration scheme can be constructed recursively substitute $\mathfrak{u}$ into the right hand side. This leads to the Neumann series

$$\mathfrak{u} = \mathfrak{X}_0\mathfrak{g} + \mathfrak{X}_0\mathfrak{f}_{\rm hxc}\mathfrak{X}_0\mathfrak{g} + \mathfrak{X}_0\mathfrak{f}_{\rm hxc}\mathfrak{X}_0\mathfrak{f}_{\rm hxc}\,\mathfrak{X}_0\mathfrak{g} + \cdots \tag{1.61}$$

The iteration solution requires the application of $\mathfrak{X}_0$ to a 2 tensor, which can be obtained by using the Adler-Wiser formula in Eq. (1.55).

1.7 Lattice dynamics from KSDFT

Recall that in section 1.2, the Kohn-Sham energy functional (1.14) is introduced. The associated Euler-Lagrange equation leads to Kohn-Sham equations (1.21). In section 1.3, the self-consistent solution of the Kohn-Sham equations are obtained by the convergence of SCF iteration. The self-consistent solution gives all the information, especially the total energy of the system, given a atomic configuration $\{\mathbf{R}_I\}$ is fixed. In this section, we will visit the lattice dynamics of a system in electronic structure theory.

1.7.1 Phonon frequency

In the BO approximation, the nuclei are treated as classical particles. So the equilibrium geometry of the system is given by the condition that the forces acting on individual nuclei vanish:

$$\mathbf{F}_I(\{\mathbf{R}_I\}) = -\frac{\partial E_{\text{tot}}(\{\mathbf{R}_I\})}{\partial \mathbf{R}_I} = 0. \tag{1.62}$$

When the self-consistent ground state electron density ρ has been computed, the atomic force can be obtained using the Hellman-Feynman theorem as

$$\begin{aligned} \mathbf{F}_I(\{\mathbf{R}_I\}) &= -\frac{\partial E_{\text{tot}}(\{\mathbf{R}_I\})}{\partial \mathbf{R}_I} \\ &= -\int \frac{\partial V_{\text{ion}}}{\partial \mathbf{R}_I}(\mathbf{r}, \mathbf{r}'; \{\mathbf{R}_I\}) P(\mathbf{r}', \mathbf{r})\, \mathrm{d}\mathbf{r}\, \mathrm{d}\mathbf{r}' - \frac{\partial E_{\text{II}}(\{\mathbf{R}_I\})}{\partial \mathbf{R}_I}. \end{aligned} \tag{1.63}$$

Assume the system deviates from its equilibrium position $\{\mathbf{R}_I\}$ by some small magnitude, then the changes of the total energy is dominated by the Hessian matrix with respect to the atomic positions. This Hessian matrix is referred to as the matrix of the *inter-atomic force constants*. The dynamical matrix D consists of $d \times d$ blocks in the form

$$D_{I,J} = \frac{1}{\sqrt{M_I M_J}} \frac{\partial^2 E_{\text{tot}}(\{\mathbf{R}_I\})}{\partial \mathbf{R}_I \partial \mathbf{R}_J}, \tag{1.64}$$

where M_I is the mass of the I-th nuclei. The size of the dynamical matrix is $d \times N_A$ by $d \times N_A$. The equilibrium atomic configuration is at a local minimum of the total energy, and all the eigenvalues of D are real and non-negative. Hence the eigen-decomposition of D is

$$D u_k = \omega_k^2 u_k,$$

where u_k is called the k-th phonon mode, and ω_k is called the k-th phonon frequency. The phonon spectrum is defined as the distribution of the eigenvalues $\{\omega_k\}$ i.e.

$$\varrho_D(\omega) = \frac{1}{dN_A} \sum_k \delta(\omega - \omega_k). \tag{1.65}$$

Here δ is the Dirac-δ distribution. ϱ_D is also referred to as the density of states of D [40, 34].

Mathematically, one direct way of computing the phonon frequency, or ϱ_D, immediately follows the definition: using finite difference approximation. This approach is called the *frozen phonon* approach in computational physics, which is elaborated as follows.

To compute the phonon frequency, one use the finite difference scheme to approximate the dynamical matrix (1.64). Specifically, the a-th colomn of the I, J block is approximated by

$$D_{I,J,a} \approx \frac{1}{\sqrt{M_I M_J}} \left(\frac{\mathbf{F}_I(\{R_I; \mathbf{R}_J \leftarrow \mathbf{R}_J + h\mathbf{e}_a\}) - \mathbf{F}_I(\{\mathbf{R}_I\})}{h} \right), \tag{1.66}$$

where $\mathbf{F}_I(\{R_I; \mathbf{R}_J \leftarrow \mathbf{R}_J + h\mathbf{e}_a\})$ is the atomic force when the J-th atom is perturbed by a small magnitude h along the $\mathbf{e}_a$ axis. In the rest of this dissertation, we will refer to this approach as the finite difference (FD).

The finite difference approach provides the most intuitive way of computing the phonon frequency of a system. It only requires solving the Kohn-Sham equations self-consistently for the original system and several perturbed systems. On the other hand, this finite difference approach computes an approximation of the Hessian matrix and the dynamical matrix. The error of the method is depends heavily on the accuracy of the SCF iteration. Moreover what is usually observed in practical application is that the error of the FD approach saturates with the size of the perturbation goes to 0. This disadvantage prevents one from using FD for phonon calculation if more accurate result is desired.

1.7.2 Phonon calculation using Density Functional Perturbation Theory

As the application of the density functional perturbation theory, which is of particular interest in this dissertation, we show the phonon calculation using Density Functional Perturbation Theory discussed in Section 1.6. In comparison to the finite difference approach, it provides an analytical way of constructing the dynamical matrix and hence the phonon structure of a system.

In order to compute the Hessian matrix, we obtain from Eq. (1.62) that

$$\begin{aligned} \frac{\partial^2 E_{\text{tot}}(\{\mathbf{R}_I\})}{\partial \mathbf{R_I} \partial \mathbf{R_J}} = & \int \frac{\partial V_{\text{ion}}}{\partial \mathbf{R}_I}(\mathbf{r}, \mathbf{r}'; \{\mathbf{R}_I\}) \frac{\partial P(\mathbf{r}', \mathbf{r})}{\partial \mathbf{R}_J} \, \mathrm{d}\mathbf{r} \, \mathrm{d}\mathbf{r}' \\ & + \int \frac{\partial^2 V_{\text{ion}}}{\partial \mathbf{R}_I \partial \mathbf{R}_J}(\mathbf{r}, \mathbf{r}'; \{\mathbf{R}_I\}) P(\mathbf{r}', \mathbf{r}) \, \mathrm{d}\mathbf{r} \, \mathrm{d}\mathbf{r}' + \frac{\partial^2 E_{\text{II}}(\{\mathbf{R}_I\})}{\partial \mathbf{R}_I \partial \mathbf{R}_J}. \end{aligned} \tag{1.67}$$

Similar to the force calculation, the second term of Eq. (1.67) can be readily computed with numerical integration, and the third term involves only ion-ion interaction that is independent of the electronic states. Hence the first term is the most challenging one due to the response of the electron density with respect to the perturbation of atomic positions. Applying the chain rule, we have

$$\begin{aligned}
&\int \frac{\partial V_{\text{ion}}}{\partial \mathbf{R}_I}(\mathbf{r},\mathbf{r}';\{\mathbf{R}_I\})\frac{\partial P(\mathbf{r}',\mathbf{r})}{\partial \mathbf{R}_J}\,\mathrm{d}\mathbf{r}\,\mathrm{d}\mathbf{r}' \\
=&\int \frac{\partial V_{\text{ion}}(\mathbf{r},\mathbf{r}';\{\mathbf{R}_I\})}{\partial \mathbf{R}_I}\frac{\delta P(\mathbf{r}',\mathbf{r})}{\delta V_{\text{ion}}(\mathbf{r}'',\mathbf{r}''')}\frac{\partial V_{\text{ion}}(\mathbf{r}'',\mathbf{r}''');\{\mathbf{R}_I\})}{\partial \mathbf{R}_J}\,\mathrm{d}\mathbf{r}\,\mathrm{d}\mathbf{r}'\,\mathrm{d}\mathbf{r}''\,\mathrm{d}\mathbf{r}''' \\
=&\int \frac{\partial V_{\text{ion}}(\mathbf{r},\mathbf{r}';\{\mathbf{R}_I\})}{\partial \mathbf{R}_I}\mathfrak{X}(\mathbf{r},\mathbf{r}';\mathbf{r}'',\mathbf{r}''')\frac{\partial V_{\text{ion}}(\mathbf{r}'',\mathbf{r}''');\{\mathbf{R}_I\})}{\partial \mathbf{R}_J}\,\mathrm{d}\mathbf{r}\,\mathrm{d}\mathbf{r}'\,\mathrm{d}\mathbf{r}''\,\mathrm{d}\mathbf{r}'''
\end{aligned} \tag{1.68}$$

Here the Fréchet derivative $\mathfrak{X}(\mathbf{r},\mathbf{r}';\mathbf{r}'',\mathbf{r}''') = \dfrac{\delta P(\mathbf{r},\mathbf{r}')}{\delta V_{\text{ion}}(\mathbf{r}'',\mathbf{r}''')}$ is referred to as the reducible polarizability operator. The calculation of applying $\mathfrak{X}$ to $\mathfrak{g} = \frac{\partial V_{\text{ion}}(\mathbf{r}'',\mathbf{r}''');\{\mathbf{R}_I\})}{\partial \mathbf{R}_J}$ should be obtained from solving the Dyson equation in Eq.(1.58).

Using the linear algebra type of notation, the key difficulty of phonon calculations is the computation of the tensor contraction $\mathfrak{u} = \mathfrak{X}\mathfrak{g}$, where $\mathfrak{g}$ traverses $d \times N_A$ order 2 tensors of the form $\frac{\partial V_{\text{ion}}(\mathbf{r}'',\mathbf{r}''';\{\mathbf{R}_I\})}{\partial \mathbf{R}_{J,a}}$, where $\mathbf{R}_{J,a}$ is the a-th direction of the atomic position $\mathbf{R}_J$ $(a = 1,\ldots,d)$. According to Eq. (1.18), $\mathfrak{g}$ can split into a local component and a nonlocal component as

$$\mathfrak{g}(\mathbf{r},\mathbf{r}') = g_{\text{loc}}(\mathbf{r})\delta(\mathbf{r}-\mathbf{r}') + \mathfrak{g}_{\text{nl}}(\mathbf{r},\mathbf{r}'), \tag{1.69}$$

or equivalently $\mathfrak{g} = \text{diag}[g_{\text{loc}}] + \mathfrak{g}_{\text{nl}}$. For each $\mathfrak{g}$, only one atom J contributes to the order 1 tensor g_{loc} and the order 2 tensor $\mathfrak{g}_{\text{nl}}$. From the definition of nonlocal pseodopotential Eq. (1.19), we have

$$\begin{aligned}
&\mathfrak{g}_{\text{nl},I}(\mathbf{r},\mathbf{r}') = \sum_{l=1}^{L_I}\gamma_{I,l}\left[b_{I,l}(\mathbf{r}-\mathbf{R}_I)db^*_{I,l}(\mathbf{r}'-\mathbf{R}_I) + db_{I,l}(\mathbf{r}-\mathbf{R}_I)b^*_{I,l}(\mathbf{r}'-\mathbf{R}_I)\right], \\
&\text{where}\quad db_{I,l}(\mathbf{r}-\mathbf{R}_I) := \frac{\partial b_{I,l}(\mathbf{r}-\mathbf{R}_I)}{\partial \mathbf{R}_I}.
\end{aligned} \tag{1.70}$$

We note that $\mathfrak{g}_{\text{nl}}$ is a symmetric operator of rank $2L_I$, where the factor 2 comes from the Leibniz formula. In the rest of the dissertation, we shall use $b_l(\mathbf{r}), db_l(\mathbf{r})$ to hide the explicit dependence on the atom indices I or the atomic positions $\{\mathbf{R}_I\}$.

In order to solve the Dyson equation (1.58), we need to apply $\mathfrak{X}_0$ to order 2 tensors of the form $\mathfrak{g}$ or $\mathfrak{f}_{\text{hxc}}\mathfrak{u}$. By means of the eigenfunctions ψ_i, the eigenvalues ε_i, and the occupation numbers f_i, $\mathfrak{X}_0\mathfrak{g}$ can be expressed using the Adler-Wiser formula [1, 60]

$$(\mathfrak{X}_0\mathfrak{g})(\mathbf{r},\mathbf{r}') = \sum_{i,a=1}^{\infty}\frac{f_a - f_i}{\varepsilon_a - \varepsilon_i}\psi_a(\mathbf{r})\left(\int \psi^*_a(\mathbf{r}'')\mathfrak{g}(\mathbf{r}'',\mathbf{r}''')\psi_i(\mathbf{r}''')\,\mathrm{d}\mathbf{r}''\,\mathrm{d}\mathbf{r}'''\right)\psi^*_i(\mathbf{r}'), \tag{1.71}$$

where the term when $i = a$ should be interpreted as the limit when $\varepsilon_a \to \varepsilon_i$. Recall that in Eq. 1.55 we have the formula using the linear algebra notation of Eq. (1.71), which can be written as

$$\mathfrak{X}_0\mathfrak{g} = \sum_{i,a=1}^{\infty} \frac{f_a - f_i}{\varepsilon_a - \varepsilon_i} \psi_a(\psi_a^* \mathfrak{g} \psi_i)\psi_i^*. \tag{1.72}$$

Since $\mathfrak{g}$ is an Hermitian order 2 tensor, $\mathfrak{X}_0\mathfrak{g}$ is also an Hermitian order 2 tensor. If we truncate the infinite sum in Eq. (1.72) to a finite sum of states, Eq. (1.72) and Eq. (1.58) can be solved together to obtain $\mathfrak{u}$, and therefore the Hessian matrix (1.67) can be evaluated.

In order to observe the computational complexity of DFPT for phonon calculations, let us first neglect the nonlocal pseudopotential $V_{\mathrm{nl},I}$. This leads to much simplification of the notation. Since each $\mathfrak{g}$ only involves the local contribution, Eq. (1.67) only requires $\dfrac{\partial \rho(\mathbf{r})}{\partial \mathbf{R}_J}$. Therefore one is only interested in computing

$$u(\mathbf{r}) = \mathfrak{u}(\mathbf{r}, \mathbf{r}) = \int \mathfrak{X}(\mathbf{r}, \mathbf{r}; \mathbf{r}', \mathbf{r}')\mathfrak{g}(\mathbf{r}', \mathbf{r}')\, \mathrm{d}\mathbf{r}' := \int \chi(\mathbf{r}, \mathbf{r}')g_{\mathrm{loc}}(\mathbf{r}')\, \mathrm{d}\mathbf{r}'. \tag{1.73}$$

Here we have introduced $\chi(\mathbf{r}, \mathbf{r}') = \mathfrak{X}(\mathbf{r}, \mathbf{r}; \mathbf{r}', \mathbf{r}')$, and used that the nonlocal component of $\mathfrak{g}$ vanishes. Similarly we can define $\chi_0(\mathbf{r}, \mathbf{r}') = \mathfrak{X}_0(\mathbf{r}, \mathbf{r}; \mathbf{r}', \mathbf{r}')$. We also consider insulating systems with a finite band gap. This allows us to simplify the temperature dependence of the occupation number so that $f_i = 1$ if $i \leq N_e$ and 0 if $i \geq N_e + 1$. As a result, Eq. (1.72) can be simplified as

$$\chi_0 g_{\mathrm{loc}} = \sum_{i=1}^{N_e} \sum_{a=N_e+1}^{\infty} \frac{1}{\varepsilon_i - \varepsilon_a} \mathrm{diag}[\psi_i^*]\psi_a \left(\psi_a^* \mathrm{diag}[g_{\mathrm{loc}}]\psi_i\right) + \mathrm{h.c.} \tag{1.74}$$

Here h.c. means the Hermitian conjugate of the first term.

In order to overcome the difficulty of explicit computation of all the unoccupied orbitals $\{\psi_a\}_{a=N_e+1}^{\infty}$, we first define the projection operator to the unoccupied space $Q = I - \sum_{i=1}^{N_e} \psi_i \psi_i^*$. Then we can compute $\chi_0 g_{\mathrm{loc}}$ as

$$\chi_0 g_{\mathrm{loc}} = \sum_{i=1}^{N_e} \mathrm{diag}[\psi_i^*] Q (\varepsilon_i - H)^{-1} Q (\mathrm{diag}[g_{\mathrm{loc}}]\psi_i) + \mathrm{h.c.}. \tag{1.75}$$

In principle, the right hand side of Eq. (1.76) only requires one Q operator to be present. However, we choose the form $Q(\varepsilon_i - H)^{-1}Q$ to emphasize that this operator is Hermitian. Let $\zeta_i := Q(\varepsilon_i - H)^{-1}Q(\mathrm{diag}[g_{\mathrm{loc}}]\psi_i)$, the matrix inverse in Eq. (1.75) can be avoided by solving the *Sternheimer equations*

$$Q(\varepsilon_i - H)Q\zeta_i = Q(\mathrm{diag}[g_{\mathrm{loc}}]\psi_i). \tag{1.76}$$

This strategy has been used in a number of contexts involving the polarizability operator [21, 46, 56, 18, 44]. The Sternheimer equations can be solved using standard direct or iterative linear solvers. The choice of the solver can depend on practical matters such as the discretization scheme, and the availability of preconditioners. In practice for planewave discretization, we find that the use of the minimal residual method (MINRES) [47] gives the best numerical performance.

The complexity of phonon calculations using density functional perturbation theory can now be analyzed as below. Even with local pseudopotential only, and assume the Dyson equations always converge within a constant number of iterations that is independent of the system size N_e, we need to apply χ_0 to $d \times N_A \sim \mathcal{O}(N_e)$ vectors of the form g_{loc}. Each g_{loc} requires solving N_e Sternheimer equations (1.76), and the computational cost of applying the projection operator Q to a vector is $\mathcal{O}(N_e^2)$. Hence the overall complexity is $\mathcal{O}(N_e^4)$ [5]. This is significantly more expensive than solving the KSDFT, of which the computational complexity is typically $\mathcal{O}(N_e^3)$.

1.7.3 Existing software packages for phonon calculations

Below are some representative software packages for phonon structure calculation using quartic scaling methods:

- Quantum ESPRESSO - PHonon: Density Functional Perturbation Theory.
  `https://www.quantum-espresso.org/`
- ABINIT: Density Functional Perturbation Theory.
  `http://www.abinit.org/,https://docs.abinit.org/topics/Phonons/`
- Phonopy: Finite difference method. Force computation could be done using most popular packages.
  `https://atztogo.github.io/phonopy/`
- VASP (Vienna Ab-initio Simulation Package) : Finite difference method.
  `https://www.vasp.at/`
- CRYSTAL: Finite difference method.
  `http://www.crystal.unito.it/`
- SIESTA (Spanish Initiative for Electronic Simulations with Thousands of Atoms) : Finite difference method.
  `https://departments.icmab.es/leem/siesta/`
- LAMMPS (Large-scale Atomic/Molecular Massively Parallel Simulator): Finite difference method.
  `https://lammps.sandia.gov/`

1.8 Summary of chapter 1

In Chapter 1, we started with the formulation of Kohn-Sham Density Functional Theory in section 1.2. It is by far the most widely used electronic structure theory that best compromises between accuracy and efficiency. We have reviewed the quantum many body problem and Born-Oppenheimer approximation which reduces the quantum many body problem to the electronic structure problem. Hohenberg and Kohn then stated that no two different potentials acting on the electrons of a given system can give rise to a same ground-state electronic charge density, which replaces the traditional description based on wavefunctions with a much more tractable one in terms of the charge density ρ. With this huge simplification, the setup of Kohn-Sham density functional theory in zero temperature is reviewed, followed by the generalization for systems in finite temperature. After that in section 1.3, the self-consistent field iteration is elaborated so that the Kohn-Sham equations can be solved self-consistently. In section 1.4, we visited a central object in electronic structure theory, which not only provides one with a more intrinsic way of constructing Kohn-Sham equations, but also helps with the implementation of many numerical algorithms. With the help of density matrix, we visited the linear response theory in section 1.5, where Adler-Wiser formula is introduced. In section 1.6, we apply the result of linear response theory to the case of Kohn-Sham density functional theory and introduced the Dyson equations which relates the reducible polarizability operator $\mathfrak{X}$ with the irreducible polarizability operator $\mathfrak{X}_0$. The Dyson equation characterizes the self-consistent response of the density matrix with respect to the external perturbation. Finally in section 1.7, we focus on the application of phonon calculation, where the finite difference method (FD) and the approach of using density functional perturbation theory (DFPT) is elaborated.

The computational cost for phonon calculation using FD and DFPT are both $\mathcal{O}(N_e^4)$. In chapter 2, a new method is developed to reduce the computational cost to $\mathcal{O}(N_e^3)$ for the first time. In chapter 3, the generalization of the new method is further discussed.

Chapter 2

Adaptively Compressed Polarizability Operator

2.1 Introduction

In principle, KSDFT provides an exact description of ground state properties of a many body quantum system, such as electron density, energy, and atomic forces. Once the electronic ground state is obtained, many physical and chemical properties of the system can be described by studying the *response* of the quantum system under small perturbation. The theory for describing such response behavior is called the density functional perturbation theory (DFPT) [3, 21, 5].

One important application of DFPT is the description of lattice vibrations. In the Born-Oppenheimer approximation, lattice vibrations can be described by the dynamical matrix, which is related to the Hessian matrix of the ground state energy with respect to the atomic positions. The eigenfunctions of the dynamical matrix give the phonon modes, and the eigenvalues give the phonon frequencies. A large variety of physical properties of solids depend on such phonon calculations. A few examples include infrared spectroscopy, elastic neutron scattering, specific heat, heat conduction, and electron-phonon interaction related behaviors such as superconductivity [21, 5]. Furthermore, the computational procedure of phonon calculations are largely transferable to the calculation of other types of response behavior, such as response to homogeneous electric fields, piezoelectric properties, magnons, and many body perturbation theory for the description of electrons at excited states such as the GW theory [25, 46].

The term "phonon calculation" usually describes the calculation of vibrational properties of condensed matter systems. In this dissertation, we slightly abuse this term to refer to calculations of vibration properties of general systems, including condensed matter systems as well as isolated molecule clusters, since such calculations share the same mathematical structure. Mathematically, the procedure for phonon calculations can be straightforward. When atoms are at their equilibrium positions, the atomic forces (i.e. first order derivatives

of the energy with respect to the atomic position) are zero for all atoms. To compute the Hessian matrix, one can move one atom at a time slightly away from its equilibrium position, and compute the corresponding atomic forces. This amounts to the finite difference (FD) approximation of the Hessian matrix, and is referred to as the "frozen phonon" [63, 4] approach in physics. The FD approach is simple to implement and can be used to obtain phonon spectrum quickly for systems of small sizes. However, FD requires in total $d \times N_A \sim \mathcal{O}(N_e)$ KSDFT calculations, where d is the spatial dimension (usually $d = 3$), and N_A is the number of atoms. The computational complexity of a single KSDFT calculation typically scales as $\mathcal{O}(N_e^3)$, where N_e is the number of electrons in the system. Since $N_A \sim \mathcal{O}(N_e)$, the total cost of the FD approximation is $\mathcal{O}(N_e^4)$. This is prohibitively expensive for systems of large sizes. Furthermore, the accuracy of the FD approximation is limited by the size of the perturbation, which cannot be too small due to the numerical noise in the evaluation of the atomic forces in KSDFT calculations (usually the accuracy of forces is set to be $10^{-4} \sim 10^{-3}$ Hartree/Bohr). Such numerical noise also makes it difficult to compute non-linear response properties, which can require even higher order derivatives of the energy.

DFPT, on the other hand, can be viewed as the "proper" way for computing derivative quantities in the context of KSDFT. The central quantity in DFPT is the polarizability operator, which characterizes the linear response of the electron density with respect to the perturbation of the external potential. More specifically, phonon calculations requires applying the polarizability operator to $d \times N_A$ perturbation vectors induced by the change of the atomic configuration. The polarizability operator can be obtained by solving a Dyson equation iteratively [5], and each iteration step requires the solutions to $\mathcal{O}(N_e^2)$ Sternheimer equations. In general the complexity of DFPT is still $\mathcal{O}(N_e^4)$. So the main advantage of DFPT is that it gives accurate linear response properties. Furthermore, the same framework can be used to compute non-linear response properties [22, 20, 5]. The mathematical aspect of DFPT for reduced Hartree-Fock model systems have recently been analyzed [11]. It is also possible to reduce the computational complexity of phonon calculations by "linear scaling methods" [19, 8]. Such methods can be successful in reducing the computational cost for systems of large sizes with substantial band gaps, but this can be challenging for medium-sized systems with relatively small band gaps.

The main computational bottleneck of DFPT is the solution of the $\mathcal{O}(N_e^2)$ Sternheimer equations [5]. KSDFT can be defined as a nonlinear eigenvalue problem with $\mathcal{O}(N_e)$ eigenfunctions. Each of the $\mathcal{O}(N_e^2)$ equations in DFPT represents the response of an eigenfunction to a different external perturbation. Hence at first sight it is not possible to reduce the number of equations. However, as N_e becomes large, there will be asymptotically more equations to solve than the size of the matrix. Hence there is potential room to obtain a set of "compressed perturbations", which leads to methods for solving DFPT with lower complexity.

At this point it might be enticing to compress the $\mathcal{O}(N_e^2)$ equations using standard compression schemes such as singular value decomposition (SVD). However, there is some immediate difficulty associated with SVD type of compression scheme: The matrix to be compressed is of size $\mathcal{O}(N_e^2) \times \mathcal{O}(N_e)$ and of approximate rank $\mathcal{O}(N_e)$. The associated cost of the SVD type of compression is $\mathcal{O}(N_e^4)$, and hence there is no saving in asymptotic

complexity. Furthermore, the $\mathcal{O}(N_e^2)$ equations need to be solved self-consistently according to the Dyson equation. Hence the initially compressed vectors might not be applicable anymore as the iteration proceeds towards the converged solution. This leads to inaccurate phonon calculations.

In this chapter, we develop a new method called the adaptively compressed polarizability operator (ACP) to overcome the above difficulties. ACP reduces the complexity for applying the polarizability operator to $\mathcal{O}(N_e)$ vectors as follows. 1) ACP compresses the $\mathcal{O}(N_e^2)$ right hand side vectors of the Sternheimer equations into $\mathcal{O}(N_e)$ vectors, using a recently developed interpolative separable density fitting method [38]. Together with a Chebyshev interpolation procedure to disentangle the energy dependence from the right hand side vectors, ACP reduces the number of equations from $\mathcal{O}(N_e^2)$ to only $\mathcal{O}(N_e)$. 2) ACP reformulates the Dyson equation into an equivalent fixed point problem, where the compression of the Sternheimer equations depends adaptively on the unknown solutions. Using such adaptive compression procedure, we demonstrate that the self-consistent solution to the Dyson equation no longer hinders the accuracy of the compressed polarizability operator. Such adaptive compression strategy shares similar spirit to the recently developed adaptively compressed exchange operator (ACE) for accelerating KSDFT calculations with hybrid exchange-correlation functionals [33]. We demonstrate that the overall computational complexity for phonon calculations can be reduced to $\mathcal{O}(N_e^3)$, and the cost depends only weakly on the band gap of the system. Hence the method can be applied to both insulators and semiconductors with small gaps. To the extent of our knowledge, this is the first result of this type in literature. We demonstrate the numerical performance of the ACP formulation for accelerating phonon calculations using model systems for one-dimensional and two-dimensional systems, both for periodic lattices and for systems with defects and random perturbations. Our numerical results confirm the low complexity of the ACP formulation for computing the full dynamical matrix and hence the phonon spectrum.

The rest of the chapter is organized as follows. Section 2.2 reviews the interpolative separable density fitting method. Section 2.3 describes the ACP formulation. Numerical results are presented in section 2.4, followed by conclusion and discussion in section 2.5.

2.2 Interpolative separable density fitting

In this section, we setup the interpolative separable density fitting (ISDF) method in the context of solving Sternheimer equations. The method is first developed in by Lu and Ying in ref [38].

Given the Kohn-Sham orbitals $\{\psi_i(\mathbf{r})\}$, and the local perturbations $\{g_j(\mathbf{r})\}$, let us denote by M the collection of the right hand side of all Sternheimer equations

$$M_{ij} = \psi_i \odot g_j, \quad \text{or} \quad M_{ij}(\mathbf{r}) = \psi_i(\mathbf{r}) g_j(\mathbf{r}). \tag{2.1}$$

Here we have used ij as a stacked column index for the matrix M. The dimension of M is $N_g \times \mathcal{O}(N_e^2)$. Typically, the computational complexity for the compression for such a

dense matrix M with approximate rank $\mathcal{O}(N_e)$ is $\mathcal{O}(N_e^4)$, even with the help of the recently developed randomized algorithms (see [24] for a review). Nonetheless, note that for a fixed row index $\mathbf{r}_\alpha$, the row vector given by $\{M_{ij}(\mathbf{r}_\alpha)\}_{i,j=1}^{i=N_e,j=d\times N_A}$ is the Kronecker product between the row vector given by $\{g_j(\mathbf{r}_\alpha)\}_{j=1}^{d\times N_A}$ and that given by $\{\psi_i(\mathbf{r}_\alpha)\}_{i=1}^{N_e}$. As will be seen below, this structure allows the computational complexity of the compression of M to be reduced to $\mathcal{O}(N_e^3)$.

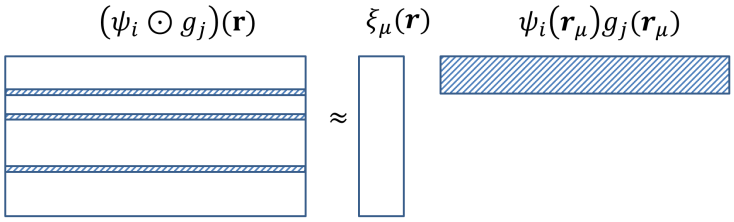

Figure 2.1: Interpolative decomposition of $M_{ij}(\mathbf{r})$.

To this end, we seek for the following interpolative decomposition (ID) type of compression [14] for the matrix M, i.e.

$$M_{ij}(\mathbf{r}) \approx \sum_{\mu=1}^{N_\mu} \xi_\mu(\mathbf{r}) M_{ij}(\mathbf{r}_\mu) \equiv \sum_{\mu=1}^{N_\mu} \xi_\mu(\mathbf{r})\psi_i(\mathbf{r}_\mu)g_j(\mathbf{r}_\mu). \tag{2.2}$$

Here $\{\mathbf{r}_\mu\}_{\mu=1}^{N_\mu}$ denotes a collection of selected row indices (see Fig. 2.1 for an illustration). Mathematically, the meaning of the indices $\{\mathbf{r}_\mu\}$ is clear: Eq. (2.2) simply states that all rows $M_{:}(\mathbf{r})$ can be approximately expressed as the linear combination of the selected rows $\{M_{:}(\mathbf{r}_\mu)\}$. However, we are not aware of any direct physical interpretation of such selected indices. Since $N_g \sim N_e$, as N_e increases, the column dimension of M (which is $\mathcal{O}(N_e^2)$) can be larger than its row dimension (which is N_g), and we can expect that the vectors $\{\psi_i \odot g_j\}$ are approximately linearly dependent. Such observation has been observed in the electronic structure community [58, 52, 17, 57, 51], and the numerical rank of the matrix M after truncation can be only $\mathcal{O}(N_e)$ with a relatively small pre-constant. In the context of the interpolative decomposition, our numerical results also indicate that it is sufficient to choose $N_\mu \sim \mathcal{O}(N_e)$, and the pre-constant is small.

One possible way of finding interpolative decomposition is to use a pivoted QR factorization [13, 23]. However, the cost of the pivoted QR factorization applied to the matrix M is $\mathcal{O}(N_g N_e^2 N_\mu) \sim \mathcal{O}(N_e^4)$, and is therefore not desirable. The interpolative separable density fitting method [38] employs a two-step procedure to reduce this cost (see Fig. 2.2 for an illustration). The first step is to use a fast pre-processing procedure, such as a subsampled random Fourier transform (SRFT) [61], to transform the matrix M into a matrix $\widetilde{M}$ of smaller dimension $N_g \times rN_e$, with r a relatively small constant so that rN_e is slightly larger

than N_μ. The second step is to apply the pivoted QR decomposition to $\widetilde{M}$

$$\widetilde{M}^T\widetilde{\Pi} = \widetilde{Q}\widetilde{R}, \tag{2.3}$$

where $\widetilde{\Pi}$ is a permutation matrix and encodes the choice of the row indices $\{\mathbf{r}_\mu\}$ from $\widetilde{M}$. The interpolation vectors $\{\xi_\mu\}$ in Eq. (2.2) can be also be computed from this pivoted QR decomposition. It should be noted that the pre-processing procedure does not affect the quality of the interpolative decomposition, while the cost of the pivoted QR factorization in Eq. (2.3) is now reduced to $\mathcal{O}(N_g N_\mu^2) \sim \mathcal{O}(N_e^3)$. We summarize the procedure for compressing M in Alg. 1.

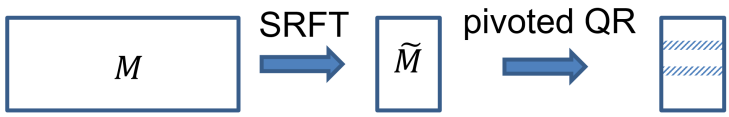

Figure 2.2: The two-step procedure of the interpolative separable density fitting method.

We remark that in Alg. 1, step 1.(a), it is possible to avoid the explicit construction of the matrix M. Instead of performing SRFT on the entire matrix M, we could apply SRFT only to the matrix G, and select r columns as a matrix $\widetilde{G}$. Then for a fixed row index $\mathbf{r}_\alpha$, the Kronecker product between the rows of subsampled matrix $\widetilde{G}$, $\{\widetilde{g}_i(\mathbf{r}_\alpha)\}_{i=1}^r$, and $\{\psi_i(\mathbf{r}_\alpha)\}_{i=1}^{N_e}$ gives one row for $\widetilde{M}$. In practice we find that this heuristic procedure also works well for compressing the matrix M in phonon calculations.

2.3 Adaptively compressed polarizability operator

In this section, we develop a new method for reducing the computational complexity of DFPT from $\mathcal{O}(N_e^4)$ to $\mathcal{O}(N_e^3)$. The reduction of the computational complexity is achieved by means of reducing the $\mathcal{O}(N_e^2)$ equations in DFPT to $\mathcal{O}(N_e)$ equations with systematic control of the accuracy. In particular, our method does not employ the "nearsightedness" property of electrons for insulating systems with substantial band gaps as in linear scaling methods [30]. Hence our method can be applied to insulators as well as semiconductors with small band gaps. In section 1.7.2, we have reduced the problem of computing the dynamic matrix to the computation of $\chi g_{I,a}$, where $\{g_{I,a}\}$ is a set of fixed vectors given by the derivative of the local pseudopotential with respect to the atomic positions. Let us stack the indicies I, a into a single index j, and denote by

$$G := [g_1, \ldots, g_j, \ldots, g_{d\times N_A}] \tag{2.4}$$

the matrix collecting all these vectors. More generally, G can be any fixed matrix with $\mathcal{O}(N_e)$ columns as required in different applications of DFPT. Then our method consists of two main

Algorithm 1: Interpolative decomposition for M using an interpolative separable density fitting method [38].

Input: Matrix M. Threshold tolerance ϵ.
Output: Selected row indices $\{\mathbf{r}_\mu\}$, and interpolation vectors $\{\xi_\mu\}$.

1. Subsampled random Fourier transform of M:

   a) Compute for $\nu = 1, \ldots, N_e \times d \times N_A$ the discrete Fourier transform

   $$\hat{M}_\nu(\mathbf{r}) = \sum_{I=1}^{N_e \times d \times N_A} e^{-2\pi\imath I\nu/(N_e \times d \times N_A)} \eta_I M_I(\mathbf{r}),$$

   where η_I is a random complex number with unit modulus for each I.

   b) Choose a submatrix $\widetilde{M}$ of matrix $\hat{M}$ by randomly choosing rN_e columns. In practice, $r = 8$ and $r = 16$ are used in our implementation for one-dimensional and two-dimensional numerical examples, respectively.

2. Compute the pivoted QR decomposition of the $rN_e \times N_g$ matrix $\widetilde{M}^T$: $\widetilde{M}^T\widetilde{\Pi} = \widetilde{Q}\widetilde{R}$, where the absolute values of the diagonal entries of $\widetilde{R}$ are ordered non-increasingly.

3. Determine the number of selected columns N_μ, such that $|\widetilde{R}_{N_\mu+1,N_\mu+1}| < \epsilon|\widetilde{R}_{1,1}| \leq |\widetilde{R}_{N_\mu,N_\mu}|$. Form $\{\mathbf{r}_\mu\}$, $\mu = 1, \ldots, N_\mu$ such that the $\mathbf{r}_\mu$-column of $\widetilde{M}^T$ corresponds to the μ-th column of $\widetilde{M}^T\widetilde{\Pi}$.

4. Denote by $\widetilde{R}_{1:N_\mu,1:N_\mu}$ the submatrix of $\widetilde{R}$ consisting of its first $N_\mu \times N_\mu$ entries, and $\widetilde{R}_{1:N_\mu,:}$ the submatrix consisting of the first N_μ rows of $\widetilde{R}$. Compute

   $$\Xi^T = \widetilde{R}^{-1}_{1:N_\mu,1:N_\mu}\widetilde{R}_{1:N_\mu,:}\widetilde{\Pi}^{-1}.$$

   Then the μ-th column of the $N_g \times N_\mu$ matrix Ξ gives the interpolation vector ξ_μ.

steps: 1) Find a compressed representation of χ_0, which allows the computation of $\chi_0 G$ by solving only $\mathcal{O}(N_e)$ linear equations. 2) Update the compressed representation of χ_0, which allows the accurate computation of χG without significant increase of the computational cost. In particular, step 2) requires the compression strategy of χ_0 to be *adaptive* to the solution of the Dyson equation

$$U := \chi G = \chi_0 g + \chi_0 f_{\text{hxc}} U. \tag{2.5}$$

Hence we refer our representation of χ_0 as the adaptively compressed polarizability operator (ACP). Note that Eq. (2.5) is the a special case of Eq. (2.5). The steps 1) and 2) of the ACP formulation are given in section 2.3.1 and 2.3.2, respectively.

2.3.1 Compression of χ_0

Consider first the computation of $\chi_0 G$ as required in the initial step in Eq. (2.5). In general, the singular values of χ_0 decay slowly, and a forcefully applied low rank decomposition of χ_0 such as those based on the singular value decomposition (SVD) will lead to inaccurate results. Nonetheless, it is possible to find a compressed representation of χ_0 when we only need to evaluate $\chi_0 G$ for a fixed matrix G.

As is shown in section 1.7.2, computing $\chi_0 G$ involves solving the following $\mathcal{O}(N_e^2)$ Sternheimer equations

$$Q(\varepsilon_i - H)Q\zeta_{ij} = Q(\psi_i \odot g_j), \quad i = 1, \ldots, N_e, \quad j = 1, \ldots, d \times N_A. \tag{2.6}$$

As N_e becomes large, asymptotically there can be many more equations to solve than the dimension of the matrix $N_g \sim \mathcal{O}(N_e)$, and hence it should be possible to compress the redundant information in the right hand side vectors. In fact this observation has been used in various contexts in computational chemistry for compressing the Hadamard product of occupied and unoccupied orbitals, which is called "density fitting" (DF) or "resolution of identity" (RI) techniques to compress $\mathcal{O}(N_e^2)$ vectors into $\mathcal{O}(N_e)$ vectors with a relatively small pre-constant [58, 51]. The detailed setup is already discussed in section 2.2.

It should be noted that ISDF techniques alone do not reduce the number of equations to solve. The reason is that the Eqs. (2.6) have the dependence on the shift ε_i on the left hand side. Hence even if the number of right hand side vectors is reduced to $\mathcal{O}(N_e)$, multiplied with the N_e shifts, we still have $\mathcal{O}(N_e^2)$ equations to solve! Therefore, in order to reduce the complexity for computing $\chi_0 G$, we must disentangle the right hand side vectors and the shifts. Note that all $\{\varepsilon_i\}$ are eigenvalues corresponding to occupied orbitals, and are typically contained in a relatively small interval (in the order of eV), at least in the pseudopotential framework.

More specifically, consider the following parameterized equation

$$Q(\varepsilon - H)Q\zeta = \xi, \tag{2.7}$$

where ξ is any vector in the range of Q. Since $\varepsilon \in \mathcal{I} \equiv [\varepsilon_1, \varepsilon_{N_e}]$, we can systematically obtain the solution to the parameterized equation by evaluating on a few sampled points in $\mathcal{I}$. In this work, we choose the Chebyshev nodes $\{\widetilde{\varepsilon}_c\}_{c=1}^{N_c}$, which are obtained by a linear map the Chebyshev nodes in the reference interval $[-1, 1]$ to $\mathcal{I}$, i.e.

$$\widetilde{\varepsilon}_c = \frac{\varepsilon_1 + \varepsilon_{N_e}}{2} + \frac{\varepsilon_1 - \varepsilon_{N_e}}{2} \cos\theta_c, \quad \theta_c = \frac{\pi(c - \frac{1}{2})}{N_c}, \quad c = 1, \ldots, N_c.$$

Typically it is sufficient to choose the number of Chebyshev nodes N_c to be $10 \sim 40$. Denote by $\widetilde{\zeta}_c$ the solution to Eq. (2.7) corresponding to $\varepsilon = \widetilde{\varepsilon}_c, \quad c = 1, \ldots, N_c$, then any solution ζ with $\varepsilon \in \mathcal{I}$ can be obtained by a Lagrange interpolation procedure as

$$\zeta = \sum_{c=1}^{N_c} \widetilde{\zeta}_c \prod_{c' \neq c} \frac{\varepsilon - \widetilde{\varepsilon}_{c'}}{\widetilde{\varepsilon}_c - \widetilde{\varepsilon}_{c'}}. \tag{2.8}$$

Asymptotically, the number of Chebyshev points needed to reach a given error tolerance is $\mathcal{O}(\sqrt{\varepsilon_g/|\mathcal{I}|})$, where $|\mathcal{I}|$ is the width of the interval $\mathcal{I}$. To understand this, let us consider the error of the Chebyshev interpolation for the following scalar function

$$f(z) = \frac{|\mathcal{I}|}{(z-1)\frac{|\mathcal{I}|}{2} - \varepsilon_g}, z \in [-1, 1]. \tag{2.9}$$

Note that

$$f(-1) = \frac{|\mathcal{I}|}{-|\mathcal{I}| - \varepsilon_g} = \frac{|\mathcal{I}|}{\varepsilon_1 - \varepsilon_{N_e+1}}, \quad f(1) = \frac{|\mathcal{I}|}{-\varepsilon_g} = \frac{|\mathcal{I}|}{\varepsilon_{N_e} - \varepsilon_{N_e+1}}.$$

Therefore $f(z)$ reflects the worst case behavior of the operator $Q(\varepsilon - H)^{-1}Q$. It is known that (see e.g. [55]) the L^∞ error of Chebyshev interpolation with N_c points on the interval $[-1, 1]$, denoted by E_{N_c}, should satisfy

$$E_{N_c} \leq \frac{2M}{(\alpha - 1)\alpha^{N_c}}.$$

Here the function $f(z)$ is analytic in the region bounded by the ellipse with foci ± 1 and major and minor semiaxis lengths summing to $\alpha > 1$, and $|f(z)| < M$ is bounded in this region. For the specific function $f(z)$ in Eq. (2.9) with the presence of the band gap ε_g, the major semiaxis could be chosen to be $1+\varepsilon_g/|\mathcal{I}|$, which means that $\alpha \approx 1+\sqrt{2\varepsilon_g/|\mathcal{I}|}+\varepsilon_g/|\mathcal{I}| \approx 1+\sqrt{2\varepsilon_g/|\mathcal{I}|}$. Within this ellipse, we obtain the bound $M = 2|\mathcal{I}|/\varepsilon_g$. This gives the error bound of Chebyshev interpolation as

$$E_{N_c} \leq C \left(\frac{\mathcal{I}}{\varepsilon_g}\right)^{3/2} e^{-N_c\sqrt{2\varepsilon_g/|\mathcal{I}|}}. \tag{2.10}$$

When $\varepsilon_g/|\mathcal{I}|$ is sufficiently small, C is a constant that is independent of $\varepsilon_g/|\mathcal{I}|$. Therefore N_c should scale as $\sqrt{|\mathcal{I}|/\varepsilon_g}\log(|\mathcal{I}|/\varepsilon_g)$. Our numerical results in section 2.4 indicates that $N_c = 10 \sim 30$ often yields sufficiently accurate results. We also remark that if $\varepsilon_g/|\mathcal{I}|$ is very small, one can further reduce the number of interpolation points using contour integral techniques [15], where $N_c = \mathcal{O}(\log(|\mathcal{I}|/\varepsilon_g))$ is sufficient. However, we observe that the preconstant of such technique tend to be larger than that of the Chebyshev interpolation. Hence we choose to present the method using Chebyshev interpolation in this chapter.

Using Chebyshev interpolation (2.8), we need to solve Eq. (2.6) with ε_i replaced by $\widetilde{\varepsilon}_c$. At first sight, the number of equations does not decrease but actually increase by a factor of N_c compared to the original formulation (2.6). However, Chebyshev interpolation disentangles the index i that appears both in the shift and in the right hand side. Since N_c is a constant that is independent of the system size, if we can find a compressed representation of the right hand side vectors using $\mathcal{O}(N_e)$ vectors, we reduce the overall number of equations to solve to $\mathcal{O}(N_e)$.

Once the compressed representation (2.2) is obtained, we solve the following set of modified Sternheimer equations

$$Q(\widetilde{\varepsilon}_c - H)Q\widetilde{\zeta}_{c\mu} = Q\xi_\mu, \quad c = 1, \ldots, N_c, \quad \mu = 1, \ldots, N_\mu. \tag{2.11}$$

Here $c\mu$ is the stacked column index for $\widetilde{\zeta}$. The number of equations is hence reduced to $N_c N_\mu \sim \mathcal{O}(N_e)$. Using Eq. (2.8), we construct the quantity $W = \left[W_1, \ldots, W_{N_\mu}\right]$. Each column of W is defined by

$$W_\mu = 2\sum_{i=1}^{N_e} \psi_i \odot \left(\sum_{c=1}^{N_c} \widetilde{\zeta}_{c\mu} \prod_{c' \neq c} \frac{\varepsilon_i - \widetilde{\varepsilon}_{c'}}{\widetilde{\varepsilon}_c - \widetilde{\varepsilon}_{c'}} \right) \psi_i(\mathbf{r}_\mu). \tag{2.12}$$

Combining Eq. (2.12) with Eq. (1.76), we obtain directly $\chi_0 g_j$ as

$$\chi_0 g_j \approx \sum_{\mu=1}^{N_\mu} W_\mu g_j(\mathbf{r}_\mu). \tag{2.13}$$

It should be noted that in Eq. (2.13), we have avoided the explicit reconstruction of the solution vectors ζ_{ij} as in Eqs. (2.6), of which the computational cost is again $\mathcal{O}(N_e^4)$.

Formally, Eq. (2.13) can further be simplified by defining a matrix Π with N_μ columns, which consists of selected columns of a permutation matrix, *i.e.*$\Pi = \widetilde{\Pi}_{:,1:N_\mu}$ as the first N_μ columns of the permutation matrix obtained from pivoted QR decomposition. More specifically, $\Pi_\mu = e_{\mathbf{r}_\mu}$ and $e_{\mathbf{r}_\mu}$ is a unit vector with only one nonzero entry at $\mathbf{r}_\mu$ such that $e_{\mathbf{r}_\mu}^T g_j = g_j(\mathbf{r}_\mu)$. Then

$$\chi_0 g_j \approx W\Pi^T g_j := \widetilde{\chi}_0 g_j. \tag{2.14}$$

Note that the compressed polarizability operator $\widetilde{\chi}_0 = W\Pi^T$ is formally independent of the right hand side vector $\{g_j\}$, and the rank of $\widetilde{\chi}_0$ is only N_μ, while the singular values of χ_0 have a much slower decay rate. This is because $\widetilde{\chi}_0$ only agrees with χ_0 when applied to vectors g_j. In other words, the difference between $\widetilde{\chi}_0$ and χ_0 is not controlled in the space orthogonal to that spanned by G. Alg. 2 summarizes the algorithm for computing the compressed polarizability operator $\widetilde{\chi}_0$.

The computational complexity of Alg. 2 can be analyzed as follows. For simplicity we neglect all possible logarithmic factors in the complexity analysis, The cost for constructing the compressed representation of M is $\mathcal{O}(N_e^3)$. Eqs. (2.11) require solving $N_c N_\mu \sim \mathcal{O}(N_e)$ equations. Assuming the computational cost for applying H to a vector is $\mathcal{O}(N_g)$, and assuming that the number of iterations using an iterative solver to solve Eqs. (2.11) is bounded by a constant, then the cost for solving all equations is dominated by the computation of $\{Q\xi_\mu\}$ which is $\mathcal{O}(N_e^3)$. In order to construct W, for each μ and i, we can first compute the term in the parenthesis in the right hand side of Eq. (2.12). Then the computational complexity for constructing W is again $\mathcal{O}(N_e^3)$. Therefore, the overall asymptotic computational cost for constructing the compressed polarizability operator $\widetilde{\chi}_0$ is $\mathcal{O}(N_e^3)$. In practice, we find that the computational cost is dominated by solving the $\mathcal{O}(N_e)$ linear equations in step 2 of Alg. 2.

Algorithm 2: Computing compressed polarizability operator $\widetilde{\chi}_0$.

Input: Vectors $\{g_j\}$. Hamiltonian matrix H.
Eigenpairs corresponding to occupied orbitals $\{\psi_i, \varepsilon_i\}$
Output: $\widetilde{\chi}_0 = W\Pi^T$.

1. Use Alg. 1 to obtain $\{\mathbf{r}_\mu\}$, Π, and hence the compressed representation of M.
2. Solve compressed Eqs. (2.11).
3. Compute W using Eq. (2.12).

2.3.2 Compression of χ

According to Eq. (2.5), $\chi_0 G$ is the leading order approximation to $U = \chi G$, and this approximation can be inaccurate if $\chi_0 f_{\text{hxc}}$ is not small. From the perspective of section 2.3.1, the self-consistent solution to the Dyson equation (2.5) introduces two additional difficulties: 1) we need to find compressed representation $\widetilde{\chi}_0$ that agrees with χ_0 when applied to both G and $v_{\text{hxc}}U$; 2) U is not known *a priori*. Hence if we apply Alg. 2 directly, we may need to increase the rank of $\widetilde{\chi}_0$ to $2N_\mu$ or higher to maintain the accuracy. Below we introduce the adaptively compressed polarizability operator (ACP) method that simultaneously addresses the above two difficulties.

We assume that f_{hxc} is invertible, and $f_{\text{hxc}}^{-1} g$ for a vector g can be computed easily. This is the case in the absence of the exchange-correlation kernel f_{xc}, and $f_{\text{hxc}}^{-1} g = v_c^{-1} g$ can simply be obtained by applying the Laplacian operator to g. This approximation is referred to as the "random phase approximation" (RPA) in physics literature [46]. In the presence of f_{xc} in the LDA and GGA formulations, f_{xc} is a diagonal matrix, and $f_{\text{hxc}}^{-1} g = (f_{\text{xc}} + v_c)^{-1} g$ can be solved using iterative methods.

We introduce the following change of variable

$$U = \widetilde{U} - B, \quad B = f_{\text{hxc}}^{-1} G, \tag{2.15}$$

and the Dyson equation (2.5) becomes

$$\widetilde{U} = \chi_0 f_{\text{hxc}} \widetilde{U} + B. \tag{2.16}$$

The advantage of using Eq. (2.16) over (2.5) is that formally, we only need to find $\widetilde{\chi}_0$ that is accurate when applied to $f_{\text{hxc}}\widetilde{U}$. In an iterative algorithm, for a given matrix $\widetilde{U}$, we can use Alg. 2 to construct $\widetilde{\chi}_0[\widetilde{U}]$ by replacing G with $f_{\text{hxc}}\widetilde{U}$, with $\widetilde{U}$ in the bracket to highlight the $\widetilde{U}$-dependence of the compression scheme, i.e.

$$\widetilde{U} = \widetilde{\chi}_0[\widetilde{U}] f_{\text{hxc}} \widetilde{U} + B. \tag{2.17}$$

We note that when self-consistency is reached for Eq. (2.17) with the self-consistent solution denoted by $\widetilde{U}^*$, $\widetilde{\chi}_0[\widetilde{U}^*] f_{\text{hxc}} \widetilde{U}^*$ remains a good approximation to $\chi_0 f_{\text{hxc}} \widetilde{U}^*$, even if $\widetilde{U}^*$ deviates

away from the initial guess. In each step, the approximate rank of $\widetilde{\chi}_0[\widetilde{U}]$ remains to be N_μ. Hence $\widetilde{\chi}_0[\widetilde{U}]$ is adaptive to the solution $\widetilde{U}$, and hence is called the adaptively compressed polarizability operator (ACP). This concept of adaptively constructing a low rank matrix shares similar spirit to the recently developed adaptively compressed exchange operator (ACE) for the efficient solution of Hartree-Fock-like calculations [33].

Eq. (2.17) can be solved using the fixed point iteration or more advanced methods for solving fixed point problems, similar to that in Eq. (2.5) in DFPT. However, thanks to the low rank structure of $\widetilde{\chi}_0$ in Eq. (2.14), we can significantly accelerate the convergence. Let us denote the value of $\widetilde{U}$ at the k-th iteration as $\widetilde{U}^k$, which gives rise to the ACP $\widetilde{\chi}_0[\widetilde{U}^k] = W^k(\Pi^k)^T$. Eq. (2.16) indicates that if the magnitude of $\chi_0 f_{\text{hxc}}$ is small, then $\widetilde{U}^0 = B$ is a good initial guess to start the iteration. Then we can reformulate Eq. (2.17) and obtain the following iteration scheme

$$\widetilde{U}^{k+1} = \left(I - W^k(\Pi^k)^T f_{\text{hxc}}\right)^{-1} B = B + W^k \left(I - (\Pi^k)^T f_{\text{hxc}} W^k\right)^{-1} (\Pi^k)^T f_{\text{hxc}} B. \tag{2.18}$$

The second equality in Eq. (2.18) uses the Sherman-Morrison-Woodbury identity for computing the inverse. The cost of the inversion is $\mathcal{O}(N_e^3)$ due to the low rank structure of $\widetilde{\chi}_0[\widetilde{U}^k]$. Numerical results indicate that the iteration scheme (2.18) can converge much more rapidly compared to the fixed point iteration for Eq. (2.5). In fact often two to four iterations are sufficient to obtain results that are sufficiently accurate. Alg. 3 describes the algorithm for using ACP to compute χG.

Algorithm 3: Computing χG with adaptively compressed polarizability operator

---

Input:
Vectors $\{g_j\}$. Stopping criterion δ.
Eigenpairs corresponding to occupied orbitals $\{\psi_i, \varepsilon_i\}$
Output: $U \approx \chi G$

1. Compute $\widetilde{U}^0 = B = f_{\text{hxc}}^{-1} G$. $k \leftarrow 0$.
2. **Do**
   a) Use Alg. 2 by replacing G with $f_{\text{hxc}}\widetilde{U}^k$ to obtain W^k and Π^k, and obtain $\widetilde{\chi}_0^k = W^k(\Pi^k)^T$.
   b) Update $\widetilde{U}^{k+1}$ according to Eq. (2.18).
   c) $k \leftarrow k + 1$

   until $\|\widetilde{U}^k - \widetilde{U}^{k-1}\| < \delta$ or maximum number of iterations is reached.
3. Compute $U \leftarrow \widetilde{U}^k - B$.

2.4 Numerical examples of ACP

In this section, we demonstrate the performance of ACP proposed in section 2.3, and compare it with the density functional perturbation theory (DFPT), and with the finite difference approach (FD) through three examples. The first example consists of a one-dimensional (1D) reduced Hartree-Fock model problem that can be tuned to resemble an insulating or a semi-conducting system. The second example is a two-dimensional (2D) model problem with a periodic triangular lattice structure. The third example is a 2D triangular lattice with defects and random perturbations of the atomic positions. Since our computational domain involve a large number of atoms, our treatment of using a system of finite size with periodic boundary conditions is equivalent to the Gamma point sampling strategy of the Brillouin zone for an infinite sized system [40]. All results in this section are performed on a single computational core of a 1.4 GHz processor with 256 GB memory using MATLAB.

2.4.1 One-dimensional reduced Hartree-Fock model

The 1D reduced Hartree-Fock model was introduced by Solovej [53], and has been used for analyzing defects in solids in e.g. [9, 10]. The simplified 1D model neglects the contribution of the exchange-correlation term. As discussed in previous sections, the presence of exchange-correlation functionals at LDA/GGA level does not lead to essential difficulties in phonon calculations.

The Hamiltonian in our 1D reduced Hartree-Fock model is given by

$$H[\rho] = -\frac{1}{2}\frac{d^2}{dx^2} + \int K(x,y)\left(\rho(y) + m(y)\right)\,\mathrm{d}y. \tag{2.19}$$

Here $m(x) = \sum_I m_I(x - R_I)$ is the summation of pseudocharges. Each function $m_I(x)$ takes the form of a one-dimensional Gaussian

$$m_I(x) = -\frac{Z_I}{\sqrt{2\pi\sigma_I^2}}\exp\left(-\frac{x^2}{2\sigma_I^2}\right), \tag{2.20}$$

where Z_I is an integer representing the charge of the I-th nucleus. In our numerical simulation, we choose all σ_I to be the same.

Instead of using a bare Coulomb interaction which diverges in 1D when x is large, we use a Yukawa kernel as the regularized Coulomb kernel

$$K(x,y) = \frac{2\pi e^{-\kappa|x-y|}}{\kappa\epsilon_0}, \tag{2.21}$$

which satisfies the equation

$$-\frac{d^2}{dx^2}K(x,y) + \kappa^2 K(x,y) = \frac{4\pi}{\epsilon_0}\delta(x-y). \tag{2.22}$$

As $\kappa \to 0$, the Yukawa kernel approaches the bare Coulomb interaction given by the Poisson equation. The parameter ϵ_0 is used so that the magnitude of the electron static contribution is comparable to that of the kinetic energy. The ion-ion repulsion energy E_{II} is also computed using the Yukawa interaction K in the model systems.

The parameters used in the model are chosen as follows. Atomic units are used throughout the discussion unless otherwise mentioned. For all systems tested in this subsection, the distance between each atom and its nearest neighbor is set to 2.4 a.u.. The Yukawa parameter $\kappa = 0.1$. The nuclear charge Z_I is set to 1 for all atoms, and σ_I is set to be 0.3. The Hamiltonian operator is represented in a plane wave basis set.

By adjusting the parameter $\epsilon_0 = 1.0$ or 10, the reduced Hartree-Fock model can be tuned to resemble an insulator or a semiconductor, respectively. We apply ACP to both cases. We use Anderson mixing for SCF iterations, and the linearized eigenvalue problems are solved by using the locally optimal block preconditioned conjugate gradient (LOBPCG) solver [29].

For systems of size $N_A = 60$, the converged electron density ρ associated with the two 1D test cases as well as the 70 smallest eigenvalues associated with the Hamiltonian defined by the converged ρ are shown in Fig. 2.3. For the insulator case, the electron density fluctuates between 0.1935 and 0.6927. There is a finite HOMO-LUMO gap, $\varepsilon_g = \varepsilon_{61} - \varepsilon_{60} = 0.6763$. The electron density associated with the semiconductor case is relatively uniform in the entire domain, with the fluctuation between 0.3576 and 0.4788. The corresponding band gap is 0.1012. Fig. 2.3 is obtained by a system with 60 atoms, and we find that systems with different sizes show similar patterns in the band structure for both insulating and semiconducting systems, respectively.

All numerical results of the ACP method below are benchmarked with results obtained from DFPT. In order to demonstrate the effectiveness of the ACP formulation for compressing $U = \chi G$, we directly measure the relative L^2 error, defined as $\|U - U^{\mathrm{ACP}}\|_2 / \|U\|_2$, where U^{ACP} is obtained from Alg. 3. We also report the error of the phonon spectrum by computing the L^∞ error of the phonon frequencies $\{\omega_k\}$. Due to the presence of acoustic phonon modes for which ω_k is close to 0, we report the absolute error instead of the relative error for the phonon frequencies. In DFPT, we use MINRES [47] to solve the Sternheimer equations iteratively. The initial guess vectors for the solutions are obtained from previous iterations in the Dyson equation to reduce the number of matrix-vector multiplications. The same strategy for choosing the initial guess is implemented for the ACP formulation as well. Anderson mixing is used to accelerate the convergence of Dyson equations in DFPT. In ACP we find that the fixed point iteration (2.18) is sufficient for fast convergence.

In Tables 2.1 and 2.2, we calibrate the accuracy of our algorithm with different number of Chebyshev points N_c and different number of columns N_μ, for both insulating and semiconducting systems, respectively. We choose $N_\mu = lN_e$, where $l = 3, 4, \ldots, 8$. Tables 2.1 and 2.2 show that for both insulating and semiconducting systems, with fixed Chebyshev interpolation points N_c, the numerical accuracy increases monotonically with respect to N_μ, until limited by the accuracy of the Chebyshev interpolation procedure. Note that when the accuracy is limited by the Chebyshev interpolation, the error can saturate as shown in each column of both Tables 2.1 and 2.2. Similarly the increase of Chebyshev interpolation

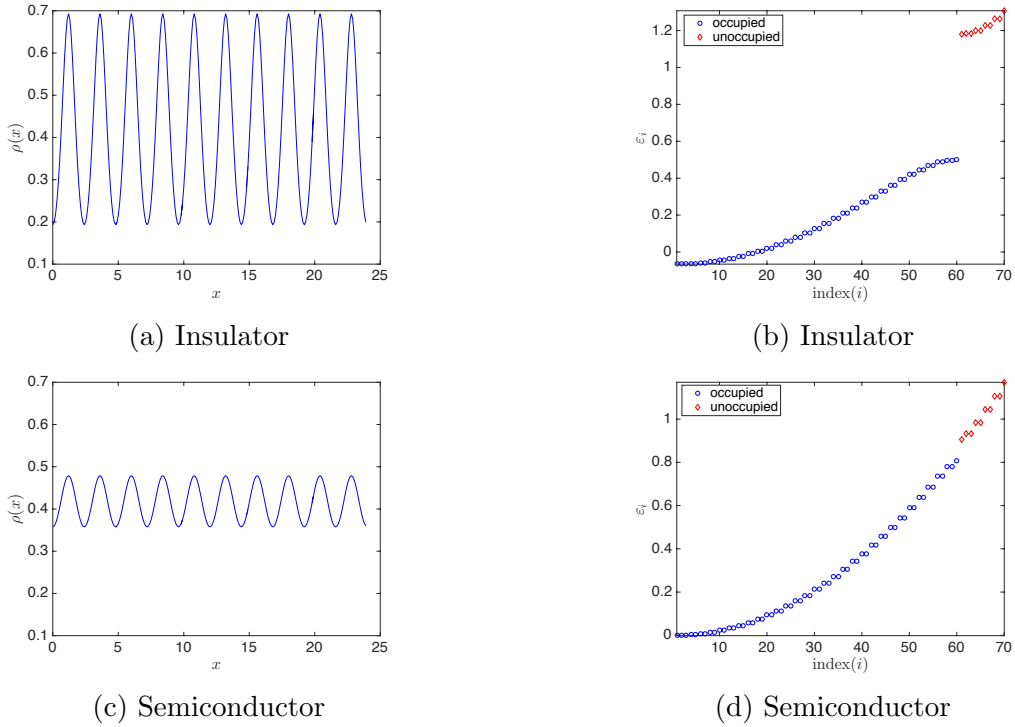

(a) Insulator (b) Insulator

(c) Semiconductor (d) Semiconductor

Figure 2.3: The electron density $\rho(x)$ of the 60-atom (a) insulating, and (c) semiconducting systems in the left panel. The corresponding occupied (blue circles) and unoccupied eigenvalues (red diamonds) are shown in the right panel in (b), (d), respectively.

reduces the error until being limited by the choice of N_μ. When both N_μ and N_c are large enough, the error of $\chi_0 G$ can be less than 10^{-6}.

In order to show how N_c scales with respect to the size of $\varepsilon_g/|\mathcal{I}|$, we adjust the parameter $\epsilon_0 = 1.8^{i-1}, i = 1, \ldots, 6$ to get systems with different band gaps. The result is reported in Fig. 2.4. By selecting $N_\mu = 6N_e$, the number of Chebyshev nodes which is required to get relative L^2 error $|\widetilde{\chi}_0 G - \chi_0 G|/|\chi_0 G| \sim 10^{-5}$ scales as $\sqrt{\varepsilon_g/|\mathcal{I}|}$, which matches the analysis in section 2.3.1.

In Table 2.3, we choose N_μ based on the entries of $\widetilde{R}$ as is shown in Alg. 1, and compare the results to those obtained from the FD. In the FD approach, we set the convergence tolerance for LOBPCG to be 10^{-6}, and the SCF tolerance to be 10^{-8}. $\delta = 0.01$ denotes the deviation of atom positions to their equilibrium ones. We remark that the varying δ from 0.01 to 0.0001 does not change too much in the phonon spectrum. The same parameters for SCF and LOBPCG are used to converge the ground state calculation in the ACP formulation. The absolute error of the phonon spectrum is smaller than 10^{-3}. The ACP formulation can lead to very accurate phonon spectrum by solving a relatively small number of equations.

In order to demonstrate the effectiveness of the adaptive compression strategy, the relative L^2 error for the approximation of $U = \chi G$ with respect to the iteration in Alg. 3 is given in

N_c \ N_μ	$3N_e$	$4N_e$	$5N_e$	$6N_e$	$7N_e$	$8N_e$
5	6.90E-03	8.91E-04	7.56E-05	9.17E-06	8.49E-06	8.45E-06
10	6.83E-03	7.83E-04	7.31E-05	2.32E-06	4.65E-07	3.40E-07
15	7.84E-03	8.66E-04	4.92E-05	2.59E-06	3.22E-07	1.11E-07
20	7.53E-03	8.20E-04	5.61E-05	2.68E-06	2.93E-07	2.89E-07
25	8.77E-03	8.80E-04	5.48E-05	2.41E-06	3.95E-07	1.23E-07
30	1.08E-02	8.04E-04	5.71E-05	2.95E-06	3.36E-07	2.76E-07

Table 2.1: The relative L^2 error $|\widetilde{\chi}_0 G - \chi_0 G|/|\chi_0 G|$ for the insulating system with $\varepsilon_g/|\mathcal{I}| = 1.1911$.

N_c \ N_μ	$3N_e$	$4N_e$	$5N_e$	$6N_e$	$7N_e$	$8N_e$
5	2.87E-02	1.02E-02	1.01E-02	1.01E-02	1.01E-02	1.01E-02
10	3.96E-02	4.99E-04	1.82E-04	1.71E-04	1.71E-04	1.71E-04
15	1.75E-02	6.30E-04	6.07E-05	9.33E-06	5.59E-06	4.78E-06
20	4.84E-02	4.47E-04	7.04E-05	8.45E-06	3.24E-06	4.05E-07
25	3.04E-02	5.08E-04	6.95E-05	6.71E-06	2.55E-06	4.57E-07
30	2.29E-02	5.50E-04	5.95E-05	9.66E-06	2.56E-06	3.69E-07

Table 2.2: The relative L^2 error $|\widetilde{\chi}_0 G - \chi_0 G|/|\chi_0 G|$ for the semiconducting system with $\varepsilon_g/|\mathcal{I}| = 0.1253$.

Method and parameter	L^∞-norm error
FD $\delta = 0.01$	5.6779e-04
ACP $N_\mu = 241$ for $\epsilon = 10^{-3}$	3.6436e-04
ACP $N_\mu = 359$ for $\epsilon = 10^{-5}$	2.7380e-06

Table 2.3: L^∞ error of the phonon spectrum. System is insulating with size $N_A = 60$. Chebyshev nodes $N_c = 20$. N_μ is determined such that $|\widetilde{R}_{N_\mu+1,N_\mu+1}| < \epsilon|\widetilde{R}_{1,1}| \leq |\widetilde{R}_{N_\mu,N_\mu}|$ in Alg. 1.

Fig. 2.5. For $\epsilon = 10^{-5}$, the error is around 10^{-5} after 4 iterations. For $\epsilon = 10^{-3}$, the error is reduced to 0.0008. In this case, if we stop after the first iteration in Alg. 3, the relative error of χG is 0.0339. Numerical results show significant improvement after two to four iterations. This indicates that the self-consistent solution of the Dyson equation is crucial for the accurate computation of phonon spectrum.

We perform phonon calculations for systems of size from 30 to 150 for both insulating and

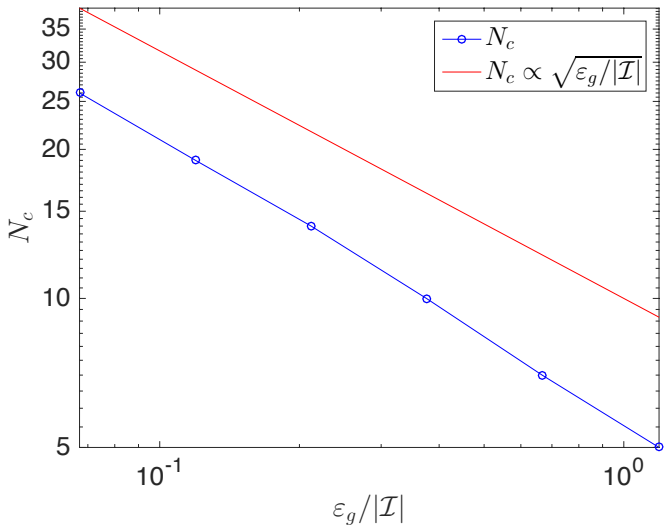

Figure 2.4: Scale of N_c with respect to the size of $\varepsilon_g/|\mathcal{I}|$, compared to the theoretical square root scaling. System size $N_A = 60$. $N_\mu = 6N_e$. The relative L^2 error $|\widetilde{\chi}_0 G - \chi_0 G|/|\chi_0 G| \sim 10^{-5}$.

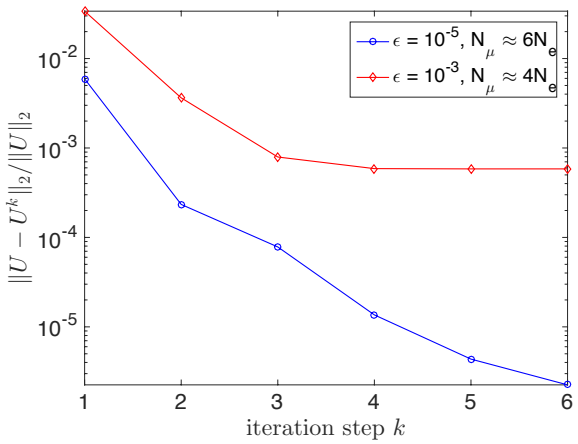

Figure 2.5: Convergence of adaptive compression.

semiconducting systems. In terms of accuracy, Fig. 2.6 shows that as N_μ increases linearly with respect to the system size, the accuracy of phonon spectrum (L^∞ error) remains to be roughly the same, which is empirically around the $\epsilon = 10^{-3}$ used to determine N_μ in Alg. 1. For the computation of the phonon frequency, we find that $N_c = 20$ and $N_\mu = 4N_e$ is sufficient to achieve error around 10^{-3}, and the phonon spectrum is already indistinguishable

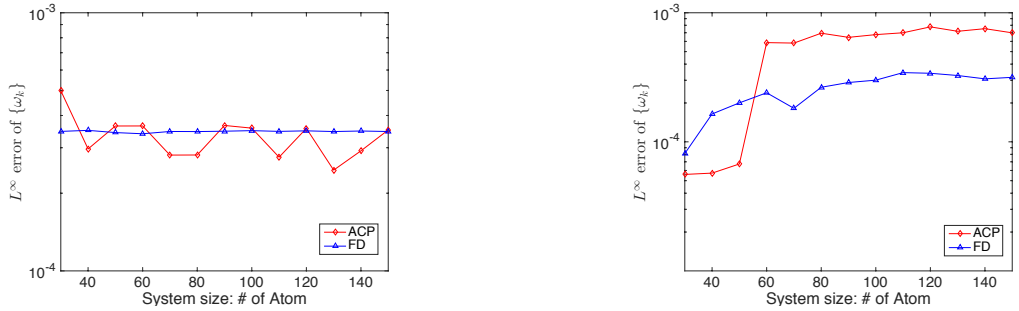

(a) Insulator (b) Semiconductor

Figure 2.6: L^∞ error of the phonon frequencies $\{\omega_k\}$ obtained from ACP and FD. For ACP formulation $N_c = 20$. $N_\mu \approx 4N_e$.

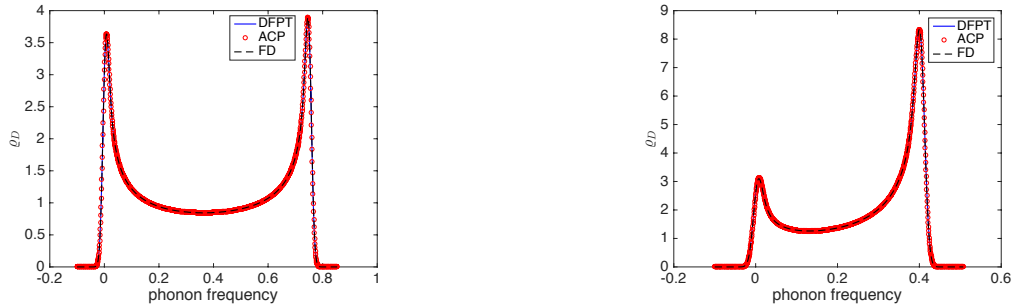

(a) Insulator (b) Semiconductor

Figure 2.7: Phonon spectrum for the 1D systems computed using ACP, DFPT, and FD, for both (a) insulating and (b) semiconducting systems.

from that obtained from DFPT. Fig. 2.7 reports the phonon spectrum ϱ_D for the systems of size $N_A = 150$. We remark that Fig. 2.7 plots the density of states ϱ by replacing the Dirac-δ distribution in Eq. 1.65 with regularized delta function

$$\delta_\sigma(x) = \frac{1}{\sqrt{2\pi\sigma^2}} e^{-\frac{x^2}{2\sigma^2}}.$$

Here the smear parameter σ is chosen as 0.01.

To demonstrate the efficiency of the ACP algorithm, Fig. 2.8 compares the computational time of ACP, DFPT, and FD, respectively. We observe that the computational cost of DFPT matches to that of FD due to the choice of initial guess of Sternheimer equations and the Anderson mixing strategy for solving the Dyson equation. Compared to DFPT, the ACP formulation benefits both from that it solves less number of Sternheimer equations, and from that the Sherman-Morrison-Woodbury procedure (2.18) is more efficient than Anderson mixing for solving the Dyson equation. In fact for all systems, Alg. 3 converges within 4 iterations, while the Anderson mixing in DFPT may require 20 iterations or more for systems

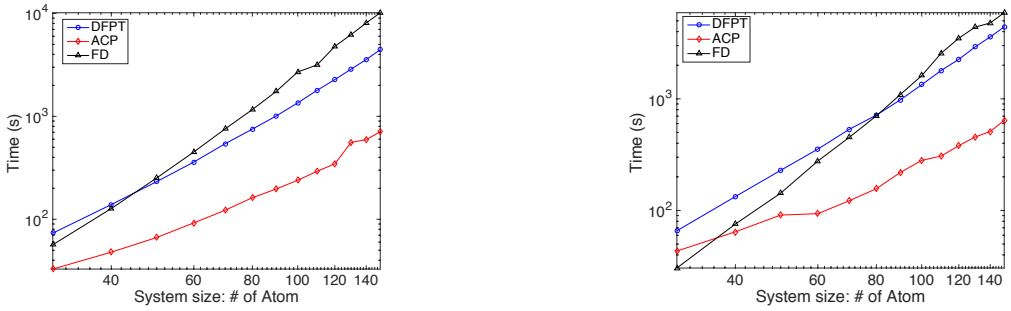

(a) Insulator (b) Semiconductor

Figure 2.8: Computational time of 1D examples. Comparison among DFPT, ACP, and FD for (a) insulating, and (b) semiconducting systems, respectively.

of all sizes. Hence for both insulating and semiconducting systems, the ACP formulation becomes more advantageous than DFPT and FD for systems merely beyond 40 atoms. For the largest system with 150 atoms, ACP is 6.28 and 6.87 times faster than DFPT for insulating and semiconducting systems, respectively.

Method	Insulator	Semiconductor
FD	3.4403	3.3047
DFPT	2.8997	2.9459
ACP	2.5040	2.1065

Table 2.4: Computational scaling measured from $N_A = 90$ to $N_A = 150$.

Table 2.4 measures the slope of the computational cost with respect to system sizes from $N_A = 90$ to $N_A = 150$. In theory, the asymptotic computational cost of FD and DFPT should be $\mathcal{O}(N_e^4)$, and the cost of ACP should be $\mathcal{O}(N_e^3)$. Numerically we observe that for the 1D examples up to $N_A = 150$, the computational scaling is still in the pre-asymptotic regime.

2.4.2 2D lattice model

In the previous section, we have validated the accuracy of ACP compared to both FD and DFPT. We also find that the efficiency of FD and DFPT can be comparable. Hence for the 2D model, we only compare the efficiency and accuracy of ACP with respect to DFPT. Our first example is a periodic triangular lattice relaxed to the equilibrium position. The distance between each atom and its nearest neighbor is set to be 1.2 a.u., and $\epsilon_0 = 0.05$. The nuclear charge Z_I is set to 1 for all atoms, and σ_I is set to be 0.24.

For a system of size $N_A = 98$, the converged electron density ρ as well as the 108 smallest eigenvalues associated with the Hamiltonian at the converged ρ are shown in Fig. 2.9. There

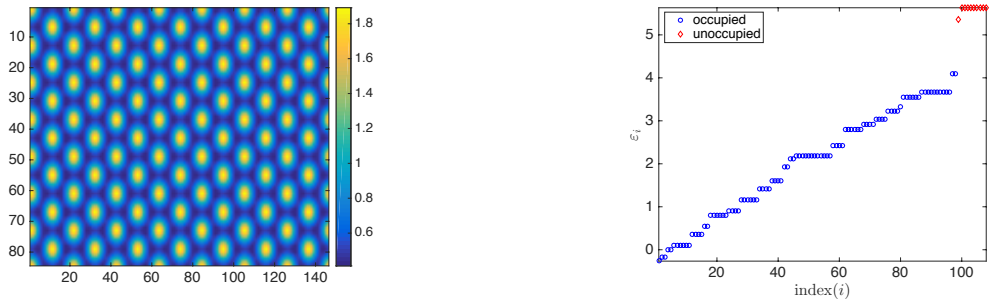

(a) (b)

Figure 2.9: The electron density ρ of the 98-atom insulating system (a), and the occupied and unoccupied eigenvalues (b).

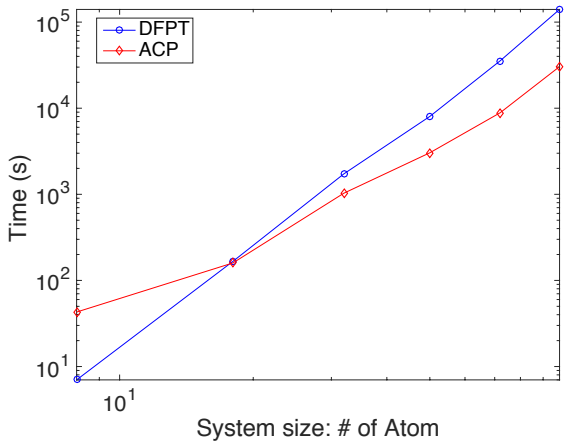

Figure 2.10: Computational time. Comparison of ACP to ACP for the 2D periodic lattice model.

is a finite HOMO-LUMO gap, $\varepsilon_g = \varepsilon_{99} - \varepsilon_{98} = 1.2637$, which suggests that the system is an insulator. Fig. 2.10 shows the computational time of ACP and DFPT as the system size grows from 2×2^2 to 2×7^2. We choose $\epsilon = 10^{-3}$ in Alg. 1, and we find that this amounts to around $N_\mu = 14N_e$ columns selected in the ACP procedure. We choose $N_c = 30$, and hence the ACP formulation solves $420N_e$ equations, compared to the $2N_AN_e = 2N_e^2$ equations needed for DFPT. We iterate Alg. 3 for two iterations. We find that when the system size increases beyond $N_A = 18$, the ACP formulation becomes more advantageous compared to DFPT. For the largest system $N_A = 98$, ACP is 4.61 times faster than DFPT. Table 2.5 measures the computational scaling from $N_A = 32$ to $N_A = 98$, which matches tightly with $\mathcal{O}(N_e^3)$ and $\mathcal{O}(N_e^4)$ theoretical scaling of ACP and DFPT, respectively. Fig. 2.11 reports the phonon spectrum ϱ_D for the system of size $N_A = 98$. Here the smear parameter $\sigma = 0.08$.

Method	Slope
DFPT	3.9295
ACP	3.0249

Table 2.5: Computational scaling measured from $N_A = 32$ to $N_A = 98$.

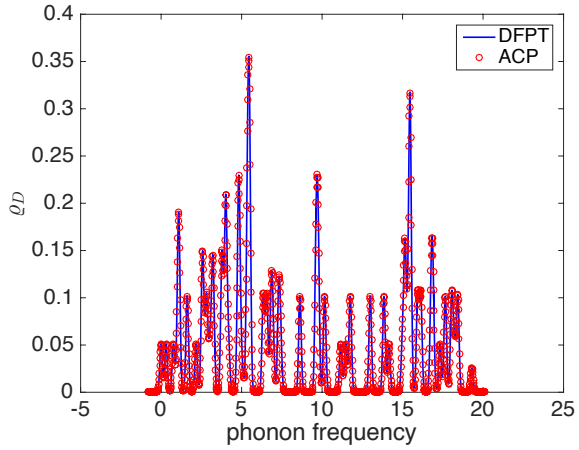

Figure 2.11: Phonon spectrum for the 2D periodic lattice. System size $N_A = 98$. $\epsilon = 10^{-3}$, $N_\mu \approx 14 N_e$.

2.4.3 2D model with random vacancies

Our final example in this section is a 2D triangular lattice with defects. We start from a periodic system with $N_A = 72$ atoms, randomly remove three atoms, and then perform structural relaxation for 15 steps. We terminate the structural relaxation before the system reaches its equilibrium position to obtain a disordered structure.

The converged electron density ρ and the smallest 79 eigenvalues are shown in Fig. 2.12. For this system, there is a finite gap $\varepsilon_g = \varepsilon_{70} - \varepsilon_{69} = 1.3500$. Fig. 2.13 shows the phonon spectrum computed from ACP and DFPT, plotted with the smear parameter $\sigma = 0.08$. The computational time for DFPT is 53883 sec and that for ACP is 8741 sec, and the speedup factor for ACP is 6.16. We observe that for the disordered structure, DFPT requires more iterations to converge, while the number of iterations for ACP to converge can remain to be chosen to be 2. More specifically, compared to the periodic structure with $N_A = 72$, the computational time for DFPT is 35501 sec, while that for ACP is 8854 sec.

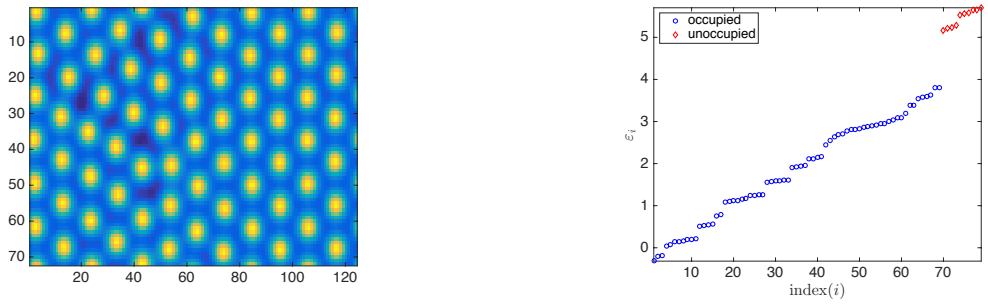

(a) (b)

Figure 2.12: The electron density ρ of the 2D system with defects (a), and the occupied and unoccupied eigenvalues (b).

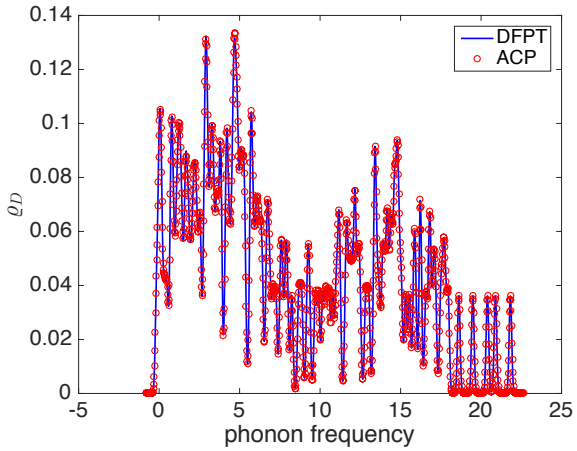

Figure 2.13: Phonon spectrum for the 2D system with defects. System size $N_A = 69$, $\epsilon = 10^{-3}$, $N_\mu \approx 14N_e$.

2.5 Conclusion of chapter 2

We have introduced the adaptively compressed polarizability operator (ACP) formulation. To the extent of our knowledge, the ACP formulation reduces the computational complexity of phonon calculations from $\mathcal{O}(N_e^4)$ to $\mathcal{O}(N_e^3)$ for the first time. This is achieved by reducing the $\mathcal{O}(N_e^2)$ equations in density functional perturbation theory (DFPT) to $\mathcal{O}(N_e)$ equations with systematic control of accuracy. Moreover, the accuracy of the ACP formulation depends weakly on the size of the gap, and hence can be applied to both insulator and semiconductor systems. Our numerical results for model problems indicate that the computational advantage of the ACP formulation can be clearly observed compared to DFPT and finite difference, even for systems of relatively small sizes. While for simplicity our model problems do not include several components of KSDFT calculations for real materials, such

as the nonlocal pseudopotentials and the exchange-correlation kernels, our model problems capture the essential difficulty in phonon calculations, and we expect that the asymptotic behavior of the ACP method for model problems is transferable to real materials simulation. We have also tuned the parameters of our model problem (such as the lattice constants and the band gaps) to mimic those of real materials. In the next chapter, we will present the ACP formulation in the presence of the nonlocal pseudopotential, and its application for computing the phonon spectrum for real materials.

The availability of fast phonon calculations provides a possible way to accelerate structural relaxation optimization of large scale molecules and solids. In this chapter we have restricted ourselves to zero temperature calculations. We will show the extension of the ACP formulation to treat systems at finite temperature and hence metallic systems. We have used phonon calculation as an example to demonstrate the effectiveness of the compressed polarizability operator. The same strategy can be applied to applications of DFPT other than phonon calculations.

Chapter 3

Split Representation of Adaptively Compressed Polarizability Operator

3.1 Introduction

Density functional perturbation theory (DFPT) [3, 21, 5, 11] studies the response of a quantum system under small perturbation, where the quantum system is described at the level of first principle electronic structure theories such as Kohn-Sham density functional theory (KSDFT) [26, 31]. One important application of DFPT is the calculation of vibration properties such as phonons, which can be further used to calculate many physical properties such as infrared spectroscopy, elastic neutron scattering, specific heat, heat conduction, and electron-phonon interaction related behaviors such as superconductivity. DFPT describes vibration properties through a polarizability operator, which characterizes the linear response of the electron density with respect to the perturbation of the external potential. More specifically, in vibration calculations, the polarizability operator needs to be applied to $d \times N_A \sim \mathcal{O}(N_e)$ perturbation vectors, where d is the spatial dimension (usually $d = 3$), N_A is the number of atoms, and N_e is the number of electrons. In general the complexity for solving KSDFT is $\mathcal{O}(N_e^3)$, while the complexity for solving DFPT is $\mathcal{O}(N_e^4)$. It is possible to reduce the computational complexity of DFPT calculations by "linear scaling methods" [19, 45, 8]. Such methods can be successful in reducing the computational cost for systems of large sizes with substantial band gaps, but this can be challenging for medium-sized systems with relatively small band gaps.

The term "phonon calculation" usually describes the calculation of vibrational properties of condensed matter systems. In this paper, we slightly abuse this term to refer to calculations of vibration properties of general systems, including condensed matter systems as well as isolated molecule clusters, since such calculations share the same mathematical structure.

In order to apply the polarizability operator to $\mathcal{O}(N_e)$ vectors, we need to solve $\mathcal{O}(N_e^2)$ coupled Sternheimer equations. On the other hand, when a constant number of degrees of freedom per electron is used, the size of the Hamiltonian matrix is only $\mathcal{O}(N_e)$. Hence

asymptotically there is room to obtain a set of only $\mathcal{O}(N_e)$ "compressed perturbation vectors", which encodes essentially all the information of the $\mathcal{O}(N_e^2)$ Sternheimer equations. In chapter 2, we developed a new method called adaptively compressed polarizability operator (ACP) formulation following this route, and successfully reduces the computational complexity of phonon calculations to $\mathcal{O}(N_e^3)$ for the first time. The ACP formulation does not rely on exponential decay properties of the density matrix as in linear scaling methods, and its accuracy depends weakly on the size of the band gap. Hence the method can be used for phonon calculations of both insulators and semiconductors with small gaps.

There are three key ingredients of the ACP formulation. 1) The Sternheimer equations are equations for shifted Hamiltonians, where each shift corresponds to an energy level of an occupied band. Hence for a general right hand side vector, there are N_e possible energies (shifts). We use a Chebyshev interpolation procedure to disentangle such energy dependence so that there are only constant number of shifts that is independent of N_e. 2) We disentangle the $\mathcal{O}(N_e^2)$ right hand side vectors in the Sternheimer equations using the recently developed interpolative separable density fitting procedure, to compress the right-hand-side vectors. 3) We construct the polarizability operator by adaptive compression so that the operator remains low rank as well as accurate when applying to a certain set of vectors. This make it possible for fast computation of the matrix inversion using methods like Sherman-Morrison-Woodbury. In particular, the ACP method does not employ the "nearsightedness" property of electrons for insulating systems with substantial band gaps as in linear scaling methods [30]. Hence the ACP method can be applied to insulators as well as semiconductors with small band gaps.

In this chapter, we introduce a generalization the ACP formulation for efficient phonon calculations of real materials called split representation of ACP. In the split representation, the nonlocal pseudopotential is taken into account, as well as temperature effects especially for metallic systems. The new split representation maintains the $\mathcal{O}(N_e^3)$ complexity, and improves all key steps in the ACP formulation, including Chebyshev interpolation of energy levels, iterative solution of Sternheimer equations, and convergence of the Dyson equations.

The rest of the chapter is organized as follows. Section 3.2 introduces the basic formulation of KSDFT and DFPT, and reviews the formulation of ACP. Section 3.3 describes the split representation of the ACP formulation. Numerical results are presented in section 3.4, followed by conclusion and discussion in section 3.5.

3.2 Review of adaptively compressed polarizability operator

In this section we briefly review the ACP formulation in the context of phonon calculations for insulating systems using local pseudopotentials. If we label the possible g_{loc} using a single index j, the Sternheimer equation (1.76) can be written as

$$Q(\varepsilon_i - H)Q\zeta_{ij} = Q(\psi_i \odot g_{\text{loc},j}). \tag{3.1}$$

Here we have used the relation diag $[g_{\text{loc}}]\psi = \psi \odot g_{\text{loc}}$ to place g_{loc} and ψ on a more symmetric footing. Then reduction of the computational complexity is achieved by means of reducing the $\mathcal{O}(N_e^2)$ equations in Eq. (3.1) to $\mathcal{O}(N_e)$ equations with systematic control of the accuracy.

The compression of the right hand side vectors is performed via the interpolative separable density fitting method by Lu and Ying [38]. Let us denote by M the collection of right hand side vectors in Eq. (3.1) without the Q factor, i.e. $M_{ij} = \psi_i \odot g_{\text{loc},j}$. Here we have used ij as a stacked column index for the matrix M. The dimension of M is $N_g \times \mathcal{O}(N_e^2)$. Due to the large number of columns of M, we seek for the following interpolative decomposition (ID) type of compression [14] for the matrix M, i.e.

$$M_{ij}(\mathbf{r}) \approx \sum_{\mu=1}^{N_\mu} \xi_\mu(\mathbf{r}) M_{ij}(\mathbf{r}_\mu) \equiv \sum_{\mu=1}^{N_\mu} \xi_\mu(\mathbf{r}) \psi_i(\mathbf{r}_\mu) g_{\text{loc},j}(\mathbf{r}_\mu). \tag{3.2}$$

Here $\{\mathbf{r}_\mu\}_{\mu=1}^{N_\mu}$ denotes a collection of selected row indices (see Fig. 2.1 for an illustration). Mathematically, the meaning of the indices $\{\mathbf{r}_\mu\}$ is clear: Eq. (3.2) simply states that for any grid point $\mathbf{r}$, the corresponding row vector $M_{:}(\mathbf{r})$ can be approximately expressed as the linear combination of the selected rows $\{M_{:}(\mathbf{r}_\mu)\}$. Since $N_g \sim N_e$, as N_e increases, the column dimension of M (which is $\mathcal{O}(N_e^2)$) can be larger than its row dimension (which is N_g), and we can expect that the vectors $\{\psi_i \odot g_j\}$ are approximately linearly dependent. Such observation has been observed in the electronic structure community under the name of density fitting or resolution of identity (RI) [58, 52, 17, 57, 51], and the numerical rank of the matrix M after truncation can be only $\mathcal{O}(N_e)$ with a relatively small pre-constant. This dimension reduction property has also been recently analyzed in [37]. In the context of the interpolative decomposition, our numerical results also indicate that it is sufficient to choose $N_\mu \sim \mathcal{O}(N_e)$, and the pre-constant is small.

One possible way of finding interpolative decomposition is to use a pivoted QR factorization [13, 23]. However, the computational complexity for compressing the dense matrix M using the interpolative decomposition is still $\mathcal{O}(N_e^4)$. The interpolative separable density fitting method [38] employs a two-step procedure to reduce this cost. The first step is to use a fast down-sampling procedure, such as a subsampled random Fourier transform (SRFT) [61], to transform the matrix M into a matrix $\widetilde{M}$ of smaller dimension $N_g \times rN_e$, with r a relatively small constant so that rN_e is slightly larger than N_μ. The second step is to apply the pivoted QR decomposition to $\widetilde{M}$

$$\widetilde{M}^* \widetilde{\Pi} = \widetilde{Q} \widetilde{R}, \tag{3.3}$$

where $\widetilde{\Pi}$ is a permutation matrix and encodes the choice of the row indices $\{\mathbf{r}_\mu\}$ from $\widetilde{M}$. The interpolation vectors $\{\xi_\mu\}$ in Eq. (3.2) can be also be computed from this pivoted QR decomposition. It should be noted that the pre-processing procedure does not affect the quality of the interpolative decomposition, while the cost of the pivoted QR factorization in Eq. (3.3) is now reduced to $\mathcal{O}(N_g N_\mu^2) \sim \mathcal{O}(N_e^3)$.

Once the compressed representation (3.2) is obtained, we solve the following set of modified Sternheimer equations

$$Q(\varepsilon_i - H)Q\widetilde{\zeta}_{c\mu} = Q\xi_\mu, \quad i = 1, \ldots, N_e, \quad \mu = 1, \ldots, N_\mu.$$

Note that there are still $\mathcal{O}(N_e^2)$ equations to solve, but this time the number of equations arises from the energy dependence on the left hand side of the equation. If the band gap is positive, we can solve a set of equations of the form

$$Q(\widetilde{\varepsilon}_c - H)Q\widetilde{\zeta}_{c\mu} = Q\xi_\mu, \quad c = 1, \ldots, N_c, \quad \mu = 1, \ldots, N_\mu. \tag{3.4}$$

where the number of shifts N_c is independent of the system size N_e. For example, this can be achieved using the Chebyshev points on the occupied band $[\varepsilon_1, \varepsilon_{N_e}]$, and the number of Chebyshev points needed to achieve a certain error tolerance scales weakly with respect to the band gap as $\sqrt{|\mathcal{I}|/\varepsilon_g}$. Here ε_g is the band gap and $|\mathcal{I}| = \varepsilon_{N_e} - \varepsilon_1$ is the width of the occupied band [35].

Then define

$$W_\mu = \sum_{i=1}^{N_e} \mathrm{diag}[\psi_i^*] \odot \left(\sum_{c=1}^{N_c} \widetilde{\zeta}_{c\mu} \prod_{c' \neq c} \frac{\varepsilon_i - \widetilde{\varepsilon}_{c'}}{\widetilde{\varepsilon}_c - \widetilde{\varepsilon}_{c'}} \right) \psi_i(\mathbf{r}_\mu) + \text{h.c.}, \tag{3.5}$$

and we can combine Eq. (3.5) with Eq. (1.76) to compute $\chi_0 g_{\mathrm{loc},j}$ as

$$\chi_0 g_{\mathrm{loc},j} \approx \sum_{\mu=1}^{N_\mu} W_\mu g_{\mathrm{loc},j}(\mathbf{r}_\mu). \tag{3.6}$$

Formally, Eq. (3.6) can further be simplified by defining a matrix Π with N_μ columns, which consists of selected columns of a permutation matrix, i.e. $\Pi = \widetilde{\Pi}_{:,1:N_\mu}$ as the first N_μ columns of the permutation matrix obtained from pivoted QR decomposition. More specifically, $\Pi_\mu = e_{\mathbf{r}_\mu}$ and $e_{\mathbf{r}_\mu}$ is a unit vector with only one nonzero entry at $\mathbf{r}_\mu$ such that $e_{\mathbf{r}_\mu}^T g_j = g_j(\mathbf{r}_\mu)$. Then

$$\chi_0 g_{\mathrm{loc},j} \approx W \Pi^T g_{\mathrm{loc},j} := \widetilde{\chi}_0[\{g_{\mathrm{loc},j}\}] g_{\mathrm{loc},j}. \tag{3.7}$$

Note that the notation $\widetilde{\chi}_0[\{g_{\mathrm{loc},j}\}]$ emphasizes the dependence on the vectors that $\widetilde{\chi}_0$ applies to. In other words, $\widetilde{\chi}_0[\{g_{\mathrm{loc},j}\}]$ is designed to only agree with χ_0 when applied to vectors $\{g_{\mathrm{loc},j}\}$, and the difference between $\widetilde{\chi}_0$ and χ_0 is not controlled in the space orthogonal to that spanned by these vectors. The rank of $\widetilde{\chi}_0[\{g_{\mathrm{loc},j}\}]$ is only N_μ, while the singular values of χ_0 have a much slower decay rate.

In the case when only local pseudopotential is used, the Dyson equation (1.58) is simplified as

$$u_j = \chi g_{\mathrm{loc},j} = u_{0,j} + \chi_0 f_{\mathrm{hxc}} u_j. \tag{3.8}$$

Here $u_{0,j} := \chi_0 g_{\mathrm{loc},j}$ is called the non-self-consistent response, and has been computed using the algorithm described above.

In order to solve Eq. (3.8), we not only need to evaluate $\chi_0 g_{\mathrm{loc},j}$, but also the application of χ_0 to the self-consistent response $f_{\mathrm{hxc}}u_j$ which is not known *a priori*. If we build a library of right hand side vectors so that the application of χ_0 remains accurate throughout the iteration process of solving Eq. (3.8), the computational complexity can quickly increase. Instead it is much more efficient to *adaptively compress* the polarizability operator χ_0.

Note that for any given set of functions $\{u_j\}$, we can construct an operator $\widetilde{\chi}_0[\{f_{\mathrm{hxc}}u_j\}]$ so that $\widetilde{\chi}_0$ agrees well with χ_0 when applied to the vectors $\{f_{\mathrm{hxc}}u_j\}$. The Dyson equation can be rewritten as

$$u_j = (I - \widetilde{\chi}_0[\{f_{\mathrm{hxc}}u_j\}])^{-1}u_{0,j}. \tag{3.9}$$

Note that $\widetilde{\chi}_0[\{f_{\mathrm{hxc}}u_j\}]$ is a low rank operator, and the matrix inverse in Eq. (3.9) can be efficiently evaluated using the Sherman-Morrison-Woodbury formula.

Eq. (3.9) yields an iterative scheme

$$u^{k+1} = (I - \widetilde{\chi}_0[\{f_{\mathrm{hxc}}u^k\}])^{-1}u_0. \tag{3.10}$$

In the equation we omitted the j subindex of u. The convergence of the modified fixed point iteration (3.10) can be understood as follows.

At the iteration step k, the scheme and the true solution respectively satisfy

$$\begin{aligned} u^{k+1} &= u_0 + \widetilde{\chi}_0[\{f_{\mathrm{hxc}}u^k\}]f_{\mathrm{hxc}}u^{k+1}, \\ u^* &= u_0 + \chi_0 f_{\mathrm{hxc}}u^*. \end{aligned} \tag{3.11}$$

Let $e^k = u^k - u^*$ be the error at the iteration step k. We have

$$\begin{aligned} e^{k+1} &= \widetilde{\chi}_0[\{f_{\mathrm{hxc}}u^k\}]f_{\mathrm{hxc}}u^{k+1} - \chi_0 f_{\mathrm{hxc}}u^* \\ &= \widetilde{\chi}_0[\{f_{\mathrm{hxc}}u^k\}]f_{\mathrm{hxc}}u^{k+1} - \chi_0 f_{\mathrm{hxc}}u^{k+1} + \chi_0 f_{\mathrm{hxc}}u^{k+1} - \chi_0 f_{\mathrm{hxc}}u^* \\ &= \eta^k + \chi_0 f_{\mathrm{hxc}}e^{k+1}. \end{aligned} \tag{3.12}$$

Here

$$\eta^k := (\widetilde{\chi}_0[\{f_{\mathrm{hxc}}u^k\}] - \chi_0)f_{\mathrm{hxc}}u^{k+1}, \tag{3.13}$$

which characterizes the discrepancy between $\widetilde{\chi}_0$ and χ_0 when applied to the unknown vector $f_{\mathrm{hxc}}u^{k+1}$.

Therefore the error at the $(k+1)$-th step satisfies

$$e^{k+1} = (I - \chi_0 f_{\mathrm{hxc}})^{-1}\eta^k. \tag{3.14}$$

Since χ_0 is negative semi-definite, the norm of $(I - \chi_0 f_{\mathrm{hxc}})^{-1}$ is bounded from above by one. Hence the error goes to zero if the error of compression η^k converges to 0.

To summarize, the ACP formulation has three key ingredients: Compress the right hand side; Disentangle the energy dependence; Adaptively compress the polarizability operator.

3.3 Split representation of the adaptively compressed polarizability operator

In this section, we demonstrate the details of the split representation of the adaptively compressed polarizability operator. It is a generalization of the ACP formulation which takes into account the presense of the nonlocal pseudopotential as well as the treatment of finite temperature.

Recall the Adler-Wiser formula in Eq. (1.72):

$$\mathfrak{X}_0\mathfrak{g} = \sum_{i,a=1}^{\infty} \frac{f_a - f_i}{\varepsilon_a - \varepsilon_i} \psi_a(\psi_a^* \mathfrak{g} \psi_i)\psi_i^*. \tag{3.15}$$

The split representation of the polarizability operator first chooses two cutoff energies $\varepsilon_{\widetilde{N}_{\rm cut}} > \varepsilon_{N_{\rm cut}} \geq \mu$, and splits the right hand side of Eq. (3.15) into two terms

$$\begin{aligned}
\mathfrak{X}_0\mathfrak{g} \approx & \left[\left(\sum_{i=1}^{N_{\rm cut}} \sum_{a=N_{\rm cut}+1}^{\widetilde{N}_{\rm cut}} \frac{f_a - f_i}{\varepsilon_a - \varepsilon_i} \psi_a(\psi_a^* \mathfrak{g} \psi_i)\psi_i^* + \text{h.c.} \right) \right. \\
& \left. + \sum_{i=1}^{N_{\rm cut}} \sum_{a=1}^{N_{\rm cut}} \frac{f_a - f_i}{\varepsilon_a - \varepsilon_i} \psi_a(\psi_a^* \mathfrak{g} \psi_i)\psi_i^* \right] \\
& + \left[\sum_{i=1}^{N_{\rm cut}} \sum_{a=\widetilde{N}_{\rm cut}+1}^{\infty} \frac{f_i}{\varepsilon_i - \varepsilon_a} \psi_a(\psi_a^* \mathfrak{g} \psi_i)\psi_i^* + \text{h.c.} \right] \\
:= & \mathfrak{X}_0^{(s)}\mathfrak{g} + \mathfrak{X}_0^{(r)}\mathfrak{g}.
\end{aligned} \tag{3.16}$$

Here the first and second brackets split $\mathfrak{X}_0\mathfrak{g}$ into a singular component $\mathfrak{X}_0^{(s)}\mathfrak{g}$ and a regular component $\mathfrak{X}_0^{(r)}\mathfrak{g}$, respectively. The Hermitian conjugate appears for the same reason as in Eq. (1.74) when treating insulating systems. $\mathfrak{X}_0^{(s)}$ is called the singular component because for systems with small gaps, the ratio $(f_a - f_i)/(\varepsilon_a - \varepsilon_i)$ can be as large as $1/\varepsilon_g$. When the physical band gap ε_g is small, this term becomes numerically singular to treat in the iterative solution of Sternheimer equations as well as the Chebyshev interpolation. On the other hand, the term $f_i/(\varepsilon_i - \varepsilon_a)$ is bounded from above by $1/\widetilde{\varepsilon}_g$. As the effective gap $\widetilde{\varepsilon}_g$ increases, the magnitude of $\mathfrak{X}_0^{(r)}$ also decreases. In order to efficiently treat the singular part, we assume that the eigenfunctions $\{\psi_k\}_{k=1}^{\widetilde{N}_{\rm cut}}$ have been computed using an iterative eigensolver. The cost for obtaining the additional eigenvectors is modest, given that the ground state DFT calculation already prepares the eigenvectors $\{\psi_k\}_{k=1}^{N_{\rm cut}}$.

The approximation in Eq. (3.16) only comes from that as ε increases above the chemical potential μ, the occupation number $f_i = \frac{1}{1+e^{\beta(\varepsilon_i - \mu)}}$ decays exponentially. Then we can choose

$\varepsilon_{N_{\text{cut}}}$ large enough so that $f\left(\varepsilon_{N_{\text{cut}}+1}\right)$ is sufficiently small and can be approximated by 0. For insulating systems we can simply choose $N_{\text{cut}} = N_e$. The second energy cutoff $\varepsilon_{\widetilde{N}_{\text{cut}}}$ defines an *effective gap* as $\widetilde{\varepsilon}_g = \varepsilon_{\widetilde{N}_{\text{cut}}} - \varepsilon_{N_{\text{cut}}}$, of which the role will be discussed later. The split representation requires the solution of eigenpairs (ε_i, ψ_i) of H for $i \leq \widetilde{N}_{\text{cut}}$. Fig. 3.1 illustrates the position of the cutoff energies along the energy spectrum, with respect to the occupation number given by the Fermi-Dirac distribution.

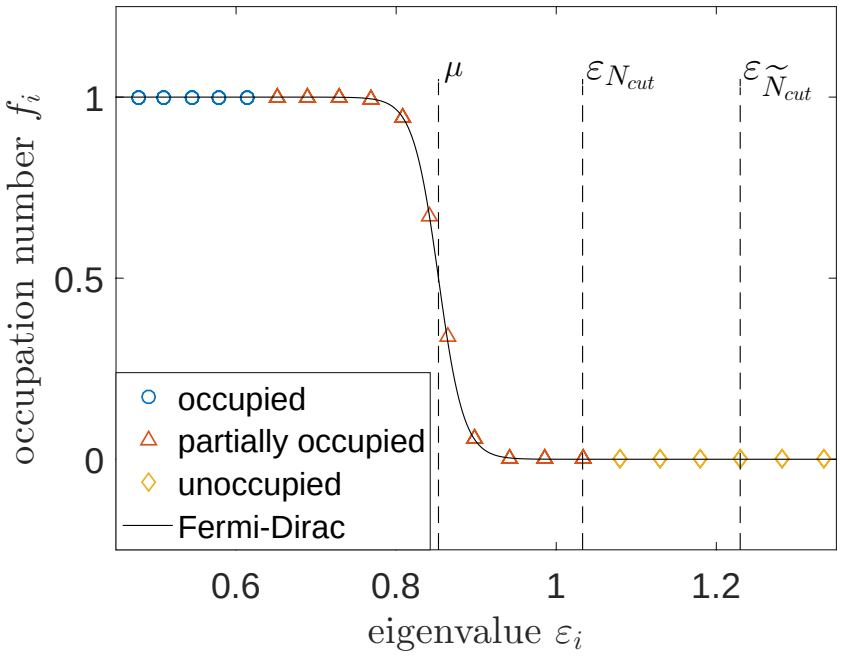

Figure 3.1: Schematic illustration of the cutoff energies with respect to the Fermi-Dirac distribution.

3.3.1 Compression of the regular component of the polarizability operator

One advantage of the split representation is that in the regular component, the contribution from f_a vanishes, and hence $\mathfrak{X}_0^{(r)}\mathfrak{g}$ can be evaluated using Sternheimer equations to eliminate the need of computing all the unoccupied orbitals as follows

$$\mathfrak{X}_0^{(r)}\mathfrak{g} = \sum_{i=1}^{N_{\text{cut}}} f_i Q_c(\varepsilon_i - H)^{-1} Q_c(\mathfrak{g}\psi_i)\psi_i^* + \text{h.c.} \tag{3.17}$$

Here the projection operator $Q_c = I - \sum_{i=1}^{\widetilde{N}_{\text{cut}}} \psi_i\psi_i^*$ projects a vector to the orthogonal space spanned by $\{\psi_i\}_{i=1}^{\widetilde{N}_{\text{cut}}}$. When all order 2 tensors $\{\mathfrak{g}_j\}$ are considered together, Eq. (3.17)

requires the solution of

$$Q_c(\varepsilon_i - H)Q_c\zeta_{ij} = Q_c(\mathfrak{g}_j\psi_i), \quad i = 1, \ldots, N_{\mathrm{cut}}, \quad j = 1, \ldots, d \times N_A. \tag{3.18}$$

Here each solution ζ_{ij} is still a vector. The adaptive compression of $\mathfrak{X}_0\mathfrak{g}_j$ then parallels the adaptive compression of $\chi_0 g_{\mathrm{loc},j}$ as in section 2.3, as detailed below.

The first step is to construct the collection of the right hand side vectors $M_{ij} = \mathfrak{g}_j\psi_i$. Since the kernel of the nonlocal pseudopotential from each atom is compactly supported in the real space, the computational cost for generating M is in fact dominated by the cost associated with the local component $g_{\mathrm{loc},j}$. Hence the overall cost is still $\mathcal{O}(N_e^3)$. The interpolative separable density fitting procedure can then proceed as before, and generate a set of compressed vectors $\{\xi_\mu\}_{\mu=1}^{N_\mu}$ as well as the selected columns $\{\mathbf{r}_\mu\}_{\mu=1}^{N_\mu}$. The interpolation decomposition then reads

$$M_{ij}(\mathbf{r}) = (\mathfrak{g}_j\psi_i)(\mathbf{r}) \approx \sum_\mu \xi_\mu(\mathbf{r})(\mathfrak{g}_j\psi_i)(\mathbf{r}_\mu). \tag{3.19}$$

The second step is the disentanglement of the energy dependence. We choose the Chebyshev interpolation points on the interval $\mathcal{I} = [\varepsilon_1, \varepsilon_{N_{\mathrm{cut}}}]$. Since the number of Chebyshev interpolation points is now controlled by the effective gap as $N_c \sim \mathcal{O}(\sqrt{\mathcal{I}/\widetilde{\varepsilon}_g})$. Note that the gap ϵ_g (which can be small or zero) is now replaced by the effective gap $\widetilde{\varepsilon}_g$. In practice we observe that it is often sufficient to choose N_c to be $5 \sim 10$.

With the Chebyshev interpolation procedure, the Sternheimer equation still takes the form (3.4), with Q replaced by Q_c. The operator $Q_c(\varepsilon_c - H)Q_c$ is a negative definite operator, with eigenvalue bounded from above by $-\widetilde{\varepsilon}_g$. As the effective gap increases, the linear system associated with the Sternheimer equation also becomes better conditioned and the number of MINRES iterations can decrease. Typically we observe that MINRES can converge with around 10 steps.

After the solution of the Sternheimer equations, Eq. (3.17) becomes

$$\mathfrak{X}_0^{(r)}\mathfrak{g}_j \approx \sum_{i=1}^{N_{\mathrm{cut}}}\sum_{\mu=1}^{N_\mu} f_i(\mathfrak{g}_j\psi_i)(\mathbf{r}_\mu)\left(\sum_{c=1}^{N_c}\widetilde{\zeta}_{c\mu}\prod_{c'\neq c}\frac{\varepsilon_i - \widetilde{\varepsilon}_{c'}}{\widetilde{\varepsilon}_c - \widetilde{\varepsilon}_{c'}}\right)\psi_i^* + \mathrm{h.c.} \tag{3.20}$$

Since that $\mathfrak{g}_j$ can be split into a local and a nonlocal component, we have

$$(\mathfrak{g}_j\psi_i)(\mathbf{r}_\mu) = g_{\mathrm{loc},j}(\mathbf{r}_\mu)\psi_i(\mathbf{r}_\mu) + (\mathfrak{g}_{\mathrm{nl},j}\psi_i)(\mathbf{r}_\mu). \tag{3.21}$$

Define

$$\mathfrak{W}_\mu^{(r)} = \sum_{i=1}^{N_{\mathrm{cut}}}\left(\sum_{c=1}^{N_c}\widetilde{\zeta}_{c\mu}\prod_{c'\neq c}\frac{\varepsilon_i - \widetilde{\varepsilon}_{c'}}{\widetilde{\varepsilon}_c - \widetilde{\varepsilon}_{c'}}\right)\psi_i(\mathbf{r}_\mu)f_i\psi_i^* + \mathrm{h.c.}, \tag{3.22}$$

and introduce the permutation matrix Π as in Eq. (3.7), then Eq. (3.20) becomes

$$\begin{aligned}\mathfrak{X}_0^{(r)}\mathfrak{g}_j \approx &\sum_{\mu=1}^{N_\mu} \mathfrak{W}_\mu^{(r)}(\Pi_\mu^T g_{\mathrm{loc},j}) \\ &+ \left[\sum_{i=1}^{N_{\mathrm{cut}}}\sum_{\mu=1}^{N_\mu} f_i(\mathfrak{g}_{\mathrm{nl},j}\psi_i)(\mathbf{r}_\mu)\left(\sum_{c=1}^{N_c}\widetilde{\zeta}_{c\mu}\prod_{c'\neq c}\frac{\varepsilon_i-\widetilde{\varepsilon}_{c'}}{\widetilde{\varepsilon}_c-\widetilde{\varepsilon}_{c'}}\right)\psi_i^* + \mathrm{h.c.}\right]\end{aligned} \tag{3.23}$$

At first glance, Eq. (3.23) does not lead to any simplification compared to Eq. (3.20). However, since the nonlocal component of $\mathfrak{g}_j$ is compactly supported, for each $\mathfrak{g}_{\mathrm{nl},j}$ there are only $\mathcal{O}(1)$ number of points $\{\mathbf{r}_\mu\}$ that contributes to $(\mathfrak{g}_{\mathrm{nl},j}\psi_i)(\mathbf{r}_\mu)$. Hence the last term in Eq. (3.23) is much easier to evaluate than the direct evaluation of Eq. (3.20).

3.3.2 Compression of the singular component of the polarizability operator

In practical calculations, numerical results indicate that it can be sufficient to choose $\widetilde{N}_{\mathrm{cut}} \leq 2N_e$, and hence the computation of $\mathfrak{X}_0^{(s)}\mathfrak{g}$ can even be directly evaluated according to Eq. (3.16). Compared to Eq. (1.72), the computation of $\mathfrak{X}_0^{(s)}\mathfrak{g}$ still scales as $\mathcal{O}(N_e^4)$, but the preconstant is much smaller. In this section we demonstrate that with a contour integral reformulation, we can compress the singular component as well with $\mathcal{O}(N_e^3)$ complexity.

According to the derivation in Appendix A, $\mathfrak{X}_0^{(s)}\mathfrak{g}$ can be evaluated using the contour integral formulation as

$$\begin{aligned}\mathfrak{X}_0^{(s)}\mathfrak{g} = &\left[\frac{1}{2\pi\imath}\oint_{\mathcal{C}} f(z)(z-H_{c,2})^{-1}\mathfrak{g}(z-H_{c,1})^{-1}\,\mathrm{d}z + \mathrm{h.c.}\right] \\ &+ \frac{1}{2\pi\imath}\oint_{\mathcal{C}} f(z)(z-H_{c,1})^{-1}\mathfrak{g}(z-H_{c,1})^{-1}\,\mathrm{d}z\end{aligned} \tag{3.24}$$

Here $H_{c,1} = \sum_{i=1}^{N_{\mathrm{cut}}}\psi_i\varepsilon_i\psi_i^*, H_{c,2} = \sum_{i=N_{\mathrm{cut}}+1}^{\widetilde{N}_{\mathrm{cut}}}\psi_i\varepsilon_i\psi_i^*$ are the Hamiltonian operators projected to the subspace spanned by the first N_{cut} states, and to the subspace spanned by the following $(\widetilde{N}_{\mathrm{cut}} - N_{\mathrm{cut}})$ states, respectively. Before moving on to further discussion, we note that the numerically exact spectral decomposition of $H_{c,1}$ and $H_{c,2}$ is the key to reducing the complexity.

The contour integral in Eq. (3.24) can be discretized to obtain a numerical scheme. Let the integration nodes and weights be denoted by $\{z_p, \omega_p\}_{p=1}^{N_p}$, i.e.

$$\frac{1}{2\pi\imath}\oint_{\mathcal{C}} h(z)\,\mathrm{d}z \approx \sum_{p=1}^{N_p}\omega_p h(z_p), \tag{3.25}$$

for suitable $h(z)$, and the discretization scheme can be obtained using rational approximation methods [36, 43, 42]. Then we have

$$\begin{aligned}\mathfrak{X}_0^{(s)}\mathfrak{g}_j &\approx \left[\sum_{p=1}^{N_p}\omega_p(z_p-H_{c,2})^{-1}\mathfrak{g}_j(z_p-H_{c,1})^{-1}+\text{h.c.}\right]\\ &\quad+\sum_{p=1}^{N_p}\omega_p(z_p-H_{c,1})^{-1}\mathfrak{g}_j(z_p-H_{c,1})^{-1}\\ &=\left[\sum_{p=1}^{N_p}\omega_p\sum_{i=1}^{N_{\text{cut}}}(z_p-H_{c,2})^{-1}(\mathfrak{g}_j\psi_i)(z_p-\varepsilon_i)^{-1}\psi_i^*+\text{h.c.}\right]\\ &\quad+\sum_{p=1}^{N_p}\omega_p\sum_{i=1}^{N_{\text{cut}}}(z_p-H_{c,1})^{-1}(\mathfrak{g}_j\psi_i)(z_p-\varepsilon_i)^{-1}\psi_i^*,\end{aligned}\tag{3.26}$$

where the equality is derived from the spectral decompositions of $H_{c,1}, H_{c,2}$. When all $\{\mathfrak{g}_j\}$ are considered together, we use again the interpolative separable density fitting (3.19) and obtain

$$\begin{aligned}\mathfrak{X}_0^{(s)}\mathfrak{g}_j &\approx \left[\sum_{p=1}^{N_p}\omega_p\sum_{i=1}^{N_{\text{cut}}}(z_p-H_{c,2})^{-1}\sum_{\mu=1}^{N_\mu}\xi_\mu(\mathfrak{g}_j\psi_i)(\mathbf{r}_\mu)(z_p-\varepsilon_i)^{-1}\psi_i^*+\text{h.c.}\right]\\ &\quad+\sum_{p=1}^{N_p}\omega_p\sum_{i=1}^{N_{\text{cut}}}(z_p-H_{c,1})^{-1}\sum_{\mu=1}^{N_\mu}\xi_\mu(\mathfrak{g}_j\psi_i)(\mathbf{r}_\mu)(z_p-\varepsilon_i)^{-1}\psi_i^*\\ &=\left[\sum_{i=1}^{N_{\text{cut}}}\sum_{\mu=1}^{N_\mu}(\mathfrak{g}_j\psi_i)(\mathbf{r}_\mu)\left(\sum_{p=1}^{N_p}\widetilde{\zeta}_{2,p\mu}^{(s)}\omega_p(z_p-\varepsilon_i)^{-1}\right)\psi_i^*+\text{h.c.}\right]\\ &\quad+\sum_{i=1}^{N_{\text{cut}}}\sum_{\mu=1}^{N_\mu}(\mathfrak{g}_j\psi_i)(\mathbf{r}_\mu)\left(\sum_{p=1}^{N_p}\widetilde{\zeta}_{1,p\mu}^{(s)}\omega_p(z_p-\varepsilon_i)^{-1}\right)\psi_i^*.\end{aligned}\tag{3.27}$$

In the last equation of (3.27), we have defined the solution $\widetilde{\zeta}_{\theta,p\mu}^{(s)} := (z_p - H_{c,\theta})^{-1}\xi_\mu, \theta = 1, 2$, which can be numerically exactly computed from the spectral decompositions of $H_{c,1}, H_{c,2}$ respectively. We use the same strategy as in Eq. (3.23) to handle the contribution from $(\mathfrak{g}_j\psi_i)(\mathbf{r}_\mu)$. Define

$$\begin{aligned}\mathfrak{W}_\mu^{(s)} &= \left[\sum_{i=1}^{N_{\text{cut}}}\psi_i(\mathbf{r}_\mu)\left(\sum_{p=1}^{N_p}\widetilde{\zeta}_{2,p\mu}^{(s)}\omega_p(z_p-\varepsilon_i)^{-1}\right)\psi_i^*+\text{h.c.}\right]\\ &\quad+\sum_{i=1}^{N_{\text{cut}}}\psi_i(\mathbf{r}_\mu)\left(\sum_{p=1}^{N_p}\widetilde{\zeta}_{1,p\mu}^{(s)}\omega_p(z_p-\varepsilon_i)^{-1}\right)\psi_i^*,\end{aligned}\tag{3.28}$$

and use the same permutation matrix Π as in Eq. (3.7), then Eq. (3.27) becomes

$$\begin{aligned}\mathfrak{X}_0^{(s)}\mathfrak{g}_j \approx & \sum_{\mu=1}^{N_\mu} \mathfrak{W}_\mu^{(s)}(\Pi_\mu^T g_{\mathrm{loc},j}) \\ & + \left[\sum_{i=1}^{N_{\mathrm{cut}}}\sum_{\mu=1}^{N_\mu}(\mathfrak{g}_{\mathrm{nl},j}\psi_i)(\mathbf{r}_\mu)\left(\sum_{p=1}^{N_p}\widetilde{\zeta}_{2,p\mu}^{(s)}\omega_p(z_p-\varepsilon_i)^{-1}\right)\psi_i^* + \mathrm{h.c.}\right] \\ & + \sum_{i=1}^{N_{\mathrm{cut}}}\sum_{\mu=1}^{N_\mu}(\mathfrak{g}_{\mathrm{nl},j}\psi_i)(\mathbf{r}_\mu)\left(\sum_{p=1}^{N_p}\widetilde{\zeta}_{1,p\mu}^{(s)}\omega_p(z_p-\varepsilon_i)^{-1}\right)\psi_i^*.\end{aligned} \tag{3.29}$$

3.3.3 Adaptive compression for solving the Dyson equation

Recall the Dyson equation (1.58), and so far we have computed the non-self-consistent response $\mathfrak{u}_{0,j} := \mathfrak{X}_0\mathfrak{g}_j$ using the split representation. In order to solve the Dyson equation, we still need to evaluate $\mathfrak{X}_0\mathfrak{f}_{\mathrm{hxc}}\mathfrak{u}$ self-consistently. Use the locality structure of $\mathfrak{f}_{\mathrm{hxc}}$ as in Eq. (1.59), we have

$$(\mathfrak{X}_0\mathfrak{f}_{\mathrm{hxc}}\mathfrak{u})(\mathbf{r},\mathbf{r}') = \int \mathfrak{X}_0(\mathbf{r},\mathbf{r}';\mathbf{r}'',\mathbf{r}'')f_{\mathrm{hxc}}(\mathbf{r}'',\mathbf{r}''')\mathfrak{u}(\mathbf{r}''',\mathbf{r}''')\,\mathrm{d}\mathbf{r}''\,\mathrm{d}\mathbf{r}'''. \tag{3.30}$$

It is important to observe that Eq. (3.30) only requires the *diagonal elements* of $\mathfrak{u}$. Hence the self-consistent solution of the Dyson equation (1.58) only requires a set of equations for these diagonal elements:

$$\mathfrak{u}_j(\mathbf{r},\mathbf{r}) = \mathfrak{u}_{0,j}(\mathbf{r},\mathbf{r}) + \int \mathfrak{X}_0(\mathbf{r},\mathbf{r};\mathbf{r}'',\mathbf{r}'')f_{\mathrm{hxc}}(\mathbf{r}'',\mathbf{r}''')\mathfrak{u}(\mathbf{r}''',\mathbf{r}''')\,\mathrm{d}\mathbf{r}''\,\mathrm{d}\mathbf{r}'''. \tag{3.31}$$

Define $u_j(\mathbf{r}) = \mathfrak{u}_j(\mathbf{r},\mathbf{r})$ and $u_{0,j}(\mathbf{r}) = \mathfrak{u}_{0,j}(\mathbf{r},\mathbf{r})$ and use the linear algebra notation, then Eq. (3.31) becomes a reduced Dyson equation

$$u_j = u_{0,j} + \chi_0 f_{\mathrm{hxc}} u_j. \tag{3.32}$$

Note that Eq. (3.32) becomes precisely the same as Eq. (3.8), which does not involve nonlocal pseudopotentials. However, the important difference is that in Eq. (3.32), $u_{0,j}$ is taken from the diagonal elements of $\mathfrak{u}_{0,j}$, which properly takes into account the nonlocal pseudopotential both in the Hamiltonian and in the non-self-consistent response.

Before moving on to the discussion of solving the reduced Dyson equation, we write out the explicit format of the diagonal part $u_{0,j} = \mathfrak{u}_{0,j}$. Define $W_\mu^{(r)}(\mathbf{r}) = \mathfrak{W}_\mu^{(r)}(\mathbf{r},\mathbf{r}), W_\mu^{(s)}(\mathbf{r}) = \mathfrak{W}_\mu^{(s)}(\mathbf{r},\mathbf{r})$, the diagonal part of Eq. (3.23) reads

$$\begin{aligned}\left(\mathfrak{X}_0^{(r)}\mathfrak{g}_j\right)(\mathbf{r},\mathbf{r}) \approx & \sum_{\mu=1}^{N_\mu} W_\mu^{(r)}(\mathbf{r})(\Pi_\mu^T g_{\mathrm{loc},j}) \\ & + \left[\sum_{i=1}^{N_{\mathrm{cut}}}\sum_{\mu=1}^{N_\mu} f_i(\mathfrak{g}_{\mathrm{nl},j}\psi_i)(\mathbf{r}_\mu)\left(\sum_{c=1}^{N_c}\widetilde{\zeta}_{c\mu}(\mathbf{r})\prod_{c'\neq c}\frac{\varepsilon_i-\widetilde{\varepsilon}_{c'}}{\widetilde{\varepsilon}_c-\widetilde{\varepsilon}_{c'}}\right)\psi_i^*(\mathbf{r}) + \mathrm{h.c.}\right].\end{aligned} \tag{3.33}$$

The diagonal part of Eq. (3.29) reads

$$\begin{aligned}\left(\mathfrak{X}_0^{(s)}\mathfrak{g}_j\right)(\mathbf{r},\mathbf{r}) \approx &\sum_{\mu=1}^{N_\mu} W_\mu^{(s)}(\mathbf{r})(\Pi_\mu^T g_{\mathrm{loc},j}) \\ &+ \left[\sum_{i=1}^{N_{\mathrm{cut}}}\sum_{\mu=1}^{N_\mu}(\mathfrak{g}_{\mathrm{nl},j}\psi_i)(\mathbf{r}_\mu)\left(\sum_{p=1}^{N_p}\widetilde{\zeta}_{2,p\mu}^{(s)}(\mathbf{r})\omega_p(z_p-\varepsilon_i)^{-1}\right)\psi_i^*(\mathbf{r}) + \mathrm{h.c.}\right] \\ &+ \sum_{i=1}^{N_{\mathrm{cut}}}\sum_{\mu=1}^{N_\mu}(\mathfrak{g}_{\mathrm{nl},j}\psi_i)(\mathbf{r}_\mu)\left(\sum_{p=1}^{N_p}\widetilde{\zeta}_{1,p\mu}^{(s)}(\mathbf{r})\omega_p(z_p-\varepsilon_i)^{-1}\right)\psi_i^*(\mathbf{r}).\end{aligned} \tag{3.34}$$

The reduced Dyson equation (3.32) can be readily solved using the same adaptive compression strategy in section 2.3. More specifically, we can replace $\mathfrak{g}_j$ by the local potential $\mathrm{diag}[f_{\mathrm{hxc}}u_j]$, and only take the diagonal elements in Eq. (3.23) and (3.29) to obtain $\chi_0 f_{\mathrm{hxc}}u_j$. Moreover, since both the regular part $\chi_0^{(r)}$ and the singular part $\chi_0^{(s)}$ preserve a low-rank nature, Sherman-Morrison-Woodbury formula can still be used in the fixed point iteration. The separated treatment of the singular and regular parts reduces the error of the compressed χ_0 as in Eq. (3.13). Therefore it also accelerates the convergence of the Dyson equation. The complete iteration process to solve the Dyson equations is defined in Alg. 4.

Once the self-consistent $\mathfrak{u}_j(\mathbf{r},\mathbf{r})$ are obtained, one can formally reconstruct $\mathfrak{u}(\mathbf{r},\mathbf{r}')$ by using the split representation again in Eq. (3.23) and (3.29). Finally $\mathfrak{u}_j$ will be integrated with $\mathfrak{g}_{j'}$ as in Eq. (1.67) to compute the Hessian matrix for phonon calculations, which will be further discussed in detail in the next section.

3.3.4 Phonon Calculation

For the purpose of phonon calculation, $\mathfrak{u}_j$ (representing a component of $\dfrac{\partial P}{\partial \mathbf{R}_I}$) will be integrated with $\mathfrak{g}_{j'}$ (representing a component of $\dfrac{\partial V_{\mathrm{ion}}}{\partial \mathbf{R}_J}$) as in Eq. (1.67) to compute the Hessian matrix for phonon calculations. The integration with local components can be readily computed once the self-consistent response $u_j(\mathbf{r})$ is obtained by solving the reduced Dyson equation. The integration with nonlocal components $\mathfrak{g}_{\mathrm{nl},j}$ would require the construction of $\mathfrak{u}(\mathbf{r},\mathbf{r}')$. However since $\mathfrak{g}_{\mathrm{nl},j}$ is compactly supported, one could avoid the full construction of $\mathfrak{u}(\mathbf{r},\mathbf{r}')$ by embedding the integration process into the construction of $\mathfrak{u}(\mathbf{r},\mathbf{r}')$. This is important for maintaining the reduced scaling of the algorithm.

In this section, we show the construction of integral in Eq. (1.68). For simplicity, the indexes I, J are ignored. Starting from the Dyson equation,

$$\mathfrak{u}(\mathbf{r},\mathbf{r}') = (\mathfrak{X}_0\mathfrak{g})(\mathbf{r},\mathbf{r}') + (\mathfrak{X}_0\mathfrak{f}_{\mathrm{hxc}}\mathfrak{u})(\mathbf{r},\mathbf{r}'), \tag{3.35}$$

an element of the Hessian matrix requires calculation of

$$\int \mathfrak{g}(\mathbf{r},\mathbf{r}')\mathfrak{u}(\mathbf{r},\mathbf{r}')\,\mathrm{d}\mathbf{r}\,\mathrm{d}\mathbf{r}' = \int \left[\mathfrak{g}(\mathbf{r},\mathbf{r}')(\mathfrak{X}_0\mathfrak{g})(\mathbf{r},\mathbf{r}') + \mathfrak{g}(\mathbf{r},\mathbf{r}')(\mathfrak{X}_0\mathfrak{f}_{\mathrm{hxc}}\mathfrak{u})(\mathbf{r},\mathbf{r}')\right]\,\mathrm{d}\mathbf{r}\,\mathrm{d}\mathbf{r}'. \tag{3.36}$$

Algorithm 4: Computing $U := [u_j]$ with the split representation of adaptively compressed polarizability operator.

Input:
$\{\mathfrak{g}_j\}$. Stopping criterion δ.
Eigenpairs corresponding to occupied orbitals $\{\psi_i, \varepsilon_i\}, i = 1, \ldots, \widetilde{N}_{\text{cut}}$
Output: $U \approx \chi G$

1. Compute $U_0 := [u_{0,j}]$ using Eq. (3.23) and (3.29) (only the diagonal elements).
2. **Do**
   a) Replace $\{\mathfrak{g}_j\}$ with $\text{diag}[f_{\text{hxc}} u_j^k]$ to obtain $W^{(r)k}$ and $W^{(s)k}$ and Π^k in Eq. (3.22) and (3.28) . Define $W^k = W^{(s)k} + W^{(r)k}$.
   b) Update U^{k+1} using Sherman-Morrison-Woodbury formula

$$\begin{aligned} U^{k+1} &= \left(I - W^k (\Pi^k)^T f_{\text{hxc}}\right)^{-1} U_0 \\ &= U_0 + W^k \left(I - (\Pi^k)^T f_{\text{hxc}} W^k\right)^{-1} (\Pi^k)^T f_{\text{hxc}} U_0 \end{aligned}$$

   .
   c) $k \leftarrow k + 1$

until $\frac{\|U^k - U^{k-1}\|}{\|U^{k-1}\|} < \delta$ or maximum number of iterations is reached.

Recall that $\mathfrak{g}(\mathbf{r}, \mathbf{r}') = g_{\text{loc}}(\mathbf{r})\delta(\mathbf{r}' - \mathbf{r}) + \mathfrak{g}_{\text{nl}}(\mathbf{r}, \mathbf{r}')$, the integral for the local part of can be easily calculated (letting $u(\mathbf{r}) = \mathfrak{u}(\mathbf{r}, \mathbf{r})$)

$$\int \mathfrak{g}_{\text{loc}}(\mathbf{r}, \mathbf{r}')\mathfrak{u}(\mathbf{r}, \mathbf{r}')\, \mathrm{d}\mathbf{r}\, \mathrm{d}\mathbf{r}' = \int g_{\text{loc}}(\mathbf{r}) u(\mathbf{r})\, \mathrm{d}\mathbf{r}. \tag{3.37}$$

For the non-local potential, using Eq. (3.23) and Eq. (3.29), we have

$$\int \mathfrak{g}_{\text{nl}}(\mathbf{r}, \mathbf{r}')\mathfrak{u}(\mathbf{r}, \mathbf{r}')\, \mathrm{d}\mathbf{r}\, \mathrm{d}\mathbf{r}' = \int \mathfrak{g}_{\text{nl}}(\mathbf{r}, \mathbf{r}') \left[(\mathfrak{X}_0 \mathfrak{g})(\mathbf{r}, \mathbf{r}') + (\mathfrak{X}_0 \mathfrak{f}_{\text{hxc}} \mathfrak{u})(\mathbf{r}, \mathbf{r}')\right] \mathrm{d}\mathbf{r}\, \mathrm{d}\mathbf{r}'. \tag{3.38}$$

Recall that $(\mathfrak{f}_{\text{hxc}}\mathfrak{u})(\mathbf{r}, \mathbf{r}') = \delta(\mathbf{r} - \mathbf{r}') \int f_{\text{hxc}}(\mathbf{r}, \mathbf{r}'') u(\mathbf{r}'')\, \mathrm{d}\mathbf{r}''$. So $(\mathfrak{f}_{\text{hxc}}\mathfrak{u})(\mathbf{r}, \mathbf{r}')$ behaves as a local potential g_{loc} when applying $\mathfrak{X}_0$ to it. So the integral in Eq. (3.38) breaks down to four parts:

$$
\begin{aligned}
&\int \mathfrak{g}_{\mathrm{nl}}(\mathbf{r},\mathbf{r}')(\mathfrak{X}_0^{(r)}\mathfrak{g})(\mathbf{r},\mathbf{r}')\,\mathrm{d}\mathbf{r}\,\mathrm{d}\mathbf{r}' \\
&= \int -\sum_{l=1}^{L}\gamma_l(b_l(\mathbf{r})\,\mathrm{d}b_l^*(\mathbf{r}') + \mathrm{d}b_l(\mathbf{r})b_l^*(\mathbf{r}'))(\mathfrak{X}_0^{(r)}\mathfrak{g})(\mathbf{r},\mathbf{r}')\,\mathrm{d}\mathbf{r}\,\mathrm{d}\mathbf{r}' \\
&= -\int \mathrm{d}\mathbf{r}\,\mathrm{d}\mathbf{r}'\sum_{l=1}^{L}\gamma_l(b_l(\mathbf{r})\,\mathrm{d}b_l^*(\mathbf{r}') + \mathrm{d}b_l(\mathbf{r})b_l^*(\mathbf{r}'))\sum_{\mu=1}^{N_\mu}\mathfrak{W}_\mu^{(r)}[\mathfrak{g}](\mathbf{r},\mathbf{r}')(\Pi_\mu[\mathfrak{g}]^T g_{\mathrm{loc}}) \\
&\quad + \Bigg[-\sum_{l=1}^{L}\gamma_l\sum_{i=1}^{N_{\mathrm{cut}}}\sum_{\mu=1}^{N_\mu} f_i(\mathfrak{g}_{\mathrm{nl}}\psi_i)(\mathbf{r}_\mu)\left(\sum_{c=1}^{N_c}\int \mathrm{d}\mathbf{r}\widetilde{\zeta}_{c\mu}(\mathbf{r})b_l(\mathbf{r})\prod_{c'\neq c}\frac{\varepsilon_i-\widetilde{\varepsilon}_{c'}}{\widetilde{\varepsilon}_c-\widetilde{\varepsilon}_{c'}}\right)\int \mathrm{d}\mathbf{r}\psi_i^*(\mathbf{r}')\,\mathrm{d}b_l^*(\mathbf{r}') \\
&\quad -\sum_{l=1}^{L}\gamma_l\sum_{i=1}^{N_{\mathrm{cut}}}\sum_{\mu=1}^{N_\mu} f_i(\mathfrak{g}_{\mathrm{nl}}\psi_i)(\mathbf{r}_\mu)\left(\sum_{c=1}^{N_c}\int \mathrm{d}\mathbf{r}\widetilde{\zeta}_{c\mu}(\mathbf{r})\,\mathrm{d}b_l(\mathbf{r})\prod_{c'\neq c}\frac{\varepsilon_i-\widetilde{\varepsilon}_{c'}}{\widetilde{\varepsilon}_c-\widetilde{\varepsilon}_{c'}}\right)\int \mathrm{d}\mathbf{r}\psi_i^*(\mathbf{r}')b_l^*(\mathbf{r}')\Bigg] \\
&\quad + \text{h.c. of previous bracket}
\end{aligned}
\tag{3.39}
$$

$$
\begin{aligned}
&\int \mathfrak{g}_{\mathrm{nl}}(\mathbf{r},\mathbf{r}')(\mathfrak{X}_0^{(s)}\mathfrak{g})(\mathbf{r},\mathbf{r}')\,\mathrm{d}\mathbf{r}\,\mathrm{d}\mathbf{r}' \\
&= \int -\sum_{l=1}^{L}\gamma_l(b_l(\mathbf{r})\,\mathrm{d}b_l^*(\mathbf{r}') + \mathrm{d}b_l(\mathbf{r})b_l^*(\mathbf{r}'))(\mathfrak{X}_0^{(s)}\mathfrak{g})(\mathbf{r},\mathbf{r}')\,\mathrm{d}\mathbf{r}\,\mathrm{d}\mathbf{r}' \\
&= -\int \mathrm{d}\mathbf{r}\,\mathrm{d}\mathbf{r}'\sum_{l=1}^{L}\gamma_l(b_l(\mathbf{r})\,\mathrm{d}b_l^*(\mathbf{r}') + \mathrm{d}b_l(\mathbf{r})b_l^*(\mathbf{r}'))\sum_{\mu=1}^{N_\mu}\mathfrak{W}_\mu^{(s)}[\mathfrak{g}](\mathbf{r},\mathbf{r}')(\Pi_\mu[\mathfrak{g}]^T g_{\mathrm{loc}}) \\
&\quad + \Bigg[-\sum_{l=1}^{L}\gamma_l\sum_{i=1}^{N_{\mathrm{cut}}}\sum_{\mu=1}^{N_\mu}(\mathfrak{g}_{\mathrm{nl},j}\psi_i)(\mathbf{r}_\mu)\left(\sum_{p=1}^{N_p}\int \mathrm{d}\mathbf{r}\widetilde{\zeta}_{2,p\mu}^{(s)}(\mathbf{r})b_l(\mathbf{r})\omega_p(z_p-\varepsilon_i)^{-1}\right)\int \mathrm{d}\mathbf{r}'\psi_i^*(\mathbf{r}')\,\mathrm{d}b_l^*(\mathbf{r}') \\
&\quad -\sum_{l=1}^{L}\gamma_l\sum_{i=1}^{N_{\mathrm{cut}}}\sum_{\mu=1}^{N_\mu}(\mathfrak{g}_{\mathrm{nl},j}\psi_i)(\mathbf{r}_\mu)\left(\sum_{p=1}^{N_p}\int \mathrm{d}\mathbf{r}\widetilde{\zeta}_{2,p\mu}^{(s)}(\mathbf{r})\,\mathrm{d}b_l(\mathbf{r})\omega_p(z_p-\varepsilon_i)^{-1}\right)\int \mathrm{d}\mathbf{r}'\psi_i^*(\mathbf{r}')b_l^*(\mathbf{r}')\Bigg] \\
&\quad + \text{h.c. of previous bracket} \\
&\quad -\sum_{l=1}^{L}\gamma_l\sum_{i=1}^{N_{\mathrm{cut}}}\sum_{\mu=1}^{N_\mu}(\mathfrak{g}_{\mathrm{nl},j}\psi_i)(\mathbf{r}_\mu)\left(\sum_{p=1}^{N_p}\int \mathrm{d}\mathbf{r}\widetilde{\zeta}_{1,p\mu}^{(s)}(\mathbf{r})b_l(\mathbf{r})\omega_p(z_p-\varepsilon_i)^{-1}\right)\int \mathrm{d}\mathbf{r}'\psi_i^*(\mathbf{r}')\,\mathrm{d}b_l^*(\mathbf{r}') \\
&\quad -\sum_{l=1}^{L}\gamma_l\sum_{i=1}^{N_{\mathrm{cut}}}\sum_{\mu=1}^{N_\mu}(\mathfrak{g}_{\mathrm{nl},j}\psi_i)(\mathbf{r}_\mu)\left(\sum_{p=1}^{N_p}\int \mathrm{d}\mathbf{r}\widetilde{\zeta}_{1,p\mu}^{(s)}(\mathbf{r})\,\mathrm{d}b_l(\mathbf{r})\omega_p(z_p-\varepsilon_i)^{-1}\right)\int \mathrm{d}\mathbf{r}'\psi_i^*(\mathbf{r}')b_l^*(\mathbf{r}')
\end{aligned}
\tag{3.40}
$$

$$
\begin{aligned}
&\int \mathfrak{g}_{\mathrm{nl}}(\mathbf{r},\mathbf{r}')(\mathfrak{X}_0^{(r)}\mathfrak{f}_{\mathrm{hxc}}\mathfrak{u})(\mathbf{r},\mathbf{r}')\,\mathrm{d}\mathbf{r}\,\mathrm{d}\mathbf{r}' \\
=&\int -\sum_{l=1}^{L}\gamma_l(b_l(\mathbf{r})\,\mathrm{d}b_l^*(\mathbf{r}')+\,\mathrm{d}b_l(\mathbf{r})b_l^*(\mathbf{r}'))(\mathfrak{X}_0^{(r)}\mathfrak{f}_{\mathrm{hxc}}\mathfrak{u})(\mathbf{r},\mathbf{r}')\,\mathrm{d}\mathbf{r}\,\mathrm{d}\mathbf{r}' \\
=&-\int \mathrm{d}\mathbf{r}\,\mathrm{d}\mathbf{r}'\sum_{l=1}^{L}\gamma_l(b_l(\mathbf{r})\,\mathrm{d}b_l^*(\mathbf{r}')+\,\mathrm{d}b_l(\mathbf{r})b_l^*(\mathbf{r}'))\sum_{\mu=1}^{N_\mu}\mathfrak{W}_\mu^{(r)}[\mathfrak{f}_{\mathrm{hxc}}\mathfrak{u}](\mathbf{r},\mathbf{r}')(\Pi_\mu[\mathfrak{f}_{\mathrm{hxc}}\mathfrak{u}]^T f_{\mathrm{hxc}}u)
\end{aligned}
\tag{3.41}
$$

$$
\begin{aligned}
&\int \mathfrak{g}_{\mathrm{nl}}(\mathbf{r},\mathbf{r}')(\mathfrak{X}_0^{(s)}\mathfrak{f}_{\mathrm{hxc}}\mathfrak{u})(\mathbf{r},\mathbf{r}')\,\mathrm{d}\mathbf{r}\,\mathrm{d}\mathbf{r}' \\
=&\int -\sum_{l=1}^{L}\gamma_l(b_l(\mathbf{r})\,\mathrm{d}b_l^*(\mathbf{r}')+\,\mathrm{d}b_l(\mathbf{r})b_l^*(\mathbf{r}'))(\mathfrak{X}_0^{(s)}\mathfrak{f}_{\mathrm{hxc}}\mathfrak{u})(\mathbf{r},\mathbf{r}')\,\mathrm{d}\mathbf{r}\,\mathrm{d}\mathbf{r}' \\
=&-\int \mathrm{d}\mathbf{r}\,\mathrm{d}\mathbf{r}'\sum_{l=1}^{L}\gamma_l(b_l(\mathbf{r})\,\mathrm{d}b_l^*(\mathbf{r}')+\,\mathrm{d}b_l(\mathbf{r})b_l^*(\mathbf{r}'))\sum_{\mu=1}^{N_\mu}\mathfrak{W}_\mu^{(s)}[\mathfrak{f}_{\mathrm{hxc}}\mathfrak{u}](\mathbf{r},\mathbf{r}')(\Pi_\mu[\mathfrak{f}_{\mathrm{hxc}}\mathfrak{u}]^T f_{\mathrm{hxc}}u)
\end{aligned}
\tag{3.42}
$$

We remark that the $\mathfrak{W}$ quantity depends on the tensors to which $\mathfrak{X}_0$ is applied. Note that in Eqs. (3.39), (3.40), (3.41), (3.42), terms like $\int \mathrm{d}\mathbf{r}'\psi_i^*(\mathbf{r}')b_l^*(\mathbf{r}')$ appear many times, hence computing and storing them is necessary. Also one important fact is that $\mathfrak{g}_{\mathrm{nl},j}\psi_i(\mathbf{r}_\mu)$ is only non-zero for several $\mathbf{r}_\mu$. This would result in a "fake" summation of N_μ, which is essential in reducing the complexity. Computation of Eq. (3.39) and Eq. (3.40) is only $\mathcal{O}(N_e)$. The complexity is discussed in detail in the following section.

3.3.5 Complexity

In this section we analyze the complexity of phonon calculation using the split representation of ACP formulation, especially those related to nonlocal pseudopotential.

The first part of the algorithm is to compute the diagonal elements $u_{0,j}$ in Eq. (3.33) and (3.34). For the local pseudopotential, the cost of constructing $W^{(r)}$ and $W^{(s)}$ is $\mathcal{O}(N_\mu N_{\mathrm{cut}} N_c N_g) \sim \mathcal{O}(N_e^3)$ and $\mathcal{O}(N_\mu N_{\mathrm{cut}} N_p N_g) \sim \mathcal{O}(N_e^3)$ respectively, since $N_\mu, N_{\mathrm{cut}}, N_g \sim \mathcal{O}(N_e)$, and $N_c, N_p \sim \mathcal{O}(1)$. Note that the construction of $W^{(r)}, W^{(s)}$ does not depend on the index j, hence there is no factor of dN_A involved. For the nonlocal pseudopotential, as is discussed in Section 3.3.1, each nonlocal component of $\mathfrak{g}_j$ is compactly supported in the real space. Denote N_b as the grid points for the support of $\mathfrak{g}_{\mathrm{nl},j}$. Hence for each $\mathfrak{g}_{\mathrm{nl},j}$ there are only $N_b \sim \mathcal{O}(1)$ number of points r_μ that contributes to $(\mathfrak{g}_{\mathrm{nl},j}\psi_i)(\mathbf{r}_\mu)$. So the cost associated with the nonlocal contribution is $\mathcal{O}(dN_A N_{\mathrm{cut}} N_b N_c N_g) \sim \mathcal{O}(N_e^3)$ in Eq. (3.23) and $\mathcal{O}(dN_A N_{\mathrm{cut}} N_b N_p N_g) \sim \mathcal{O}(N_e^3)$ in

Eq. (3.29). Note that the dN_A factor comes from the fact that $\mathfrak{g}_{\mathrm{nl},j}\psi_i(\mathbf{r}_\mu)$ depends on index $j = 1, 2, \ldots, dN_A$.

In every iteration step when solving the reduced Dyson equation, the complexity of the construction of W^k still cost $\mathcal{O}(N_e^3)$, as we just replaced $\mathfrak{g}_j$ by $\mathrm{diag}[f_{\mathrm{hxc}}u_j^k]$. Using Sherman-Morrison-Woodbury formula, the update of U^{k+1} cost $\mathcal{O}(N_g N_\mu dN_A + N_\mu^3 + N_\mu^2 dN_A) \sim \mathcal{O}(N_e^3)$. In practice, we observe we observe that the number of iterations does not increase with respect to the system size. To summarize, we know that the computation of $u_j(\mathbf{r})$ cost $\mathcal{O}(N_e^3)$ in total.

In order to assemble the information stored in $\mathfrak{u}_j$ to obtain the dynamical matrix for phonon calculations, $\mathfrak{u}_j$ will be integrated with $\mathfrak{g}_{j'}$ as in Eq. (1.67). Before we move on to further discussion, we note that $\mathfrak{u}_j(\mathbf{r}, \mathbf{r}'), \mathfrak{W}_\mu(\mathbf{r}, \mathbf{r}')$ are never constructed or stored. They are only stored in its factorized format. The integration with local components can be readily computed once the self-consistent response $u_j(\mathbf{r})$ is obtained by solving the reduced Dyson equation. The corresponding cost is $\mathcal{O}(d^2 N_A^2 N_g)$. The integration with nonlocal components $\mathfrak{g}_{\mathrm{nl},j}$ would require certain off-diagonal entries $\mathfrak{u}(\mathbf{r}, \mathbf{r}')$. However since $\mathfrak{g}_{\mathrm{nl},j}$ is compactly supported, one could avoid the full construction of $\mathfrak{u}(\mathbf{r}, \mathbf{r}')$ by embedding the integration process into the construction of $\mathfrak{u}(\mathbf{r}, \mathbf{r}')$. As shown in Eqs. (3.39) and (3.40), the complexity for this integration is $\mathcal{O}(d^2 N_a^2 N_b N_{\mathrm{cut}} N_c + 2d^2 N_a^2 N_{\mathrm{cut}} N_b N_c) \sim \mathcal{O}(N_e^3)$ and $\mathcal{O}(d^2 N_a^2 N_b N_{\mathrm{cut}} N_p + 2d^2 N_a^2 N_{\mathrm{cut}} N_b N_p) \sim \mathcal{O}(N_e^3)$, respectively. As for Eqs. (3.41) and (3.42), the complexity is $\mathcal{O}(d^2 N_a^2 N_b N_{\mathrm{cut}} N_c) \sim \mathcal{O}(N_e^3)$ and $\mathcal{O}(d^2 N_a^2 N_b N_{\mathrm{cut}} N_p) \sim \mathcal{O}(N_e^3)$, respectively. Diagonalizing the Hessian matrix costs $\mathcal{O}(N_a^3)$. In summary, the complexity of phonon calculation scales as $\mathcal{O}(N_e^3)$. This is further confirmed by numerical examples in 1D in the following section. Table 3.1 summarizes the complexity of all computation steps of split ACP.

Step	Equation	Complexity
Interpolation decomposition	Eq. (3.19)	$\mathcal{O}(N_g dN_A N_{\mathrm{cut}})$ $+\mathcal{O}(N_g N_{\mathrm{cut}} N_\mu)$
Diagonal element construction regular part	Eq. (3.33)	$\mathcal{O}(N_\mu N_{\mathrm{cut}} N_c N_g)$ $+\mathcal{O}(dN_A N_{\mathrm{cut}} N_b N_c N_g)$
Diagonal element construction Singular part	Eq. (3.34)	$\mathcal{O}(N_\mu N_{\mathrm{cut}} N_p N_g)$ $+\mathcal{O}(dN_A N_{\mathrm{cut}} N_b N_p N_g)$
The Dyson equation update	Step 2.(b) in Alg. 4	$\mathcal{O}(N_g N_\mu dN_A)$ $+\mathcal{O}(N_\mu^3 + N_\mu^2 dN_A)$
Reconstruction local potential	Eq. (3.37)	$\mathcal{O}(d^2 N_A^2 N_g)$
Reconstruction nonlocal pseudopotential	Eq. (3.39)	$\mathcal{O}(d^2 N_a^2 N_b N_{\mathrm{cut}} N_c + 2d^2 N_a^2 N_{\mathrm{cut}} N_b N_c)$
	Eq. (3.40)	$\mathcal{O}(d^2 N_a^2 N_b N_{\mathrm{cut}} N_p + 2d^2 N_a^2 N_{\mathrm{cut}} N_b N_p)$
	Eq. (3.41)	$\mathcal{O}(d^2 N_a^2 N_b N_{\mathrm{cut}} N_c)$
	Eq. (3.42)	$\mathcal{O}(d^2 N_a^2 N_b N_{\mathrm{cut}} N_p)$

Table 3.1: Summary of the complexity of each component of the split ACP algorithm.

3.4 Numerical examples

In this section, we demonstrate the performance of split ACP and compare it with DFPT and finite difference (FD) through two examples. The first example consists of a 1D reduced Hartree-Fock model problem that can be tuned to resemble a metallic system. The second one is a 3D aluminum cluster calculation performed using KSSOLV [62], which is a MATLAB toolbox for solving Kohn-Sham equations for small molecules and solids in three-dimensions. KSSOLV uses plane wave expansion to discretize the Kohn-Sham equations. All calculations are carried out using the Berkeley Research Computing (BRC) High Performance Computing service. Each node consists of two Intel Xeon 10-core Ivy Bridge processors (20 cores per node) and 64 GB of memory.

3.4.1 1D reduced Hartree-Fock model with nonlocal pseudopotential

The 1D reduced Hartree-Fock model was introduced by Solovej [53], and has been used for analyzing defects in solids in e.g. [9, 10]. The simplified 1D model neglects the contribution of the exchange-correlation term. As discussed in previous sections, the presence of exchange-correlation functionals at LDA/GGA level does not lead to essential difficulties in phonon calculations. Furthermore, the nonlocal pseudopotential in the Kleinman-Bylander form [28] is added to this reduced model to test the availability for the split ACP to handle the case in presence of nonlocal potential.

The Hamiltonian in our 1D reduced Hartree-Fock model is given by

$$H[\rho] = -\frac{1}{2}\frac{d^2}{dx^2} + \left[\int K(x,y)\left(\rho(y)+m(y)\right)\,\mathrm{d}y\right]\delta(x,x') + \gamma\sum_I b(x-R_I)b^*(x'-R_I). \quad (3.43)$$

Here $m(x) = \sum_I m_I(x-R_I)$ is the summation of pseudocharges. Each function $m_I(x)$ takes the form of a one-dimensional Gaussian

$$m_I(x) = -\frac{Z_I}{\sqrt{2\pi\sigma_I^2}}\exp\left(-\frac{x^2}{2\sigma_I^2}\right), \quad (3.44)$$

where Z_I is an integer representing the charge of the I-th nucleus. In our numerical simulation, we choose all σ_I to be the same.

Instead of using a bare Coulomb interaction which diverges in 1D when x is large, we use a Yukawa kernel as the regularized Coulomb kernel

$$K(x,y) = \frac{2\pi e^{-\kappa|x-y|}}{\kappa\epsilon_0}, \quad (3.45)$$

which satisfies the equation

$$-\frac{d^2}{dx^2}K(x,y) + \kappa^2 K(x,y) = \frac{4\pi}{\epsilon_0}\delta(x-y). \quad (3.46)$$

As $\kappa \to 0$, the Yukawa kernel approaches the bare Coulomb interaction given by the Poisson equation. The parameter ϵ_0 is used so that the magnitude of the electron static contribution is comparable to that of the kinetic energy. The ion-ion repulsion energy E_{II} is also computed using the Yukawa interaction K in the model systems.

The last term in $H[\rho]$ represents the kernel of the nonlocal pseudopotential, which is the summation of rank-1 real symmetric operator with real valued function

$$b(x) = \frac{1}{\sqrt{2\pi\sigma_b^2}} \exp\left(-\frac{x^2}{2\sigma_b^2}\right). \tag{3.47}$$

γ is a scaling factor used to control the magnitude of the nonlocal pseudopotential, which is, in practice, much smaller than the local pseudopotential.

The parameters used in this model are chosen as follows. Atomic units are used throughout the discussion unless otherwise mentioned. For all systems tested in this subsection, the distance between each atom and its nearest neighbor is set to 2.4 a.u. The Yukawa parameter $\kappa = 0.1$. The nuclear charge Z_I is set to 1 for all atoms, and σ_I is set to 0.3. The parameter ϵ_0 is chosen to be 80 so that the reduced Hartree-Fock model can be tuned to resemble a metallic system. In the nonlocal pseudopotential, the scaling factor $\gamma = -0.01$, as well as σ_b set to be 0.1 (this will cause the total energy to change by 1.47%). The temperature T is set to be 5000 K to emphasize the influence of partial occupation. The Hamiltonian operator is represented in a plane wave basis set.

For the system of size $N_A = 80$, the 110 smallest eigenvalues as well as the occupational status near the chemical potential are shown in Fig. 3.2. There is no evident energy gap within the spectrum of the Hamiltonian. Orbitals can be partially occupied due to the finite temperature. Specifically, we identify an orbital to be (fully) occupied if the occupation number $f_i > 1 - 10^{-6}$, unoccupied if $f_i < 10^{-6}$, otherwise partially occupied. In this case, there are 20 partially occupied orbitals, whose eigenvalues are around the chemical potential. The total number of (fully) occupied and partially occupied orbitals N_{occ} is 89, and we choose $N_{\mathrm{cut}} = N_{\mathrm{occ}}$ for all the split ACP computations. Also we fix the number of pole expansion nodes N_p to be 40 unless otherwise mentioned.

In the ground state calculation, we use Anderson mixing [2] for accelerating the self-consistent field (SCF) iterations, and the linearized eigenvalue problems are solved by using the locally optimal block preconditioned conjugate gradient (LOBPCG) solver [29]. In DFPT, we use MINRES [47] to solve the Sternheimer equations iteratively. The initial guess vectors for the solutions are obtained from previous iterations in the Dyson equation to reduce the number of matrix-vector multiplications. The same strategy for choosing the initial guess is implemented for the split ACP formulation as well. Anderson mixing is used to accelerate the convergence of Dyson equations in DFPT, and in split ACP we use the fixed point iteration with Sherman-Morrison-Woodbury formula.

All numerical results of the split ACP method and FD approach below are benchmarked with results obtained from DFPT. We test the accuracy of the split ACP method in three different level: the diagonal elements $\mathrm{diag}(\mathfrak{X}_0\mathfrak{g})$, the diagonal elements of solution to Dyson equations $\mathrm{diag}(\mathfrak{X}\mathfrak{g})$, and the phonon frequencies $\{\omega_k\}$. For the diagonal

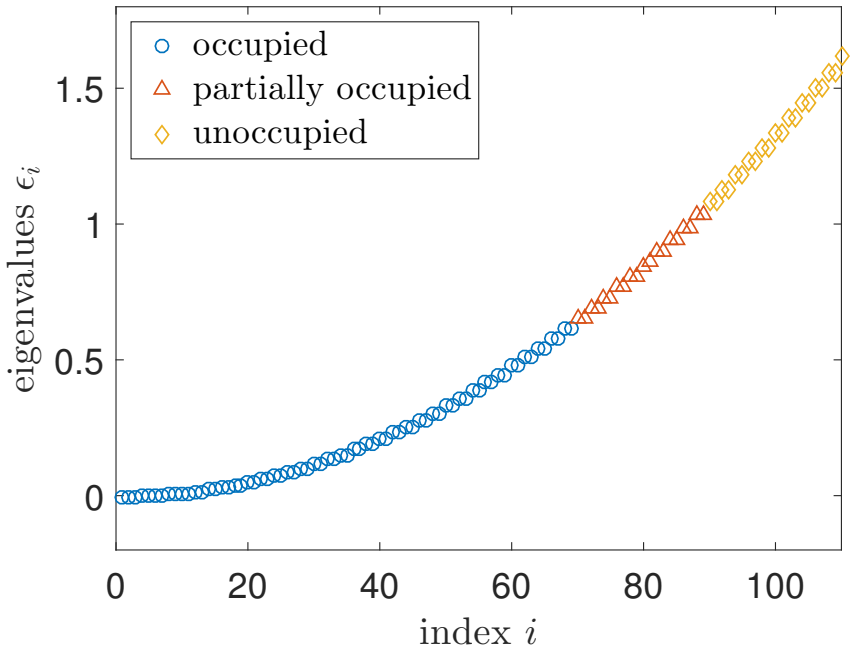

(a) eigenvalues

Figure 3.2: Eigenvalues of the 1D system with $N_A = 80$.

elements $\mathrm{diag}(\mathfrak{X}_0\mathfrak{g})$ and $\mathrm{diag}(\mathfrak{X}\mathfrak{g})$, we directly measure the relative L^2 error, defined as $\|\mathrm{diag}(\mathfrak{X}_0\mathfrak{g}) - \mathrm{diag}(\widetilde{\mathfrak{X}}_0\mathfrak{g})\|_2/\|\mathrm{diag}(\mathfrak{X}_0\mathfrak{g})\|_2$. For the phonon frequencies, due to the presence of acoustic phonon modes for which ω_k is close to 0, instead of the relative error, we measure the absolute L^∞ error defined as $\max_k |\omega_k - \widetilde{\omega}_k|$, where $\widetilde{\omega}_k$ is obtained from FD or split ACP. We also demonstrate the efficiency of the split ACP method by comparing the computational time and scaling of split ACP with that of DFPT and FD.

In Table 3.2 and 3.3, we calibrate the accuracy of the split compression with different choices of the numbers of Chebyshev nodes N_c and the numbers of columns N_μ, for two different choices of $\widetilde{N}_{\mathrm{cut}}$, respectively. We measure the accuracy by relative L^2 error $\|\mathrm{diag}(\mathfrak{X}_0\mathfrak{g}) - \mathrm{diag}(\widetilde{\mathfrak{X}}_0\mathfrak{g})\|_2/\|\mathrm{diag}(\mathfrak{X}_0\mathfrak{g})\|_2$, and choose $N_\mu = lN_{\mathrm{occ}}$ where $l = 3, 4, \cdots, 8$. Table 3.2 and 3.3 both show that, with a fixed number of Chebyshev nodes N_c, the error decreases monotonically with respect to N_μ, until limited by the accuracy of the Chebyshev interpolation procedure. Similarly, with a fixed number of selected columns, the numerical accuracy improves as more Chebyshev nodes are used in interpolation until limited by the choice of N_μ. Comparing Table 3.3 with Table 3.2, we also find that numerical accuracy can be better with a larger $\widetilde{N}_{\mathrm{cut}}$. This is due to the increase of the effective energy gap $\widetilde{\varepsilon}_g$, which leads to a smaller numerical error in the Chebyshev interpolation procedure. For $\widetilde{N}_{\mathrm{cut}}/N_{\mathrm{cut}} \approx 1.28$, the relative L^2 error of $\chi_0 G$ can be less than 10^{-6} for large enough N_c and

N_c \ N_μ	$3N_{\text{occ}}$	$4N_{\text{occ}}$	$5N_{\text{occ}}$	$6N_{\text{occ}}$	$7N_{\text{occ}}$	$8N_{\text{occ}}$
3	2.38E-02	2.17E-02	2.13E-02	2.12E-02	2.12E-02	2.12E-02
4	2.06E-02	9.43E-03	6.25E-03	6.21E-03	6.21E-03	6.21E-03
5	2.01E-02	7.88E-03	2.86E-03	2.85E-03	2.84E-03	2.84E-03
6	1.64E-02	6.76E-03	1.73E-03	1.65E-03	1.65E-03	1.65E-03
7	1.65E-02	9.30E-03	8.10E-04	6.85E-04	6.87E-04	6.87E-04
8	1.62E-02	9.07E-03	5.86E-04	2.53E-04	2.50E-04	2.50E-04
9	1.81E-02	7.24E-03	7.86E-04	1.51E-04	1.47E-04	1.47E-04
10	1.49E-02	6.53E-03	5.83E-04	7.99E-05	7.24E-05	7.24E-05

Table 3.2: The relative L^2 error $\|\text{diag}(\mathfrak{X}_0\mathfrak{g}) - \text{diag}(\widetilde{\mathfrak{X}}_0\mathfrak{g})\|_2/\|\text{diag}(\mathfrak{X}_0\mathfrak{g})\|_2$ for $\widetilde{N}_{\text{cut}}/N_{\text{cut}} \approx 1.06$ with the effective gap $\widetilde{\varepsilon}_g/|\mathcal{I}| \approx 0.1408$.

N_c \ N_μ	$3N_{\text{occ}}$	$4N_{\text{occ}}$	$5N_{\text{occ}}$	$6N_{\text{occ}}$	$7N_{\text{occ}}$	$8N_{\text{occ}}$
3	1.56E-02	8.52E-03	9.45E-04	7.42E-04	7.39E-04	7.39E-04
4	1.72E-02	7.79E-03	6.82E-04	1.02E-04	9.67E-05	9.67E-05
5	1.74E-02	9.49E-03	8.90E-04	6.00E-05	2.50E-05	2.50E-05
6	1.56E-02	7.80E-03	5.89E-04	7.06E-05	5.40E-06	5.38E-06
7	1.62E-02	9.07E-03	6.11E-04	5.51E-05	8.45E-07	8.42E-07
8	1.61E-02	9.04E-03	5.97E-04	4.73E-05	5.55E-07	3.21E-07
9	1.85E-02	9.08E-03	6.45E-04	4.52E-05	4.88E-07	3.20E-07
10	1.55E-02	9.52E-03	8.12E-04	5.72E-05	4.97E-07	3.20E-07

Table 3.3: The relative L^2 error $\|\text{diag}(\mathfrak{X}_0\mathfrak{g}) - \text{diag}(\widetilde{\mathfrak{X}}_0\mathfrak{g})\|_2/\|\text{diag}(\mathfrak{X}_0\mathfrak{g})\|_2$ for $\widetilde{N}_{\text{cut}}/N_{\text{cut}} \approx 1.28$ with the effective gap $\widetilde{\varepsilon}_g/|\mathcal{I}| \approx 0.6777$.

N_μ.

We further study how different choices of N_c and $\widetilde{N}_{\text{cut}}$ affect the computational accuracy on $\text{diag}(\mathfrak{X}_0\mathfrak{g})$. Here for all N_c and $\widetilde{N}_{\text{cut}}$, N_μ is fixed to be $480 \approx 5.4N_{\text{occ}}$ or $560 \approx 6.3N_{\text{occ}}$. This is determined the same way as that in the regular ACP formulation so that $|\widetilde{R}_{N_\mu+1,N_\mu+1}| < \epsilon|\widetilde{R}_{1,1}| \leq |\widetilde{R}_{N_\mu,N_\mu}|$ in Algorithm 2 in [35], with $\epsilon = 10^{-4}$ and 10^{-5}, respectively. Fig. 3.3 compares the relative L^2 errors $\|\text{diag}(\mathfrak{X}_0\mathfrak{g}) - \text{diag}(\widetilde{\mathfrak{X}}_0\mathfrak{g})\|_2/\|\text{diag}(\mathfrak{X}_0\mathfrak{g})\|_2$ under different $\widetilde{N}_{\text{cut}}$ and N_c. We find that it can be sufficient to choose $\widetilde{N}_{\text{cut}} \leq 2N_{\text{cut}}$ to achieve the best accuracy possible where further improvement is hindered by the the choice of N_μ (around 3×10^{-5} for $N_\mu \approx 5.4N_{\text{occ}}$ and 1×10^{-6} for $N_\mu \approx 6.3N_{\text{occ}}$). Under the split ACP formulation, the number of Chebyshev nodes is significantly reduced. Specifically, 4-8 nodes can already perform fairly accurate calculation while no less than 20 nodes are needed in the regular

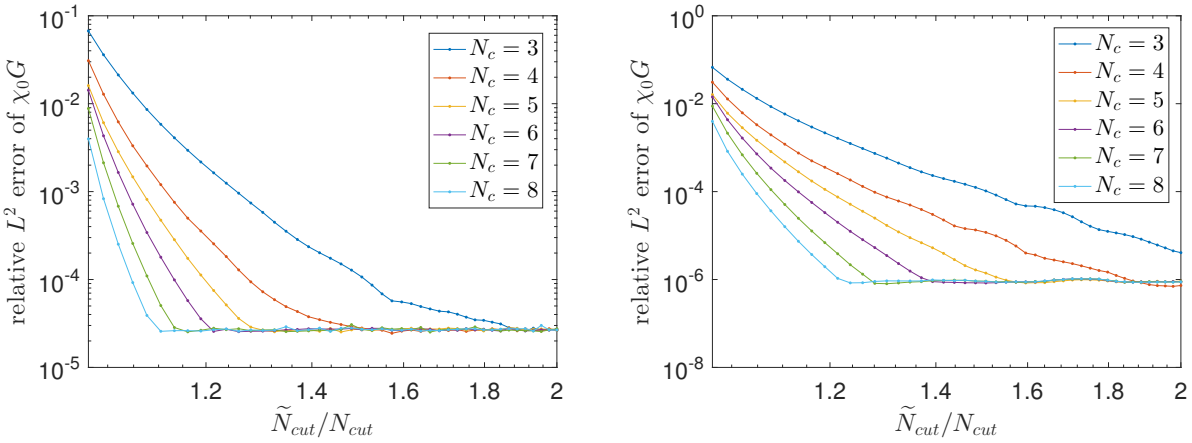

(a) $N_\mu \approx 5.4 N_{\text{occ}}$ (b) $N_\mu \approx 6.3 N_{\text{occ}}$

Figure 3.3: The relative L^2 errors $\|\text{diag}(\mathfrak{X}_0\mathfrak{g}) - \text{diag}(\widetilde{\mathfrak{X}}_0\mathfrak{g})\|_2/\|\text{diag}(\mathfrak{X}_0\mathfrak{g})\|_2$ under different $\widetilde{N}_{\text{cut}}$ and N_c

ACP formulation. Furthermore, the more Chebyshev nodes are used, the smaller $\widetilde{N}_{\text{cut}}$ we can choose to achieve the same accuracy. For example, if 5 nodes are adopted in Chebyshev interpolation, we need to choose $\widetilde{N}_{\text{cut}}$ as large as $1.55N_{\text{cut}}$ to achieve the best accuracy, while $\widetilde{N}_{\text{cut}} \approx 1.2N_{\text{cut}}$ is sufficient if N_c increases to 8.

In order to demonstrate the effectiveness of the split representation, the relative L^2 error $\|\text{diag}(\mathfrak{X}\mathfrak{g}) - \text{diag}(\widetilde{\mathfrak{X}}\mathfrak{g})\|_2/\|\text{diag}(\mathfrak{X}\mathfrak{g})\|_2$ during the fixed point iteration when solving Dyson equation is shown in Fig. 3.4. For each choice of N_μ, numerical results show significant improvement after only one iteration, and the self-consistent iteration converges within two steps. After convergence, the error is around 1.4×10^{-3} for $\epsilon = 10^{-3}$, 6.2×10^{-5} for $\epsilon = 10^{-4}$, and 6.4×10^{-6} for $\epsilon = 10^{-5}$.

Method and parameters	L^∞-norm error
FD, $\delta = 0.01$	7.79E-05
split ACP, $N_p = 20$, $N_\mu \approx 5.4N_{\text{occ}}$ for $\epsilon = 10^{-4}$	5.90E-05
split ACP, $N_p = 40$, $N_\mu \approx 6.3N_{\text{occ}}$ for $\epsilon = 10^{-5}$	1.51E-05

Table 3.4: L^∞ error of the phonon frequencies. System size is $N_A = 80$. Chebyshev nodes $N_c = 5$ in split ACP.

Next we compare the split ACP with DFPT and FD in terms of the accuracy of phonon frequencies. Table 3.4 presents L^∞ error of the phonon spectrum obtained by FD and split ACP with different parameters benchmarked with that from DFPT. In the FD approach, the convergence tolerance for LOBPCG is set to be 10^{-8}, and the SCF convergence tolerance is 10^{-10}. δ denotes the perturbation of each atom position to the origin. We remark that

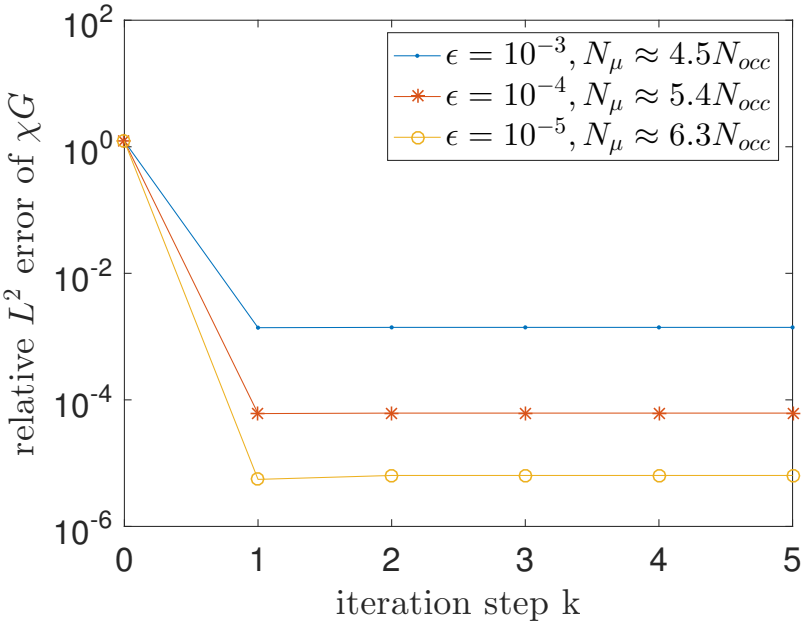

Figure 3.4: Convergence for solving the Dyson equation using the split ACP formulation.

further smaller δ can lead to slightly larger numerical error due to the numerical instability of FD approach, and the numerical error of FD approach is usually around 10^{-4}. As for the split ACP, the same parameters for LOBPCG and SCF are chosen to converge the ground state calculation, and 5 nodes are used in the Chebyshev interpolation procedure. We find that it is sufficient to choose $N_p = 20$ and $N_\mu \approx 5.4 N_{\text{occ}}$ to achieve comparable accuracy with FD approach. Furthermore, with more nodes in pole expansion and more selected columns, the L^∞ error of split ACP can be as small as around 10^{-5}, in which case split ACP can be more accurate than FD approach.

Method	Computational scaling
DFPT	4.0036
FD	3.8057
split ACP	3.1587
split ACP 1 iteration	3.1433

Table 3.5: Computational scaling measured from $N_A = 90$ to $N_A = 140$.

In the end we perform phonon calculations for systems of size from 30 to 140. We choose $\delta = 0.01$ for FD approach. Fig. 3.5a shows that the accuracy of phonon spectrum (L^∞ error) from FD approach remains roughly the same as the system size increases, which is

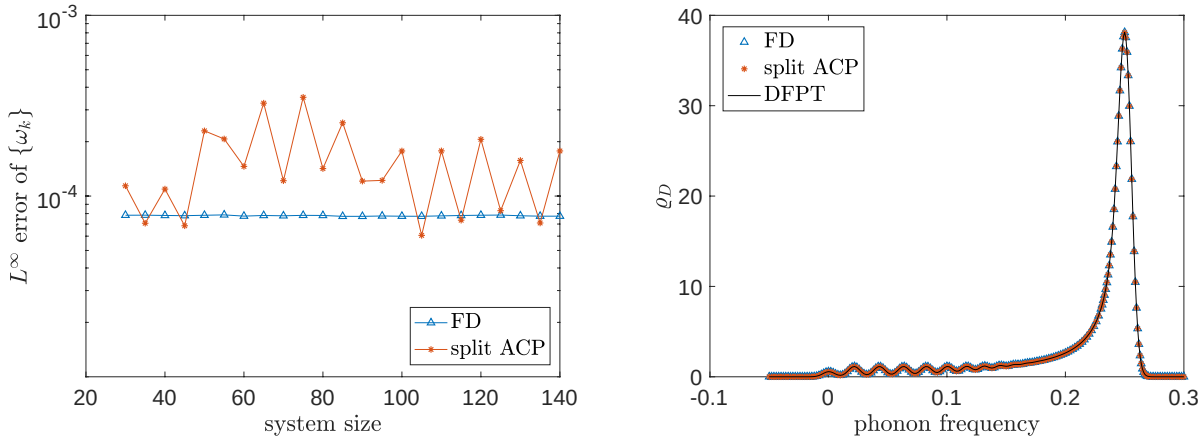

Figure 3.5: (a) L^∞ error of the phonon frequencies $\{\omega_k\}$. (b) Phonon spectrum for the 1D system.

empirically around 10^{-4}. For the split ACP, we find that $\epsilon = 10^{-4}$, $N_c = 4$, $N_p = 20$ and $\widetilde{N}_{\text{cut}} \approx 1.7 N_{\text{cut}}$ is sufficient to achieve error around 10^{-4}. Since the convergence of the split adaptive compression can be very fast, as discussed before, we also carry out the phonon calculation by split ACP with only 1 step of iteration on solving Dyson equation, and the numerical accuracy is almost the same as that of split ACP. Fig. 3.5b reports the phonon spectrum ϱ_D for system of size $N_A = 140$. We remark that Fig 3.5b plots ϱ_D by smearing the Dirac-δ distribution in (1.65) using a regularized function

$$\delta_\sigma(x) = \frac{1}{\sqrt{2\pi\sigma^2}} e^{-\frac{x^2}{2\sigma^2}},$$

where the smear parameter σ is chosen to be 0.005.

To demonstrate the efficiency of the split ACP formulation, Fig. 3.6 compares the computational time of different methods. We observe that the split ACP can be more advantageous than DFPT for systems merely beyond 40 atoms, and become more advantageous than FD for systems beyond 60 atoms. Due to the less iterations on solving Dyson equation, the split ACP with 1 iteration can be faster than the split ACP. For the largest system with 140 atoms, split ACP with 1 iteration is 3.83 and 1.91 times faster than DFPT and FD, respectively.

Table 3.5 measures the slope of the computational cost with respect to system sizes from $N_A = 90$ to $N_A = 140$. In theory, the asymptotic computational cost of DFPT and FD should be $\mathcal{O}(N_e^4)$, and the cost of split ACP should be $\mathcal{O}(N_e^3)$. For all the methods, numerical scalings shown in Table 3.5 match closely with the theoretical ones.

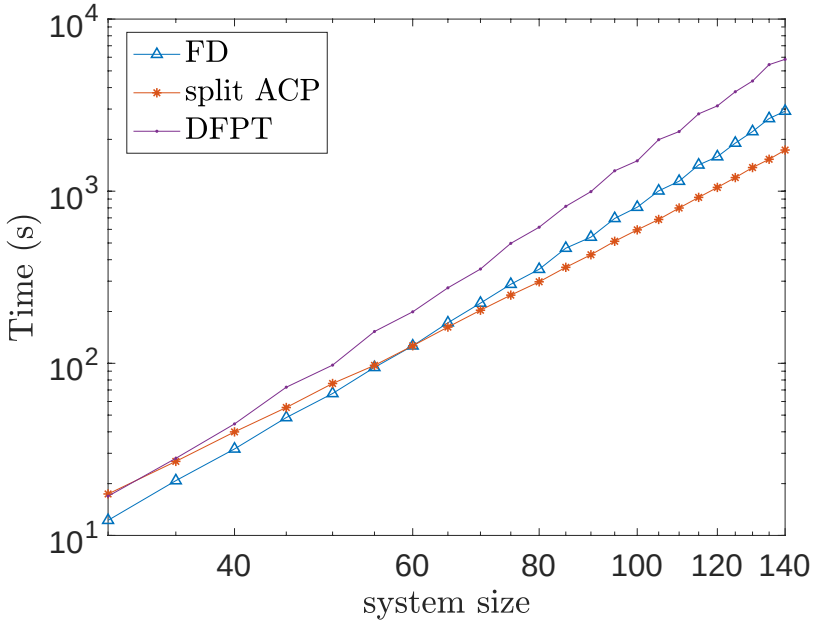

Figure 3.6: Computational time of 1D examples.

3.4.2 3D aluminum cluster

In this section, we present the result of phonon calculations of a 3D aluminum cluster. Each unit cell is a $7.65 \times 7.65 \times 7.65$ a.u. with 4 Al atoms. The computational supercell consists of $2 \times 2 \times 1$ unit cells and has 16 atoms and 48 electrons. We use the spin-restricted formulation and the Perdew-Zunger pseudopotential [50], and the temperature is set to 1000K. E_{cut} is set to 10 Hartree. We set $N_{\text{cut}} = 33$, $\widetilde{N}_{\text{cut}} = 47$, and the number of Chebyshev interpolation N_c to be 6. For the system size tested, we found that using Eq.(3.16) directly for computing the singular part of the polarizability matrix much more faster than using the pole expansion. So the computation is done using Eq.(3.16) for the purpose of testing the accuracy of the algorithm. This results in much shorter computational time given the size of the system tested is small.

Figure 3.7 reports the relative error in the iteration of solving the Dyson equation. We remark that for this system, $N_\mu = 1584$. In comparison, the total grid points in the discretization is $N_g = 42592$. This means that the numerical rank of the operator χ far less than the number of grid points. The iteration is converged to 10^{-6} relative error for 6 steps.

Figure 3.8 reports the phonon spectrum computed from both FD and split ACP. The smearing parameter for plotting the spectrum is chosen as 0.008. The L^∞ error on the density of states is 5.62E-05.

We remark that the purpose of the test above is to illustrate that the split ACP formulation can indeed be used to accurately obtain the phonon spectrum for 3D metallic systems, with fractionally occupied states and nonlocal pseudopotentials. However, due to the small

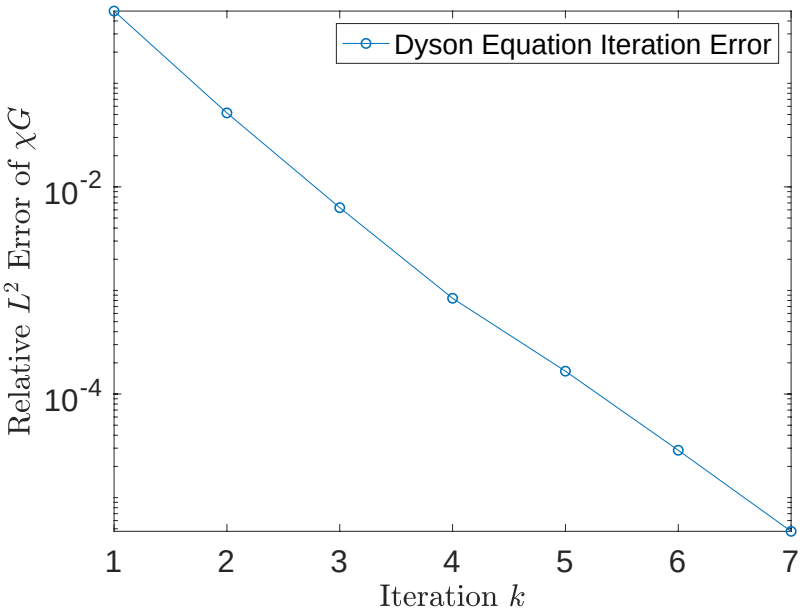

Figure 3.7: The Dyson Equations iteration error.

system size, the computational time of the split representation of ACP is in fact much longer than that of FD. Also we remark that there is difficulty in the DFPT approach in 3D. The Sternheimer equations are ill-conditioned and the MINRES iteration fail to converge. This result also emphasizes the necessity of introducing the effective gap in the split ACP.

Since KSSOLV is only designed to solve Kohn-Sham equations for systems with relatively small sizes, our implementation cannot reveal the efficiency of the split ACP approach yet for 3D systems, and this will be our future work.

3.5 Conclusion

In this chapter, we have introduced the split representation of a recently developed method called the adaptively compressed polarizability operator. The split-ACP formulation incorporate nonlocal pseudopotentials and finite temperature effects successfully, hence generalizes the ACP formulation to solve for phonons in metallic systems as well. Our numerical results for model problems indicate that the computational advantage of the split ACP fomulation can be clealy observed compared to DFPT and finited difference, even for systems of relatively small sizes. The numerical example for 3D Aluminum cluster shows that accuracy of the split ACP formulation in the application for computing the phonon spectrum for real materials.

The new split representation of ACP provides a systematic and complete solution to treating systems at finite temperature. We have used phonon calculation as an example

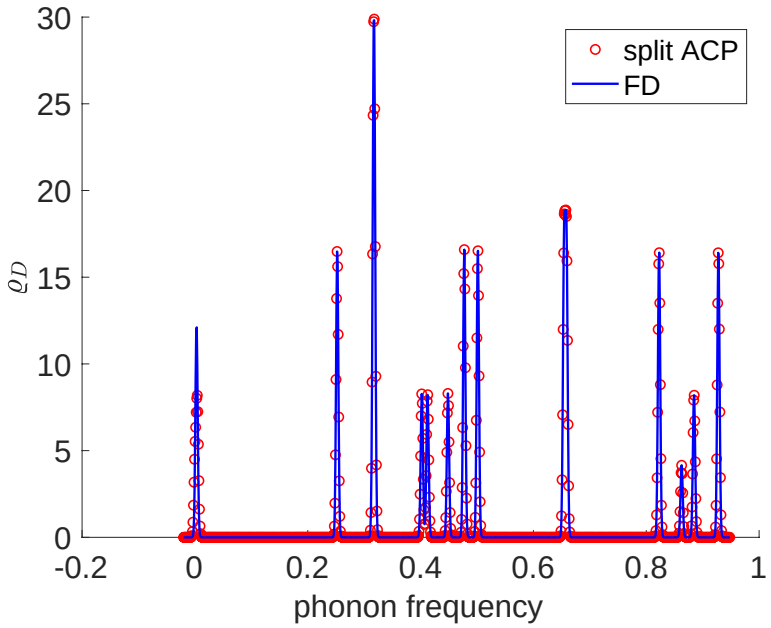

Figure 3.8: Phonon spectrum of 3D Aluminum Cluster.

to demonstrate the effectiveness as well as accuracy of the split representation of adaptively compressed polarizability operator. The same strategy can be applied to applications of DFPT other than phonon calculations, when the polarizability operator χ need to be applied to a large number of vectors. Moreover, Meanwhile, all numerical tests are on single-threaded. Parallelized implementation would help fully test whether split representation of ACP formulation can achieve the goal of reducing complexity to asymptotically $\mathcal{O}(N_e^3)$.

Through the discussion in chapter 3, we have generalized the ACP method taking into account the nonlocal pseudopotential and treating finite temperature. We obtain an accurate, efficient method to compute the vibrational properties for insulating and metallic systems. The ACP method along with the split representation is by far the first method to achieve the asymptotical complexity of $\mathcal{O}(N_e^3)$ in phonon calculations.

Bibliography

[1] S. L. Adler. "Quantum Theory of the Dielectric Constant in Real Solids". In: *Phys. Rev.* 126 (1962), pp. 413–420.

[2] D. G. Anderson. "Iterative procedures for nonlinear integral equations". In: *J. Assoc. Comput. Mach.* 12 (1965), pp. 547–560.

[3] S. Baroni, P. Giannozzi, and A. Testa. "Green's-function approach to linear response in solids". In: *Phys. Rev. Lett.* 58 (1987), pp. 1861–1864.

[4] S. Baroni and R. Resta. "Ab initio calculation of the low-frequency Raman cross section in silicon". In: *Phys. Rev. B* 33 (1986), p. 5969.

[5] S. Baroni et al. "Phonons and related crystal properties from density-functional perturbation theory". In: *Rev. Mod. Phys.* 73 (2001), pp. 515–562.

[6] A. D. Becke. "Density-functional exchange-energy approximation with correct asymptotic behavior". In: *Phys. Rev. A* 38 (1988), pp. 3098–3100.

[7] M. Born and R. Oppenheimer. "Zur quantentheorie der molekeln". In: *Ann. Phys. (Leipzig)* 389 (1927), pp. 457–484.

[8] D. R. Bowler and T. Miyazaki. "O(N) methods in electronic structure calculations". In: *Rep. Prog. Phys.* 75 (2012), p. 036503.

[9] E. Cances, A. Deleurence, and M. Lewin. "A New Approach to the Modeling of Local Defects in Crystals: The Reduced Hartree-Fock Case". In: *Commun. Math. Phys.* 281 (2008), pp. 129–177.

[10] E. Cances, A. Deleurence, and M. Lewin. "Non-perturbative embedding of local defects in crystalline materials". In: *J. Phys.: Condens. Matter* 20 (2008), pp. 294213–294218.

[11] E. Cances and N. Mourad. "A mathematical perspective on density functional perturbation theory". In: *Nonlinearity* 27 (2014), p. 1999.

[12] D. M. Ceperley and B. J. Alder. "Ground state of the electron gas by a stochastic method". In: *Phys. Rev. Lett.* 45 (1980), pp. 566–569.

[13] T. F. Chan and Per C. Hansen. "Computing truncated singular value decomposition least squares solutions by rank revealing QR-factorizations". In: *SIAM J. Sci. Stat. Comput.* 11 (1990), pp. 519–530.

[14] H. Cheng et al. "On the compression of low rank matrices". In: *SIAM J. Sci. Comput.* 26 (2005), pp. 1389–1404.

[15] A. Damle, L. Lin, and L. Ying. "Compressed Representation of Kohn–Sham Orbitals via Selected Columns of the Density Matrix". In: *J. Chem. Theory Comput.* 11.4 (2015), pp. 1463–1469.

[16] H-R. Fang and Y. Saad. "Two classes of multisecant methods for nonlinear acceleration". In: *Numer. Linear Algebra Appl.* 16 (2009), pp. 197–221.

[17] D. Foerster. "Elimination, in electronic structure calculations, of redundant orbital products". In: *J. Chem. Phys.* 128 (2008), p. 034108.

[18] F. Giustino, M. L. Cohen, and S. G. Louie. "GW method with the self-consistent Sternheimer equation". In: *Phys. Rev. B* 81 (2010), p. 115105.

[19] S. Goedecker. "Linear scaling electronic structure methods". In: *Rev. Mod. Phys.* 71 (1999), pp. 1085–1123.

[20] X. Gonze. "Adiabatic density-functional perturbation theory". In: *Phys. Rev. A* 52 (1995), pp. 1096–1114.

[21] X. Gonze and C. Lee. "Dynamical matrices, Born effective charges, dielectric permittivity tensors, and interatomic force constants from density-functional perturbation theory". In: *Phys. Rev. B* 55 (1997), p. 10355.

[22] X. Gonze and J.-P. Vigneron. "Density-functional approach to nonlinear-response coefficients of solids". In: *Phys. Rev. B* 39 (1989), p. 13120.

[23] M. Gu and S. Eisenstat. "Efficient Algorithms for Computing a Strong Rank-Revealing QR Factorization". In: *SIAM J. Sci. Comput.* 17.4 (1996), pp. 848–869.

[24] N. Halko, P.-G. Martinsson, and J. A. Tropp. "Finding structure with randomness: Probabilistic algorithms for constructing approximate matrix decompositions". In: *SIAM Rev.* 53.2 (2011), pp. 217–288.

[25] L. Hedin. "New method for calculating the one-particle Green's function with application to the electron-gas problem". In: *Phys. Rev.* 139 (1965), A796.

[26] P. Hohenberg and W. Kohn. "Inhomogeneous electron gas". In: *Phys. Rev.* 136 (1964), B864–B871.

[27] D. D. Johnson. "Modified Broyden's method for accelerating convergence in self-consistent calculations". In: *Phys. Rev. B* 38 (1988), pp. 12807–12813.

[28] L. Kleinman and D. M. Bylander. "Efficacious form for model pseudopotentials". In: *Phys. Rev. Lett.* 48 (1982), pp. 1425–1428.

[29] A. V. Knyazev. "Toward the Optimal Preconditioned Eigensolver: Locally Optimal Block Preconditioned Conjugate Gradient Method". In: *SIAM J. Sci. Comp.* 23 (2001), pp. 517–541.

[30] W. Kohn. "Density Functional and Density Matrix Method Scaling Linearly with the Number of Atoms". In: *Phys. Rev. Lett.* 76 (1996), pp. 3168–3171.

[31] W. Kohn and L. Sham. "Self-consistent equations including exchange and correlation effects". In: *Phys. Rev.* 140 (1965), A1133–A1138.

[32] C. Lee, W. Yang, and R. G. Parr. "Development of the Colle-Salvetti correlation-energy formula into a functional of the electron density". In: *Phys. Rev. B* 37 (1988), pp. 785–789.

[33] L. Lin. "Adaptively Compressed Exchange Operator". In: *J. Chem. Theory Comput., in press* (2016).

[34] L. Lin, Y. Saad, and C. Yang. "Approximating spectral densities of large matrices". In: *SIAM Rev.* 58 (2016), p. 34.

[35] L. Lin, Z. Xu, and L. Ying. "Adaptively compressed polarizability operator for accelerating large scale *ab initio* phonon calculations". In: *SIAM Multiscale Model. Simul.* 15 (2017), pp. 29–55.

[36] L. Lin et al. "Pole-based approximation of the Fermi-Dirac function". In: *Chin. Ann. Math.* 30B (2009), p. 729.

[37] J. Lu, C. D. Sogge, and S. Steinerberger. *Approximating pointwise products of Laplacian eigenfunctions*. preprint, arXiv:1811.10447. 2018.

[38] J. Lu and L. Ying. "Compression of the electron repulsion integral tensor in tensor hypercontraction format with cubic scaling cost". In: *J. Comput. Phys.* 302 (2015), p. 329.

[39] L. D. Marks and D. R. Luke. "Robust mixing for *ab initio* quantum mechanical calculations". In: *Phys. Rev. B* 78 (2008), pp. 075114–075125.

[40] R. Martin. *Electronic Structure – Basic Theory and Practical Methods*. West Nyack, NY: Cambridge Univ. Pr., 2004.

[41] N.D. Mermin. "Thermal properties of the inhomogeneous electron gas". In: *Phys. Rev.* 137 (1965), A1441.

[42] Jonathan E Moussa. "Minimax rational approximation of the Fermi-Dirac distribution". In: *The Journal of chemical physics* 145.16 (2016), p. 164108.

[43] Yuji Nakatsukasa, Olivier Sete, and Lloyd N Trefethen. "The AAA algorithm for rational approximation". In: *SIAM Journal on Scientific Computing* 40.3 (2018), A1494–A1522.

[44] H.-V. Nguyen et al. "Improving accuracy and efficiency of calculations of photoemission spectra within the many-body perturbation theory". In: *Phys. Rev. B* 85 (2012), p. 081101.

[45] A. M. N. Niklasson and M. Challacombe. "Density matrix perturbation theory". In: *Phys. Rev. Lett.* 92 (2004), p. 193001.

[46] G. Onida, L. Reining, and A. Rubio. "Electronic excitations: density-functional versus many-body Green's-function approaches". In: *Rev. Mod. Phys.* 74 (2002), p. 601.

[47] C. C. Paige and M. A Saunders. "Solution of sparse indefinite systems of linear equations". In: *SIAM J. Numer. Anal.* 12 (1975), pp. 617–629.

[48] J. E. Pask and P. A. Sterne. "Real-space formulation of the electrostatic potential and total energy of solids". In: *Phys. Rev. B* 71 (2005), pp. 113101–113104.

[49] J. P. Perdew, K. Burke, and M. Ernzerhof. "Generalized gradient approximation made simple". In: *Phys. Rev. Lett.* 77 (1996), pp. 3865–3868.

[50] J. P. Perdew and A. Zunger. "Self-interaction correction to density-functional approximations for many-electron systems". In: *Phys. Rev. B* 23 (1981), pp. 5048–5079.

[51] X. Ren et al. "Resolution-of-identity approach to Hartree–Fock, hybrid density functionals, RPA, MP2 and GW with numeric atom-centered orbital basis functions". In: *New J. Phys.* 14 (2012), p. 053020.

[52] A. Sodt, J. E. Subotnik, and M. Head-Gordon. "Linear scaling density fitting". In: *J. Chem. Phys.* 125 (2006), p. 194109.

[53] J. P. Solovej. "Proof of the ionization conjecture in a reduced Hartree-Fock model". In: *Invent. Math.* 104 (1991), pp. 291–311.

[54] Abdulnour Y Toukmaji and John A Board Jr. "Ewald summation techniques in perspective: a survey". In: *Computer physics communications* 95.2-3 (1996), pp. 73–92.

[55] Lloyd N Trefethen. "Is Gauss quadrature better than Clenshaw-Curtis?" In: *SIAM review* 50.1 (2008), pp. 67–87.

[56] P. Umari, G. Stenuit, and S. Baroni. "GW quasiparticle spectra from occupied states only". In: *Phys. Rev. B* 81 (2010), p. 115104.

[57] P. Umari, G. Stenuit, and S. Baroni. "Optimal representation of the polarization propagator for large-scale GW calculations". In: *Phys. Rev. B* 79.20 (2009), p. 201104.

[58] F. Weigend. "A fully direct RI-HF algorithm: Implementation, optimised auxiliary basis sets, demonstration of accuracy and efficiency". In: *Phys. Chem. Chem. Phys.* 4 (2002), pp. 4285–4291.

[59] E Weinan and Jianfeng Lu. *The Kohn-Sham equation for deformed crystals*. Vol. 221. American Mathematical Soc., 2013.

[60] N. Wiser. "Dielectric Constant with Local Field Effects Included". In: *Phys. Rev.* 129 (1963), pp. 62–69.

[61] F. Woolfe et al. "A fast randomized algorithm for the approximation of matrices". In: *Appl. Comput. Harmon. Anal.* 25.3 (2008), pp. 335–366.

[62] C. Yang et al. "KSSOLV–a MATLAB toolbox for solving the Kohn–Sham equations". In: *ACM Trans. Math. Software* 36 (2009), p. 10.

[63] M. T. Yin and M. L. Cohen. "Theory of static structural properties, crystal stability, and phase transformations: Application to Si and Ge". In: *Phys. Rev. B* 26 (1982), p. 5668.